Additive Nanomanufacturing of Flexible Hybrid Electronics

by

Zabihollah Ahmadi

A dissertation submitted to the Graduate Faculty of
Auburn University
in partial fulfillment of the
requirements for the Degree of
Doctor of Philosophy

Auburn, Alabama
May 6, 2023

Keywords: Additive Nanomanufacturing, Flexible hybrid electronics, Printed electronics, Multi Material Printing

Approved by

Masoud Mahjouri-Samani, Chair, Assistant Professor, Department of Electrical and Computer Engineering
Robert Dean, Professor, Department of Electrical and Computer Engineering
Michael Hamilton, Professor, Department of Electrical and Computer Engineering
Mark Adams, Associate Professor, Department of Electrical and Computer Engineering
Tae-Sik Oh, Assistant Professor, Chemical Engineering

Abstract

There is always great interest in finding new advanced manufacturing techniques to pave the way for realization of future flexible and wearable electronics. Direct printing of functional materials, structures, and devices on various platforms such as flexible to rigid substrates are of interest for applications ranging from electronics to energy and sensing to biomedical devices. Current additive manufacturing (AM) at micro scale processes are either limited by the available sources of functional materials or require to be in the form of precisely designed inks. In addition, the existence of surfactants/additives in inks add further printing complexity and contamination issues to the process. Here, for the first time, we report a novel laser-based additive nanomanufacturing (ANM) system capable of in-situ and on-demand generations of nanoparticles that can serve as nanoscale building blocks for real-time sintering and printing a variety of multifunctional materials and patterns at atmospheric pressure and temperature. We show the ability to print different materials, including titanium dioxide (TiO_2), barium titanate (BTO), and indium tin oxide (ITO), on various rigid and flexible platforms such as silicon dioxide (SiO_2), paper, polydimethylsiloxane (PDMS), and polyethylene terephthalate (PET) substrates. This nonequilibrium process involves a pulsed laser for the ablation of targets and in-situ formation of pure amorphous nanoparticles in atmospheric pressure and temperature. These amorphous nanoparticles are then guided through a nozzle via an inert carrier gas onto the surface of the substrate, where they are sintered/crystallized in real-time. We further show the process-structure relationship of the printed materials from nano to microscale.

We demonstrated the dry printing and additive nanomanufacturing of flexible hybrid electronics and sensors on flexible polyimide and PET substrates. The electrical and mechanical characterization of the printed lines are studied, and different flexible hybrid electronics designs are printed and the performance of the devices are tested.

Silver is the 68^{th} most abundant element in the earth while copper is the 25^{th}, which makes copper cheaper (1% of the price of silver). Therefore, printing copper has attracted more attention because of its huge potential. Using this technique, we were able to get the 12 μΩ.cm resistivity. Resistance of printed Cu measured in 5 months showed negligible variation, confirming the good stability of printed Cu in long time. 5B classification of ASTM adhesion test confirmed the good adhesion between the sintered Cu and polyimide kapton substrate.

We upgraded the ANM printer to a multimaterial additive nanomanufacturing (M-ANM), allowing the printing of lateral and vertical hybrid structures and devices. By using M-ANM technique, various multimaterial devices such as silver/zinc oxide (Ag/ZnO) photodetector and hybrid silver/aluminum oxide (Ag/Al_2O_3) circuits has been printed and tested.

The formation of a trench can increase the mechanical interlocking and interfacial region of the printed material, which can improve its reliability. We demonstrated a facile technique for simultaneously creating trench into polyimide substrates via laser etching process, followed by printing and sintering the laser-ablated silver (Ag) nanoparticles onto the embedded trench in the polyimide substrate. The irradiated areas is evaluated by mean of optical microscopy, and the relationship between laser beam fluence, pulse repetition rate and number of scanning path to the depth of created trench is described.

Acknowledgments

I would like to give a special thanks to my advisor **Dr. Masoud Mahjouri-Samani** throughout my PhD study.

I would also like to thank my committee members, **Dr. Robert Dean**, **Dr. Michael C. Hamilton, Dr. Mark Adams and Dr. Tae-Sik Oh** for their review and commentary.

This endeavor would not have been possible without great support of National Center of Additive Manufacturing Excellence (NCAME) Facility at the Auburn University, for the SEM characterization of printed samples, **Dr. Raymond R. Unocic** for conducting the STEM characterization for generated nanoparticles at the Center for Nanophase Materials Sciences (CNMS), Oak Ridge National Laboratory, a U.S. Department of Energy (DOE). I appreciate the support from the Alabama Micro/Nanoelectronic Science and Technology Center (AMNSTC) for providing access to the cleanroom facility.

In addition, I am grateful for my lab-mates Aarsh Patel, Nurul Azam, and Suman Jaiswal for their support during my entire study at Auburn University.

My sincere gratitude goes to my beloved parents and sisters, Ezattolah Ahmadi, Moghadaseh Kameli, Mona and Maedeh Ahmadi. I will forever be grateful to them. Without the support and guidance of them, I would have never be where I am today. I also would like to specially thank my best friends, Asal Abasi, Mohammad Azizi, Majid Shamsi and Abbas Negahdari. These people played a significant role in my life and I will never forget.

Table of Contents

List of Tables

List of Figures

Figure 2.5. Examples of patterned 2D crystals on the PDMS substrates. A photonics Mach Zehnder interferometer (a), an electronics circuit board (b), Auburn University logo (c) and eagle image (d) fabricated by laser crystallization of amorphous WSe_2 layer on PDMS substrates. Scale bar is same for all pictures.

Figure 2.6. A photograph image of fabricated devices (a), schematic illustration of crystalline 2D materials used as photodetector (b), IV characteristics of a 5nm thick crystallized MoS_2 layer device (c), resistance of a fabricated device according to the bending radius under tensile strain (d).

Figure 3.1. Schematic illustration of the ANM process used for printing various functional materials on the different substrates (a). Enlarged illustration of in-situ and on-demand generating of nanoparticles by pulsed laser ablation of the desired target materials in atmospheric pressure and temperature (b). Enlarged illustration of real-time laser sintering and crystallization of nanoparticles on the surface of the substrate (c). Optical image of printed circuit lines using the ANM process (d). Enlarged optical image of the printed circuit lines (e).

Figure 3.2. SEM image of ablated pure amorphous TiO_2 nanoparticles (a). STEM (b) and HAADF (c) images with different magnifications of ablated pure amorphous TiO_2 nanoparticles.

Figure 3.3. Representative Raman spectra of TiO_2 nanoparticles sintered at different crystallization energies, 0.07 up to 0.56 J/cm^2.

Figure 3.4. SEM image of as-produced amorphous TiO_2 ablated by laser (a), sintered TiO_2 at 60 s (b), 180 s (c) and 270 s (d) while crystallization energy and other parameters are kept constant. Line created by ANM method (ablation energy = 2.3 J/cm^2, gas flow rate = 2.8 SLPM, sintering/crystallization energy = 0.3 J/cm^2, repetition rate = 10 Hz, 90% overlap, X-Y delay = 5

s) with 100 μm diameter (e), sintered TiO_2 at 0.295 J/cm^2 (f), 0.4 J/cm^2 (g), 0.67 J/cm^2 (h) crystallization energy while time (60 s) and other parameters are kept constant.

Figure 3.5. The thickness of ANM-printed dots as a function of gas flow rate for 0.3 J/cm^2 and 0.46 J/cm^2 in (a) and (c) sintering/crystallization energies. The thickness of ANM-printed dots as a function of repetition rate with 0.3 J/cm^2 and 0.46 J/cm^2 in (b) and (d) sintering/crystallization energies.

Figure 3.6. Sintered/crystallized TiO_2 thickness vs. sintering time at ablation energy = 2.3 J/cm^2, sintering/crystallization energy = 0.46 J/cm^2, repetition rate = 20 Hz, and different values of gas flow rate (a). Optical images of ANM-printed circles with different overlap ratio (b). Sintered/crystallized TiO_2 thickness vs. overlap (c).

Figure 3.7. Optical images of printed TiO_2 (for a-d) and ITO (e) patterns on SiO_2 substrate by ANM method.

Figure 3.8. SEM images of ablated ITO (a) and BTO (d) nanoparticles. STEM images of ablated ITO (b) and BTO (e) nanoparticles. The SEM images of sintered and crystallized ITO (c) and BTO (f).

Figure 3.9. Photographic images of TiO_2 patterns (200 μm line width) printed on (a) copper, (b) Al_2O_3, (c) PDMS, and (d) paper.

Figure 3.10. Real-time electrical resistivity measurement of 3 mm long lines while being printed by the ANM process as a function of the number of printed paths. Schematic illustration of deposited ITO line between two contact pads on a flexible PET substrate while the resistance is measured in real-time via a connected multimeter to pads (a). S/C E = 0.156 J/cm^2, RR = 10 Hz (b) S/C E = 0.156 J/cm^2, RR = 20 Hz (c) S/C E = 0.23 J/cm^2, RR= 10 Hz e) S/C E = 0.23 J/cm^2, RR = 20 Hz (d).

Figure 4.1. Schematic illustration of ANM process for dry printing Ag and ITO on flexible substrates (a). A 2 × 2 cm^2 printed Ag NFC tag antenna (four loops with a total length of ~32 cm and ~1.38 Ω cm resistance) connected to a self-power M24LR04E IC enabling communication with a phone device (b, c). Printed FHEs circuit on the polyimide substrate (d).

Figure 4.2. SEM images of laser-ablated Ag and ITO nanoparticles, respectively (a, d). BF-STEM images of laser-ablated Ag and ITO nanoparticles, respectively (b, e). SEM images of laser-sintered Ag (c) and ITO (f).

Figure 4.3. Cross-sectional image of printed and sintered silver nanoparticles on SiO_2 substrate via ANM process.

Figure 4.4. SEM images of morphological evolution of the printed Ag lines with different sintering laser energies as indicated on the bottom left corner of each figure (a-i). By increasing the sintering/crystallization energies, the porosity and resistance (shown upper right corner of each figure) of the printed lines decreased accordingly.

Figure 4.5. The thickness of sintered Ag (a) and ITO (b) as a function of the number of the printed paths at 4 different repetition rates 10 Hz, 20 Hz, 30 Hz, and 40 Hz.

Figure 4.6. Resistance of ANM-printed Ag lines as a function of the number of printed paths for four different repetition rates, including 10 Hz (a), 20 Hz (b), 30 Hz (c), and 40 Hz (d).

Figure 4.7. Schematic illustration of bending/cycling testing setup (a). Bending results of the ANM-printed Ag line for 1 cycle (b) and 50 cycles (c). (Initial resistance: red, 10.8 Ω cm; purple, 13.6 Ω cm; black, 22.5 Ω cm; green, 25 Ω cm; Blue, 22.4 Ω cm). Bending results of the ANM-printed Ag lines after 1000 cycles (d); (Initial resistance: red, 6.4 Ω cm; black, 20 Ω cm; green, 6.5 Ω cm; Blue, 8.3 Ω cm).

Figure 4.8. Digital image of fatigue setup used for stretching tests (a). Change of resistances in ANM-printed ITO strain sensor during 100 cycles at different strain levels (b). ITO bending results printed by ANM system for 1 cycle (c); Initial resistance: purple, 420 Ω cm; black, 550 Ω cm; red, 1300 Ω cm; green, 1600 Ω cm. The graph of normalized resistance variance at 0.19% strain during 9 cycles at 20 seconds (d) (inset is the optical image of the ITO strain sensor). SEM images of the ITO surface before (e) and after (f) stretching showing signs of crack formation (red ellipse).

Figure 4.9. Optical image of a bent temperature sensor (a). The inset image shows the top-view picture of the temperature sensor. Relative resistance changes at temperatures ranging from 30 °C to 80 °C (b).

Figure 4.10. Conductive electronics circuit and pattern of Ag printed by ANM process on polyimide substrate (a). Mounted SMD IC and LEDs on the circuit (b). Sequential turning on LEDs programmed by IC while 5V is applied (c-e). Circuit working under bending pressure (f).

Figure 5.1. Schematic of additive nanomanufacturing printer. Enlarged illustration of on demand Cu nanoparticle generation (a) and in-situ sintering of Cu nanoparticles on the surface of a substrate (b). SEM of ablated Cu nanoparticle by a pulse nanosecond laser (c). SEM of real time sintered Cu nanoparticles onto the PI kapton substrate (d).

Figure 5.2. Cu-based interdigital pattern arrays, AU logo, RF and NFC antenna, heater and square matrix printed on PI kapton substrates by ANM technique.

Figure 5.3. XRD plots of ablated Cu nanoparticles (a), and sintered Cu nanoparticles (b).

Figure 5.4. Resistance of 10 mm printed Cu as function of number of printed layers at different sintering powers for printing speed 2mm/s (a). Resistance of 20 layers printed Cu vs. sintering power at 10 mm/s printing speed (b). Resistance of Cu verses different layers printed (c).

Resistance of Cu verses printing speed while all other parameters kept constant (d). Thickness profile of printed Cu at 3 different printed layers (e). Measured resistivity based on data of graph c and e (f).

Figure 5.5. Plot of resistance variation versus day (a) and month (b) in air exposure for three different Cu printed on PI kapton showing the stable resistance in long period of time. Photograph of printed Cu samples (c).

Figure 5.6. Photograph image of printed-Cu pads (a), ~900Ω SMD resistor reflow soldered to the Cu pads (b), back of the substrate after reflow soldering (c), measured resistance of the SMD resistor (d).

Figure 5.7. Digital photo of 1cm by 1cm Cu printed on PI kapton before adhesion test (a). Digital photo of same printed Cu sample after adhesion test and removing of adhesion tape (b). Photograph image of Cu printed samples before and after scratching the surface with hand showing same resistance (c).

Figure 5.8. Initial and final resistance of Cu-printed 1 cm line samples at different bending cycles and radii (a-d). Photograph image showing well-functioning Cu-based flexible hybrid electronic at different bending radii (e, f)

Figure 6.1. Schematic illustration of the multimaterial additive nanomanufacturing (M-ANM) and dry printing method (a). An example of the process flow for printing a multimaterial conductor/insulator (Ag/Al_2O_3) hybrid structure (b-g). First, Ag antenna pattern is printed on the polyimide substrate (b). The Al_2O_3 layer is printed on a section of the Ag lines as an isolating bridge layer (c). Ag is printed crossing over the top of the Al_2O_3 layer to complete the NFC antenna device (d). Photograph of a completed circuit with a M24LR04E IC chip mounted on the printed antenna (e). Close-up optical image of the printed insulating Al_2O_3 bridge with the

crossed Ag lines (f). Image showing the flexibility of the multimaterial printed hybrid NFC antenna (g).

Figure 6.2. STEM images of BTO (a), TiO_2 (b), SnO (c), and ZnO (d) nanoparticles generated by M-ANM printer. SEM images of BTO (e), TiO_2 (f), SnO (g), and ZnO (h) sintered by ANM printer.

Figure 6.3. Raman spectra of sintered BTO (a), sintered TiO_2 (b), sintered SnO (c), and sintered ZnO (d). XRD plots of sintered BTO (e), sintered TiO_2 (f), sintered SnO (g), and sintered ZnO (h).

Figure 6.4. Optical image of side-by-side M-ANM printed Ag-SnO-ZnO lines (a). Optical images of Ag-ZnO (b), ZnO-SnO (c) and Ag-SnO (d) junction. (e, f) Optical images of BTO, ZnO, and TiO_2 printed on polyamide in a single run. Cross-section of printed Ag on top of TiO_2 (g). EDS elemental maps of printed TiO_2/Ag hybrid structure layer-by-layer (h-j).

Figure 6.5. Thickness (a), resistance (b), and resistivity (c) plots as a function of the number of printed layers ranging from 10 to 100 passes. Initial and final resistances of the printed Ag-lines under various bending radii and cycles, including 10^3 (d), 10^4 (e), 10^5 (f), and 10^6 (g) cycles. Digital photo of custom-made bending and cycling machine (h).

Figure 6.6. Digital photo of flexible Ag-ZnO photodetector arrays (a). 2D (b) and 3D (c) optical images of printed ZnO-based photodetector. Photoresponses of the sensor under various biased voltages (d) and light intensities (e). Photoresponses of the ZnO photodetector under various illumination intensities under different bending radii (f,g). Peak current of photodetector as a function of power density (h).

Figure 6.7. Digital photo of the M-ANM printed lines of flexible hybrid electronics (a). 3D optical image of the printed Al_2O_3 as the isolator layer between crossed Ag lines of the NFC

antenna (b). The height profile image printed Al_2O_3 section in the NFC antenna with a thickness of ~140 µm (c). Completed flexible hybrid electronic circuit with all mounted components (d). Digital photo of the circuit showing the red (e) or blue (f) LED switching via NFC communication controlled by a mobile phone.

Figure 7.1 Schematic illustration of trench formation on PI substrate via 248nm laser etching process (**a**). Schematic illustration of completed trench pattern formed on the PI substrate (**b**). In-situ Ag nanoparticles generation, and laser sintering of the delivered Ag nanoparticles onto the pre-formed trench (**c**).

Figure 7.2. Laser ablated 300 µm diameter craters in PI substrate at different number of laser pulses (**a**). Depth of ablation plotted as a function of number of pulse (**b**). 3D view of ablated crater using 40 laser pulses (**c**). Laser fluence of ablation was 0.48 J cm^{-2}.

Figure 7.3. 2D (**a**) and 3D (**b**) optical image of PI surface. 2D and 3D view of 10 µm trench formed on PI substrate (**c**) and (**d**), respectively. 2D and 3D view of 32 µm trench formed on PI substrate (**e**) and (**f**), respectively.

Figure 7.4. Depth of trench formed onto the PI substrate versus number of scanning path for three different laser fluences at four different repetition rates: 5 Hz (**a**), 10 Hz (**b**), 15 Hz (**c**) and 20 Hz (**d**).

Figure 7.5. Optical images of trenches formed by laser ablation using different nozzle diameter sizes ranging from ~200 µm to ~500 µm (**a**) to (**d**). 3D view of created trench via nozzle diameter size 500 µm (**e**). Surface profile of ~500 µm trench (**f**).

Figure 7.6. Schematic illustration of dry and pure Ag nanoparticles generated by laser ablation (**a**). SEM image of generated Ag nanoparticles (**b**). STEM image of ablated pure Ag nanoparticles (**c**). High-angle annular dark-field (HAADF) images of ablated pure Ag

nanoparticles (**d**). Schematic illustration of laser sintering and printing the Ag nanoparticles onto the trench (**e**). SEM image of sintered nanoparticles onto the trench (**f**).

Figure 7.7. Optical image of printed Ag on the surface of PI substrate (**a**). Surface morphology of printed line on PI substrate with ~ 60 µm height (**b**). Optical image (**c**) and surface morphology (**d**) of ~20 µm trench formed on PI substrate. Optical image (**e**) and surface morphology (**f**) of laser sintered Ag nanoparticles embedded in the trench formed on PI substrate.

Figure 7.8. Cycling results of SANM printed Ag lines with (**a**) and without (**b**) trench onto PI substrates, respectively.

Figure 7.9. Normalized change of resistance-cycle curves in response to 0.2 to 0.6 mm displacement for the ANM printed Ag on flat PI substrates for 3 different samples (**a**, **b**, **c**). Graphs of stretching test for 0.2 to 0.6 mm displacement on ANM printed Ag onto trench (**d**, **e**, **f**).

List of Abbreviations

AME	Additively Manufactured Electronics
ANM	Additive Nanomaufacturing
M-ANM	Multimaterial Additive Nanomaufacturing
FHE	Flexible Hybrid Electronics
IJP	Inkjet Printing
AJP	Aerosol Jet Printing
TiO_2	Titanium Dioxide
BTO	Barium Titanate
ITO	Indium Tin Oxide
Ag	Silver
Cu	Copper
Al_2O_3	Aluminum Oxide
ZnO	Zinc Oxide
MoS_2	Molybdenum Disulfide
$MoSe_2$	Molybdenum Diselenide
WSe_2	Tungsten Diselenide
WS_2	Tungsten Disulfide

CHAPTER 01

INTRODUCTION TO ADDITIVE MANUFACTURING-MACRO TO MICRO SCALE

1.1 Additive Manufacturing

Additive manufacturing (AM) processes, commonly known as 3D printing, builds up geometrically complex parts at the macroscale by adding micro-size layers of a material from a sliced computer-aided design (CAD) file [1]. This single-step process allows the design of custom parts and reduction of fabrication time, cost, and material consumption compared to conventional manufacturing methods. The AM can be classified into seven categories, as shown in **Figure 1.1**. Many of the currently available AM techniques are used for printing 3D parts at the macro scale. These methods, such as powder bed fusion and directed energy deposition are used for a variety of industries such as aerospace, automotive, healthcare, and consumer products. However, there are also some micro/nano additive manufacturing methods that operate as printed electronic technique. Inkjet and aerosol jet printing offer the possibility of micro-scale fabricating for variety of applications such as antennas, sensors, electronics devices, battery and storage.

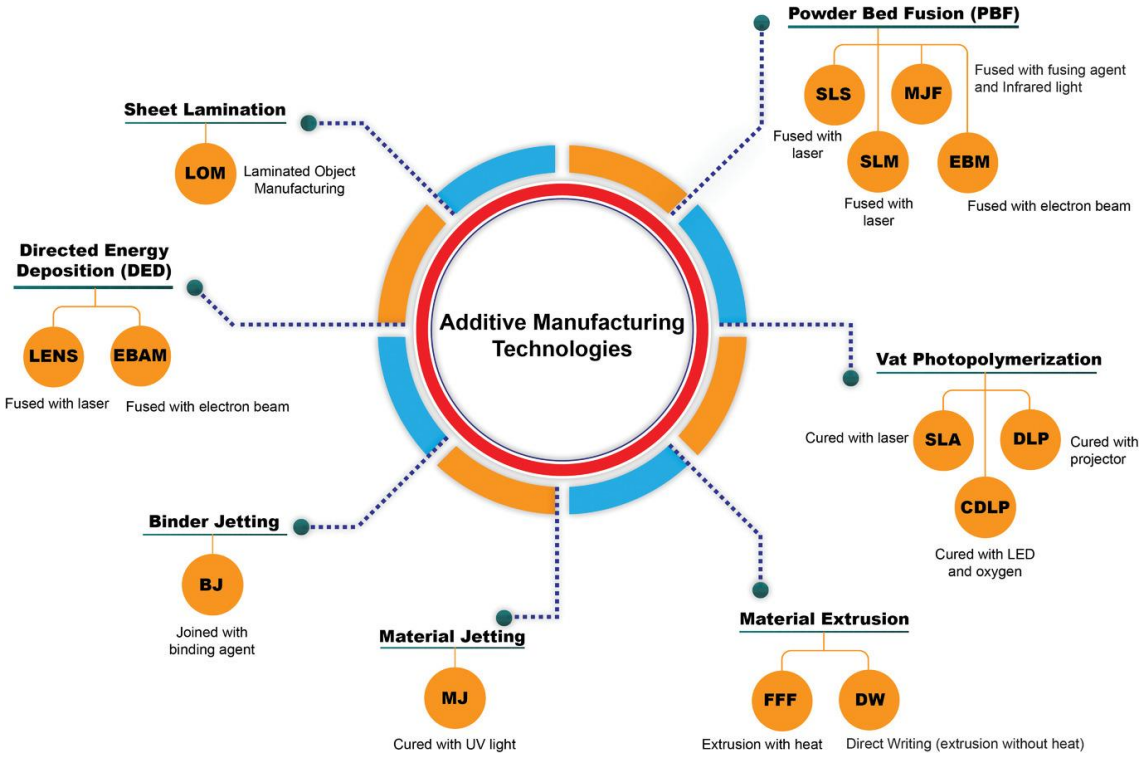

Figure 2.1 Classification of additive manufacturing technologies; the seven categories: material extrusion, vat photopolymerization, binder jetting, material jetting, sheet lamination, directed energy deposition, and powder bed fusion [1].

1.2 Additively Manufactured Electronics

Nowadays, flexible substrates are recognized as one of the key foundations of printed electronics due to their extreme light weight, ability to conform and bend, and their wide range of applications including in wearables electronics, flexible displays, soft robotics, energy and storage [2-12]. Conventional electronic manufacturing techniques such as photolithography and vacuum deposition, involve many steps such as mask design and fabrication, dry and wet etching that are expensive, time consuming, and environmentally harmful. In addition to that, these techniques rely on high-temperature processing, therefore are limited to conventional substrates such as rigid silicon wafers and printed circuit boards since these substrates are able to withstand the high temperatures and pressures [13, 14]. Flexible substrates are often made of polymer-based

materials, which cannot tolerate high temperature processes. These substrates can experience deformation, melting or warping at high temperatures which make them unusable for the intended application. Additionally, high temperature processes can damage active or passive components printed on the substrate. To avoid these issues, micro-scale additive manufacturing (AM) technologies such as inkjet printing (IJP) and aerosol jet printing (AJP) have emerged as a solution for printable electronics technology or additively manufactured electronics (AME) [15-20]. These technology can help to reduce the number of steps and the environmental impact of manufacturing, and can also enable the use of a wide range of substrates, including flexible and wearable substrates. The direct writing nature of AM eliminates waste of materials and many post processing steps of conventional methods. Many micro-scale additive manufacturing techniques use ink-based materials, such as conductive, resistive, and dielectric inks. Metal inks are needed to be annealed after printing so the nanoparticles sinter together for conductivity, and also to remove the solvents/additives in the inks [21, 22]. Here the annealing temperature is much lower than conventional manufacturing technique, which enables the use of flexible substrates in micro-scale AM techniques.

1.2.1 Inkjet Printing

Inkjet printing (IJP) relies on the ejection of ink droplets from a nozzle onto the substrate, which can be either rigid or flexible [23-26]. Conductive, dielectric, and polymeric inks are the most common materials used in IJP. Typically, the inks used for this technique are formulated with viscosities on the order of 1–20 centipoise (cp). The droplets of ink with different viscosities are ejected from the nozzle head and can be formed through either a continuous or a drop-on-demand (DOD) manner. In the continuous mode, a continuous pressurized stream of liquid droplets are ejected from the nozzle head. The DOD system is widely employed because of its

lower system complexity and higher accuracy of droplet displacement [27]. In a DOD system, the ink droplets are jet from the nozzle by pulses generated by a thermal resistor, a piezoelectric transducer, a thermal buckling or an acoustic wave.

1.2.2 Aerosol Jet Printing

The aerosol jet printing (AJP) is a relatively new printing technique and it has been developed in recent years [19, 28]. This method uses a fine mist of material particles (instead of liquid ink) suspended in a gas. The size of particles is usually 1–5 μm in diameter. The aerosol jet print head that has a nozzle that produces the aerosol, and a gas flow that directs the aerosol towards the substrate. The print head also has a high-voltage power supply that charges the material particles as they pass through the nozzle. The charged particles are then directed towards the substrate, where they are attracted to a set of electrodes that have the opposite charge. This allows for precise control over the placement of the material particles on the substrate, which is useful for creating complex and high-resolution structures. Compared to IJP, AJP is compatible with a wide range of materials, including high-viscosity inorganic inks, organics, and high aspect-ratio carbon nanotube (CNT) solutions [29]. In AJP, the sheath gas (usually nitrogen) in the print head prevents the nozzle from clogging and keeps the aerosol beam tightly focused.

1.2.3 Disadvantages of Inkjet and Aerosol Jet Printing

In both systems, the use of solvents and additives makes the inks impure and complex to handle. As a result, solvents removal and post thermal annealing make the device manufacturing process complicated and expensive [30]. In addition, the printed material should be in a viscous fluid state, making it difficult to obtain materials with the appropriate viscosities. The development of new source materials for IJP and AJP has become a priority for many researchers in order to enable the printing of functional devices. Determining optimal print parameters of ink is often a

sensitive process. Additionally, optimal printing parameters for a given ink do not, in general, translate to new materials, demanding an extensive, empirical optimization over a broad phase space for each additional ink or material. Therefore, printing multifunctional materials (e.g., ferromagnetic, piezoelectric) and hybrid structures is still a major challenge [30-40].

1.2.4 Multi-Materials Printing

Multimaterial printing refers to print multiple materials during a single build process. Most devices and structures with sophisticated functionalities, such as electronics, optoelectronics, and sensors, typically require multimaterial deposition. Thus, there are emerging needs for printing methods that allow multimaterial printing in multilateral configurations. IJP and AJP techniques have been mostly successful in printing a limited single material in a single process step. A few printing methods have also been reported that are capable of printing multimaterials. For example, Skylar-Scott et al. reported a micrometer-scale printing strategy by fast switching between viscous materials which are extruded through a single nozzle. Wanjun Liu et al. [37] developed an extrusion-based multimaterial bioprinting platform capable of depositing multiple coded bio-inks in a continuous manner with switching between different reservoirs. Ke Sun et al. showed 3D interdigitated microbattery architectures by printing concentrated lithium oxide-based inks. Although these extrusion-based printing methods have been used to fabricate functional devices, the construction of multimaterial architectures often involves sequentially printing individual materials using multiple nozzles. Besides the limited availability of the source materials for printing, the drawbacks of printing one material at a time include the need for careful alignment of each nozzle as well as start-and-stop ink flow on demand without introducing defects.

1.3 Outline of Dissertation

This dissertation introduced several original findings to address the challenges of current additively manufactured electronics technique.

In Chapter 01, Additively manufactured electronic techniques are introduces as the new area of printed electronics. The challenges and disadvantages of current AME techniques such as inkjet and aerosol jet printing have been discussed.

In Chapter 02, A rapid direct laser crystallization and mask-free large-scale patterning of MoS_2 and WSe_2 crystals on PDMS substrates has been showed. A thin layer of stoichiometric amorphous 2D film is first laser-deposited via pulsed laser deposition (PLD) system onto the flexible substrates followed by a controlled crystallization and direct writing process using a tunable nanosecond laser (1064 nm). The process parameters and mechanisms are discussed in detail. Electrical and optical characterizations are performed to confirm the quality of crystallized 2D materials.

In Chapter 03, A novel laser-based additive nanomanufacturing (ANM) system has been reported which is capable of on-demand generation of nanoparticles. These nanoparticles can serve as the building blocks for real-time sintering and dry printing a variety of multifunctional materials and patterns. The capability of printing different functional materials on various rigid and flexible substrates is discussed. Additionally, the process–structure relationship of the printed materials is investigated.

In Chapter 04, Silver-based flexible hybrid electronics (FHE) and sensors printed by ANM on flexible substrates is reported. Different FHE designs are fabricated and tested to check the performance of the devices. Mechanical reliability tests including cycling, bending, and stretching are employed and the results confirm the expected performance of the printed samples under different strain levels.

In Chapter 05, An ink-free and dry additive nanomanufacturing technique to print highly conductive copper on flexible polyimide kapton substrate has been introduced. Resistance of printed Cu measured in 5 months showed negligible variation, confirming the good stability of printed Cu in long time. 5B classification of ASTM adhesion test confirmed the good adhesion between the sintered Cu and polyimide kapton substrate. To demonstrate the mechanical reliability of printed Cu, different bending radii and cycles were tested and results showed the excellent reliability of samples. The ANM printer was used to print Cu-based patterns, flexible hybrid electronics, antenna and sensor that has wide range of applications in oil and gas industry, flexible electronics, medical and energy storage.

In Chapter 06, A multimaterial additive nanomanufacturing (M-ANM) technique is demonstrated. Lateral and vertical hybrid structures and devices printed by M-ANM. ZnO photodetectors with Ag electrodes and multimaterial Ag-Al_2O_3 FHE circuits were printed and tested as practical applications. This unique M-ANM technique was used to print a variety of materials such as Ag, BTO, TiO_2, SnO, ZnO, and Al_2O_3 that can be used for broad applications ranging from flexible electronics, optoelectronics, energy storage and harvesting, space, and medical applications enabling the future internet of things (IoT).

In Chapter 07, we showed our technique is capable of subtractive and additive manufacturing as well. For this use, the ANM machine first ablated arbitrarily patterns to form any trenches and channels from the polyimide substrate using a subtractive technique, and then filling the channels using the ANM printer.

CHAPTER 02

Rapid Laser Nanomanufacturing and Direct Patterning of 2D Materials on Flexible Substrates—2DFlex

2.1 Introduction

Compared to conventional rigid devices, stretchable and flexible devices can be attached to irregular and deformed surfaces. Such devices are gradually used in emerging new areas such as wearable devices, soft robotics, electronics skin and flexible display.[41] New biomedicine and healthcare applications of flexible and stretchable devices have been emerged due to intrinsic mechanical properties, excellent compliance, biocompatibility and conformability to tissue surfaces.[42]

Over the past decade, 2D quantum materials have been considered as promising candidates for future flexible and transparent nanoelectronics applications due to their outstanding mechanical, electrical, and optical properties.[43-49] In addition, these atomically-thin sheets afford the ultimate thickness scalability desired in a variety of essential material categories including semiconductors, insulators, conductors, and superconductors.[50-52] Among various 2D materials such as graphene, transition metal dichalcogenides (TMDs), and boron nitride (BN), heterostructures have shown a great potential to realize electronic, optoelectronic, and photonic devices with superior performance. Accordingly, flexible photonics is now enabling a wide range of emerging applications including board-level optical interconnects,[53-56] optomechanical tuning,[57-59] epidermal monitoring, [60] strain sensing [61], and conformal photonics. [62, 63]

Currently, the inability to directly growth and patterning of 2D materials on flexible substrates and lack of large-area and transfer-free processes have made the practical realization of 2DFlex in the aforementioned applications challenging. The majority of electronic device studies involving MoS_2 crystals use chemically or mechanically exfoliated 2D sheets.[64] At present, only relatively small samples of these 2D materials can be generated with mechanical exfoliation. Poor layer thickness and size uniformity, uncontrolled nanosheet orientations, and contamination between layers are some examples that prevent viability of chemical exfoliation for its commerciality.[65-67] Chemical vapor deposition (CVD) and laser-assisted synthesis are common approaches for generating high quality, large area 2D thin films.[68-71] However, CVD and laser-assisted synthesis are not amenable to stretchable and flexible substrates due to high growth temperatures (approximately 700–900°C) required for the decomposition of TMD precursor gases and molecular transformation to crystalline structures. Most recently, magnetron sputtering of TMD targets has been demonstrated to directly grow large-area uniform films at low temperatures (250°C). These films often suffer from a lack of stoichiometry and good crystallinity. Researchers used a broadband pulsed flash lamp and laser annealing to crystallize such as-deposited amorphous sputtered layers.[47, 72] As 2D devices become more complex (e.g., numerous 2D materials, more layers, specific shapes, etc.), the patterning steps (lithographically and subsequently etch away unwanted areas of 2D material) can become economically costly and time-consuming.[73] Material printing and additive manufacturing have emerged as new fabrication concepts that allow for the transfer of liquid-based 2D inks onto flexible substrates for device printing.[74, 75] For instance, inkjet printing based on commercial jet printing devices is widely used because of its direct-writing, low-temperature, mask-free, and its compatibility with flexible substrates.[75] However, the ink is made via chemical exfoliation and salary formation

techniques that highly suffer from contamination, nonuniformity and precise thickness control issues. Moreover, the nozzles used in inkjet printing can be blocked frequently. To the best of our knowledge, the ability to directly synthesize crystalline TMDs with any complex shape and pattern on flexible substrates has remained elusive.

Here, we report a novel approach to directly integrate crystalline patterns of 2D materials onto the flexible substrates enabling the future conformal and transparent optoelectronic and photonic devices. Photo-thermal heating and reaction induced by laser can transform 2D materials from amorphous phase to crystalline phase. Controlled crystallization and direct writing processes are achieved by a precise laser processing of stoichiometric amorphous 2D film on the flexible substrates. The influence of laser pulse duration, the number of pulses and also thickness of deposited 2D amorphous layer on the crystallization of 2D materials is discussed. This laser crystallization method opens up new routes to synthesize 2D materials with every desired complex shape on flexible substrates.

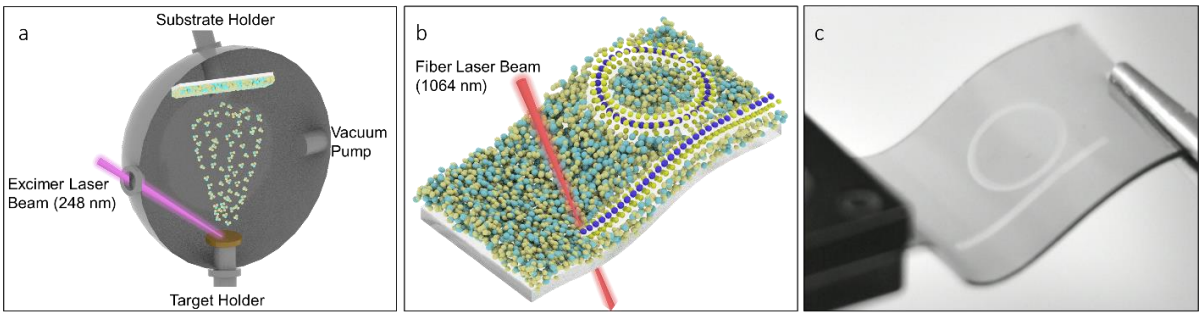

Figure 2.1 Schematic diagrams of stoichiometric deposition of amorphous 2D materials on PDMS via pulsed laser deposition (**a**) and laser crystallization of amorphous 2D materials (**b**). (**c**) Photograph image of a MoS_2 modulator crystallized by laser crystallization method.

2.2 Results and discussion

Figure 2.1 shows the schematics representation of the laser crystallization and patterning process of 2D quantum materials on flexible substrates. In this process, a pulsed laser deposition (PLD) system (**Figure 2.1**a) was used to deposit thin films of stoichiometric amorphous MoS_2 and WSe_2 with different thicknesses onto the PDMS substrates. Dense 1-inch diameter pellets of hardly pressed MoS_2 and WSe_2 powders were used as ablation target and an excimer laser (COMPexPro, KrF) with λ=248 was used for target ablation at a 40° angle of incidence and 5 Hz repetition rate. Targets (MoS_2 and WSe_2) were placed on a target carousel inside a spherical chamber (21 inches in diameter). The resultant laser spot size and fluence on the target were 2 × 5 mm and 1.5 J cm^{-2}, respectively. The pressure inside the ablation chamber was lowered to 5 × 10^{-6} Torr for deposition, and the substrate-target distance was set at 7 cm. Polydimethylsiloxane (PDMS) was used as flexible substrates. As-deposited amorphous on PDMS substrate was transferred into a costume-designed environmental processing chamber for subsequent laser crystallization (**Figure 2.1**b) and pattering processes under the argon gas environment at atmospheric pressure and room temperature. To avoid surface oxidation during the crystallization process, the chamber was first flushed by argon gas for a few minutes and then the argon gas flow rate was kept constant at 200 sccm. For crystallization and patterning, the laser beam from a nanosecond pulsed fiber laser with λ=1064 nm (130 W, tunable nanosecond pulses, 5–2000 ns in 63 waveforms, with a pulse energy from 0.04 to 1.57 mJ and a repetition rate ranging from 1 Hz to 4160 KHz.) was directed to the center of a galvo scanner with a 13 μm focal point. The design and control of process parameters (e.g. power, pulse duration, number of pulses) for each specific pattern was controlled by a laser marking software (Laser Studio Professional.)

The low thermal conductivity of the amorphous 2D materials and the PDMS substrate results in a low thermal conductance and hence a poor heat transfer. Therefore, it is essential to utilize a crystallizing process that can overcome these limitations. Time-resolved infrared laser crystallization method allowed us to controllably couple a precise amount of energy and hence heat the amorphous 2D layer for selective phase transformation. In this controlled laser-material interaction process, the heat penetration depth was controlled in a way that there is enough time for thermal energy to crystallize the amorphous 2D material for crystallization without damaging the underlying PDMS substrate. Accordingly, a tunable nanosecond fiber laser (1064 nm) was used since the PDMS has no (minimal) absorption in this wavelength and provided a great processing control. [33] This is critical for minimizing the laser interaction with the substrate during the crystallization process. Comprehensive experiments were performed to find the influence of laser pulse width (ranging from 10 ns to 261 ns), number of laser pulses, and the thickness of the as-deposited amorphous layer on the crystallization of 2D materials. We didn't use pulse duration more than 261ns since in most cases of experiments, it caused harshly burning of the PDMS substrate. The symbols in each panel of **Figure 2.2** indicate the locations processing parameters where good 2D MoS_2 and WSe_2 crystals were obtained. The curves are fitted to provide processing guidance. Employing the process parameters on the curves for each pulse-width resulted in the formation of high-quality 2D crystals without creating any damage on the PDMS substrate. However, the laser parameters to the right and above of the curves in **Figure 2.2**a, b resulted in the evaporation of the amorphous 2D materials. On the other hand, employing process parameters to the left and below of the curves did not affect the amorphous layer. Increasing the pulse width of the laser required less laser power and pulse number for crystallization, and vice versa. At shorter pulse durations, the width of the crystalline lines was

smaller than the lines crystallized by the longer laser pulse-widths. This was attributed to heat formation and dissipation time. When the laser pulse-width is small (e.g., 10 ns), the generated heat has less time to dissipate in the amorphous materials, hence inducing a smaller heat-affected zone. In contrast, higher laser pulse-width provides a longer time for heat formation and dissipation to an area outside the laser spot causing a larger heat-affected zone and hence larger crystalline line widths. According to experimental observations, the laser pulse-widths beyond 261 ns always resulted in the evaporating of the amorphous materials or damaging the PDMS substrate. These allowed us to identify the best processing conditions for further crystallization and patterning purposes. From these experiments, the laser power of 33 W, pulse duration of 108 ns, and 20 laser pulses per spot were used for patterning of 2D materials on the PDMS for the subsequent studies.

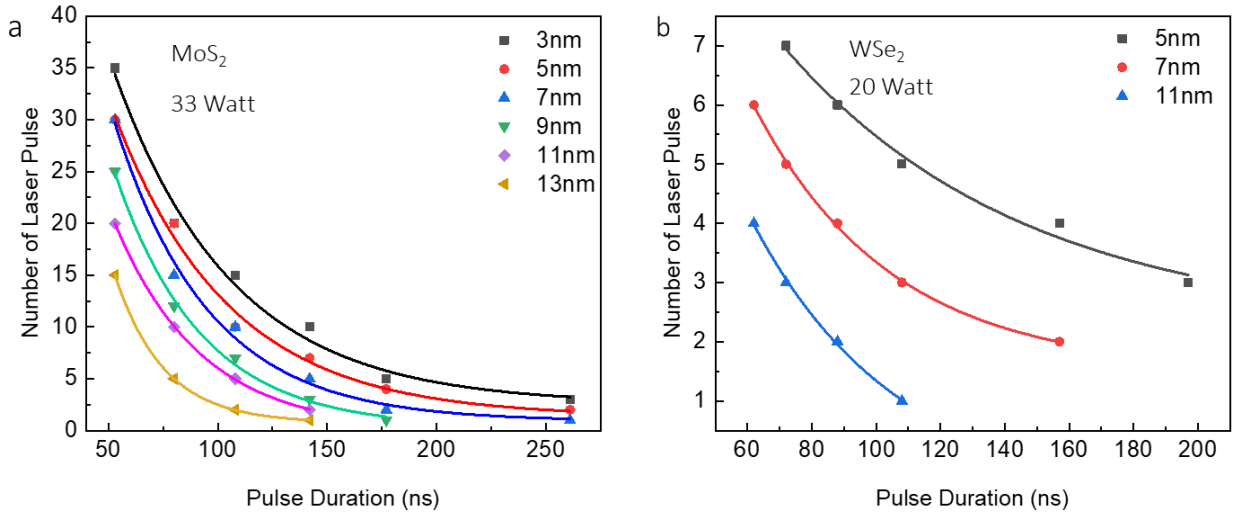

Figure 2.2 The effect of laser interactions with amorphous 2D MoS_2 (a) andWSe_2 (b). Each graph represents the effect of laser pulse-width and number of pulses on the crystallization of amorphous layers with various thicknesses.

Raman spectroscopy was used to monitor the crystallization quality of the laser processes amorphous materials on the PDMS substrates. The Raman spectra were obtained at room temperature using a 532nm excitation laser from PDMS substrate (**Figure 2.3**a, d), amorphous

MoS_2/WSe_2 layer coated on the PDMS substrate (**Figure 2.3**b/e), and laser crystallized MoS_2/WSe_2 layer on the PDMS (**Figure 2.3**c/f), as shown in **Figure 2.3**. As it demonstrated in **Figure 2.3**a,b/d,e the Raman spectra of PDMS and Amorphous laser on PDMS are similar since amorphous MoS_2/WSe_2 does not have any specific Raman signature. However, the active Raman modes of MoS_2/WSe_2 crystals including E^1_{2g} at ~378 cm^{-1} and A^1_g at ~403 cm^{-1}/ A^1_g at ~ 250 cm^{-1} are clearly observed in **Figure 2.3**c/f after the laser crystallization process.

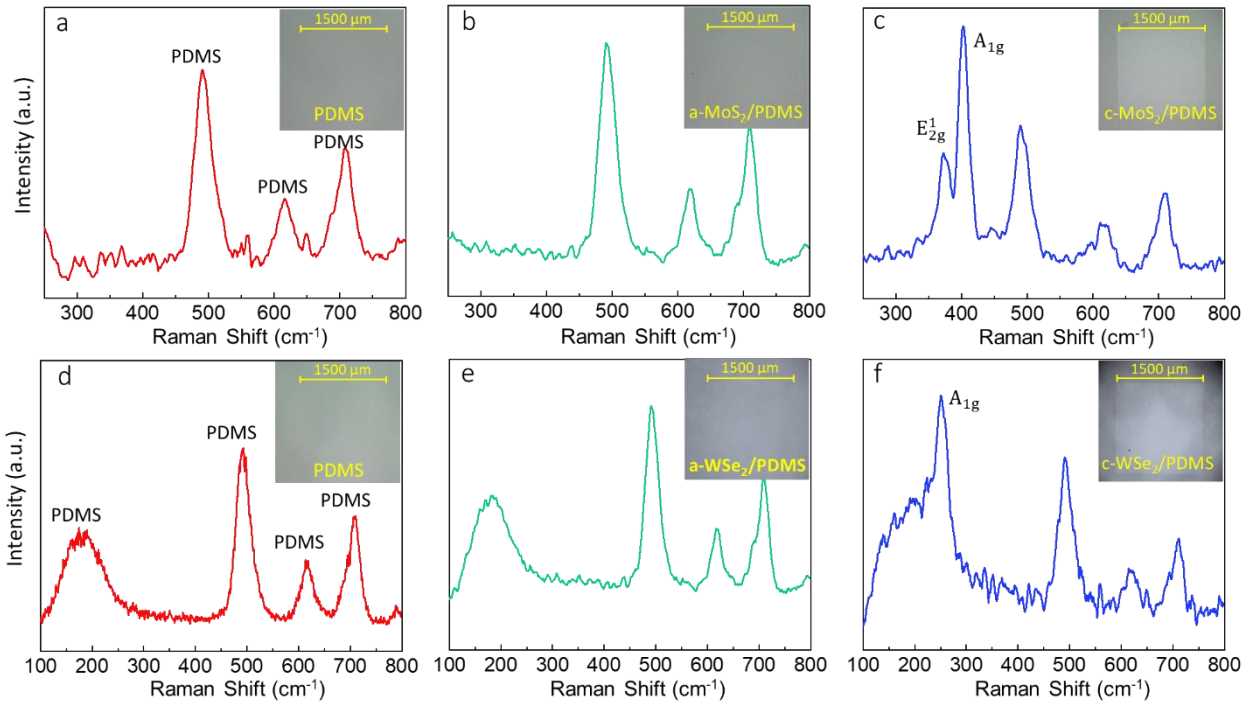

Figure 2.3. Optical images and Raman spectroscopy of the samples before and after the laser deposition and crystallization processes. Optical images and Raman spectra of PDMS (**a**, **d**), amorphous MoS_2/WSe_2 on PDMS (**b**, **e**), and crystalline MoS_2/ WSe_2 on PDMS (**c**, **f**). Both the pure PDMS and amorphous 2Dmaterial on the PDMS substrate showed similar Raman peaks since the amorphous layer does not have any Raman fingerprints. The laser crystallized materials, however, show very sharp Raman signatures at 375 and 405 cm^{-1} corresponding to crystalline MoS_2 and at 250 cm^{-1} corresponding to crystalline WSe_2.

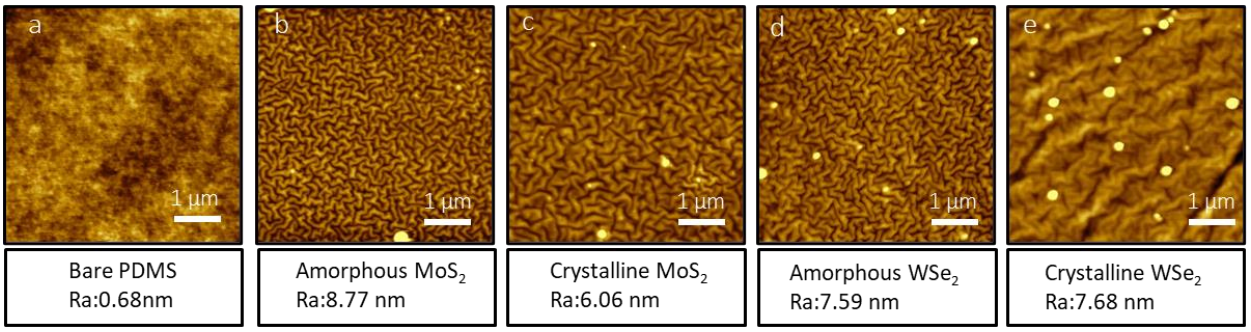

Figure 2.4. Atomic force microscopy (AFM) image and roughness (Ra) of bare PDMS (a), as-deposited amorphous MoS_2/PDMS by PLD system (b), MoS_2/PDMS crystallized (c), as-deposited amorphous WSe_2/PDMS (d) deposited by PLD system, and MoS_2/PDMS crystallized by laser crystallization process (e).

Figure 2.4(a-e) shows the AFM topography of bare PDMs, amorphous and crystalline for MoS_2 and WSe_2. The surface roughness of PDMS is 0.68 nm. During deposition of amorphous 2D quantum materials, PLD increased the roughness to 8.77 nm and 7.59 nm for MoS_2 and WSe_2, respectively. After crystallization, the roughness was 6.06 nm and 7.68 nm MoS_2 and WSe_2, respectively. Surface wrinkling are created because of ultrahigh vacuum deposition as well as laser-produced plasma during PLD process.[76] To understand the crystallization temperatures of our amorphous layers in an equilibrium processing condition, amorphous WSe_2 and MoS_2 layers (with thickness of 3, 5, 7,9,11 nm) were deposited onto SiO_2 substrate via PLD and baked in an environmental tube furnace under atmospheric argon pressure. These results were useful in comparing with our nonequilibrium laser crystallization method. The results showed that for obtaining crystalline 2D materials (MoS_2 and WSe_2) with the same quality as those fabricated by laser crystallization approach, the required crystallization temperatures for MoS_2 and WSe_2 were around 600°C. This well-beyond the temperature stability of the PDMS substrate (~200°C). In addition, the observations showed that the furnace temperatures above 700°C caused decomposition and evaporation of 2D materials from the silicon substrates. These results indicate the importance of a time-resolved nonequilibrium laser processing approach in the crystallization

of 2D materials on flexible platforms without damaging the underlying substrates. This approach provides a sufficient temperature in a short time so that the amorphous layer crystallizes without heat conduction and damage of the flexible substrate.

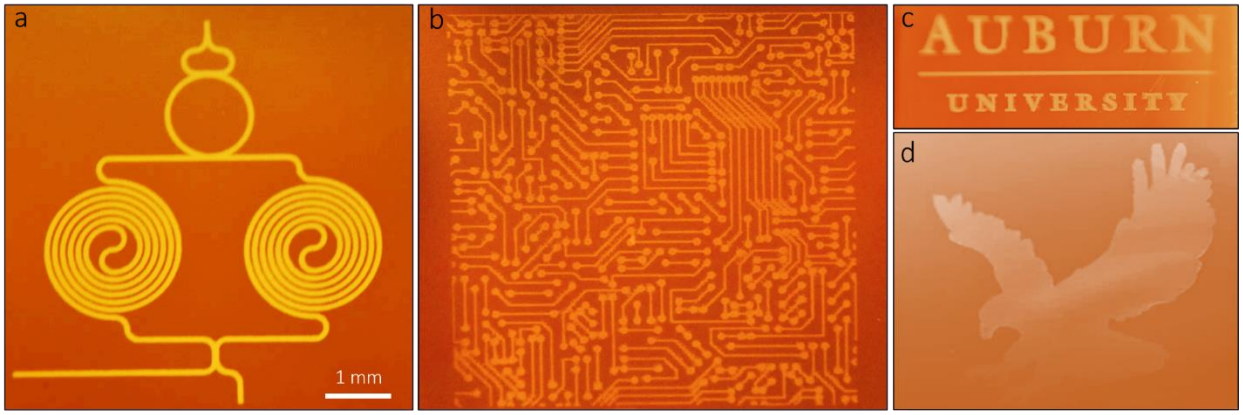

Figure 2.5. Examples of patterned 2D crystals on the PDMS substrates. A photonics Mach Zehnder interferometer (a), an electronics circuit board (b), Auburn University logo (c) and eagle image (d) fabricated by laser crystallization of amorphous WSe_2 layer on PDMS substrates. Scale bar is same for all pictures.

The ability to directly integrate 2D and other quantum materials with desired patterns and shapes onto the flexible substrate is highly demanded applications ranging from electronics to photonics and energy to sensing applications. Utilizing our approach, we demonstrated the formation of various 2D material-based patterns on the PDMS substrate. For instance, **Figure 2.5**a, b, c and d demonstrate the fabricated crystalline WSe_2-based photonics Mach Zehnder interferometer, an electronic circuit board, Auburn University logo and an eagle, respectively. Our crystallization and pattering process allows the realization of complex and arbitrary patterns on flexible substrates.

The electrical properties of the crystallized samples were measured by depositing contact electrodes and measuring their I-V characteristics. To fabricate such a device, we first crystallized a large area of amorphous MoS_2 on PDMS followed by the deposition of gold contacts through photolithography and sputtering processes. **Figure 2.6**a shows a photograph image of fabricated devices. **Figure 2.6**b shows a three-dimensional illustration of crystalline 2D materials with two gold contacts (inset image is the optical image of the fabricated device). To achieve an insight into the flexibility of the fabricated device, the IV and bending tests were performed. **Figure 2.6**c shows the IV characteristics of a 5 nm c-MoS_2 device. The resistance decreased gradually in inverse proportion to the bending radius (**Figure 2.6**d). A considerable extent of decrease in electrical conductivity can arises since defects can be introduced into the c-MoS_2 crystal lattice. Bending the film (r=4mm<bending radius<r = 20 mm) led to increase in R compared to the flat condition (8 MΩ) due to reduced charge–carrier mobility and mechanical deformation of 2D c-MoS_2.

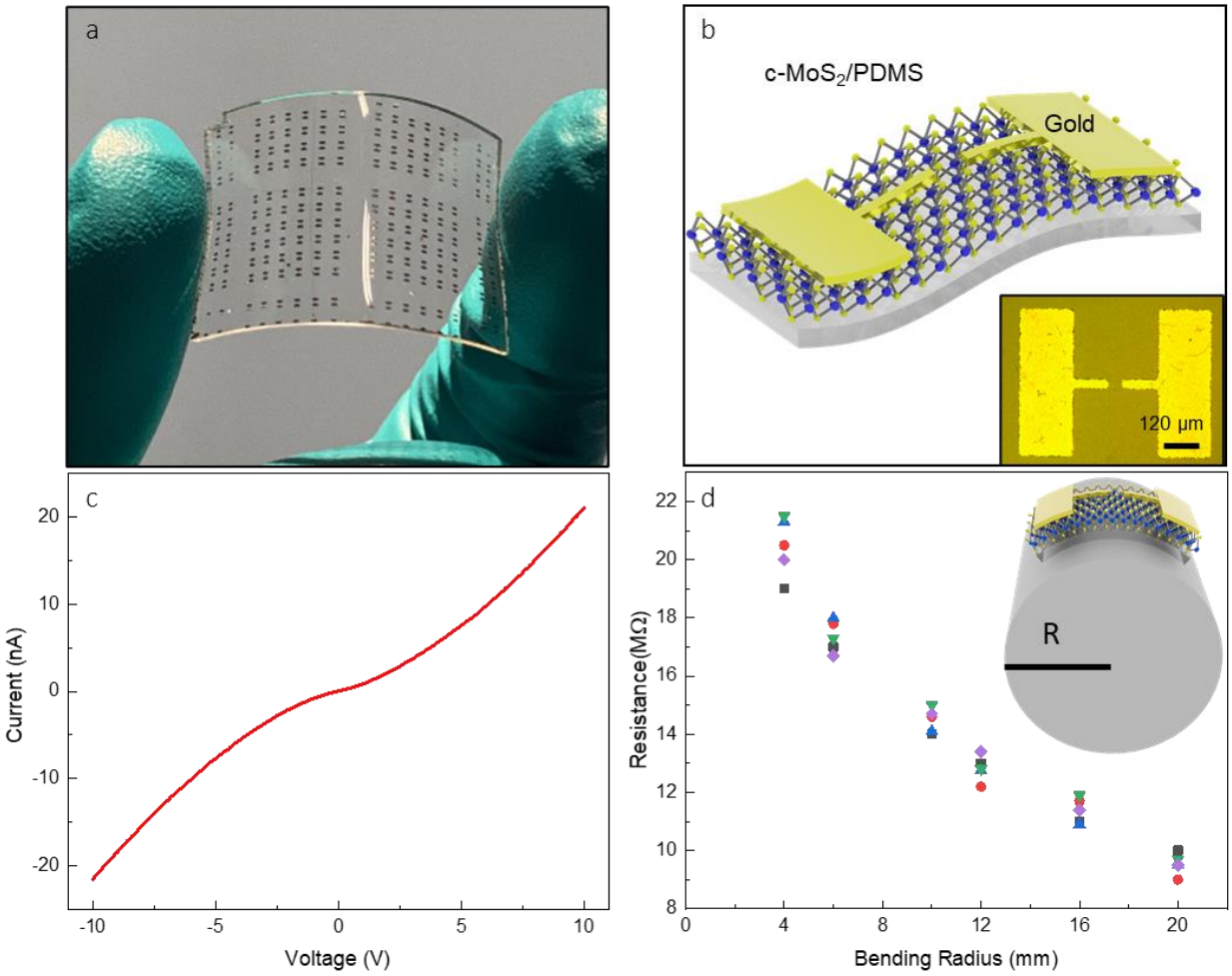

Figure 2.6. A photograph image of fabricated devices (a), schematic illustration of crystalline 2D materials used as photodetector (b), IV characteristics of a 5nm thick crystallized MoS_2 layer device (c), resistance of a fabricated device according to the bending radius under tensile strain (d).

2.3 Conclusion

In summary, we presented a novel direct laser crystallization and large-area patterning of amorphous 2D materials (MoS_2, WSe_2) deposited by pulsed laser deposition on PDMS flexible substrate. We demonstrated that a tunable nanosecond (1064 nm) laser has allowed us to controllably couple a precise amount of energy and hence heat the amorphous 2D layer for selective phase transformation. In this controlled time-resolved laser-material interaction process, the heat penetration depth was controlled by changing the pulse duration and number of

laser pulse in each spot in a way that there is enough time for thermal energy to crystallize the amorphous 2D material for crystallization without damaging the underlying PDMS substrate. Furthermore, we showed the capability of this laser crystallization process to make any complex patterns.

CHAPTER 03

Additive Nanomanufacturing of Multifunctional Materials and Patterned Structures: A Novel Laser-Based Dry Printing Process

3.1 Introduction

The manufacturing complexity, cost, and excessive wastage of the conventional device micro/nanomanufacturing processes as well as their incompatibility with stretchable and dissolvable substrates have resulted in considerable efforts for developing new advanced manufacturing methods to overcome these challenges.[77] Additive manufacturing (AM) processes, commonly known as 3D printing, have attracted enormous attention in various industries such as aerospace, medical, automotive, fashion, and the environment.[78-82] Typically, AM builds up geometrically complex parts at the macroscale by adding micro-size layers of material from a sliced computer-aided design (CAD) file.[83-85] This single-step process allows the design of custom parts and reduction of fabrication time, cost, and material consumption compared to conventional manufacturing methods. The ability to fabricate complex structures and devices via AM and materials printing technologies has led to a paradigm shift in engineering design and product realization. However, the limited choice of functional precursors and versatile printing techniques in the current AM technology are among the major challenges that significantly limit their applications in printing hybrid structures and devices with complex functionalities, including electronics, optoelectronics, flexible and wearable sensors, and energy conversion and storage devices.[86-92]

Among the AM categories,[31] inkjet and aerosol jet printing offer the possibility of fabricating a few electronics and functional devices.[93] Inkjet printing (IJP) relies on the ejection of ink

droplets from a nozzle onto the substrate, which can be either rigid or flexible.[23-26] Conductive, dielectric, and polymeric inks are the most common materials used in IJP. Typically, the inks used for this technique are formulated with viscosities on the order of 1–20 centipoise (cp). The aerosol jet printing (AJP) is a relatively new printing technique developed in recent years.[19, 28] In this process, liquid inks are first atomized into small droplets of ~1–5 μm in diameter, then transported to the printing head through a carrier gas. Compared to IJP, AJP is compatible with a wide range of materials, including high-viscosity inorganic inks, organics, and high aspect-ratio carbon nanotube (CNT) solutions.[29] In AJP, the sheath gas (usually nitrogen) in the print head prevents the nozzle from clogging and keeps the aerosol beam tightly focused.

In both systems, the use of solvents and surfactants/additives makes the inks impure and complex to handle. As a result, solvents removal and post thermal annealing make the device manufacturing process complicated and expensive.[30] In addition, the printed material should be in a viscous fluid state, making it difficult to obtain materials with the appropriate viscosities. The development of new source materials for IJP and AJP has become a priority for many researchers in order to enable the printing of functional devices. Determining optimal print parameters of ink is often a sensitive process. In addition, optimal printing parameters for a given ink do not, in general, translate to new materials, demanding an extensive, empirical optimization over a broad phase space for each additional ink or material. Therefore, printing multifunctional materials (e.g., ferromagnetic, piezoelectric) and hybrid structures is still a major challenge.[30-40] Direct printing of multifunctional materials and composites such as TiO_2, [94-100] BTO, [101-103] ITO [87, 104] opens a new pathway toward the direct manufacturing of devices with complex functionality. This has led to the emergence of laser-based additive nanomanufacturing

(ANM) as a promising approach that could enable the synthesis and patterning of a variety of materials with micro/nanoscale resolutions.[105-113]

Here, for the first time, we successfully introduced a single step ANM approach that enables the dry printing of a variety of multifunctional materials such as TiO_2, BTO, and ITO on different substrates using a laser source. Our novel printing method is based on the in-situ and on-demand generation of metastable nanoparticles via the nonequilibrium pulsed laser ablation process that can be laser sintered/crystallized in real-time to form desired patterns and devices. Our novel laser-based ANM process possesses the capability to print a wide range of dry, contaminations-free, and intrinsically pure nanoparticles at room temperature and at atmospheric pressure. This approach also offers the flexibility of printing onto different types of substrates, including metals, ceramics, plastics, paper, and flexible substrates such as PDMS and PET.

3.2 Experimental Method

3.2.1 Experimental Setup

Figure 3.1 shows the schematic of our designed and developed ANM apparatus. The system consists of a pulsed excimer laser (KrF, wavelength 248 nm), a beam splitter, two adjustable turning mirror, two lenses with 150 mm focal length, an ablation chamber with a nozzle, a target and its holder, an X-Y computer-controlled positioning system, attenuators, and controlled Ar/N_2 gas connected to the cylindrical holder by a feeder pipe. A substrate is placed onto the X-Y motion table. The separation between the nozzle and the substrate is kept constant at 0.5 mm. All the components are placed on an optical table.

The ANM fabrication process involves five key steps, as shown in **Figure 3.1**a, as listed in this paragraph. (1) Splitting pulsed excimer laser beam: the 248 nm excimer laser beam is divided into ablation and sintering/crystallization beams by a beam splitter (70% reflection, 30%

transmission), and then the two beams energies are further tuned and guided toward mirrors 1 and 2, respectively. (2) Pure amorphous nanoparticles generation: the ablation laser beam is directed toward a sealed environmental chamber using mirror 1. The ablation laser beam is then focused onto the surface of the target by a UV fused silica convex lens to generate pure amorphous nanoparticles. The target is rotated by a step motor at an angular speed of ~3 rad/s to avoid laser piercing. During the interaction of the ablation laser beam with the target, a laser-plasma plume is formed. The interaction of this plume with the background gas results in thermalization and condensation of the plume leading to the formation of nanoparticles.

Figure 3.2 shows the scanning electron microscopy (SEM) and scanning transmission electron microscopy (STEM) images of the laser-generated amorphous TiO_2 nanoparticles with a size distribution of around 3-7 nm. (3) Nanoparticles delivery: a stream of produced pure amorphous nanoparticles are delivered to a central point beneath the nozzle head using a carrier gas flow. (4) Sintering/crystallization of produced pure amorphous nanoparticles: the sintering/crystallization laser beam is focused above the surface of the substrate using mirror 2 and a convex lens. The nanoparticles are then sintered and crystallized on the surface of the substrate. Optical attenuators are used inside cylindrical holders to attenuate and tune the energy of ablation and sintering/crystallization laser beam, i.e., to reduce optical power. (5) Stage scanning: the substrate placed on an X-Y stage, which is computer programmed to move and form any pre-defined patterns. The operation principle of the system is similar to the laser beam directed energy deposition (LB-DED) processes;[85, 114, 115] however, the major difference here is the in-situ and on-demand formation of nanoscale building blocks.

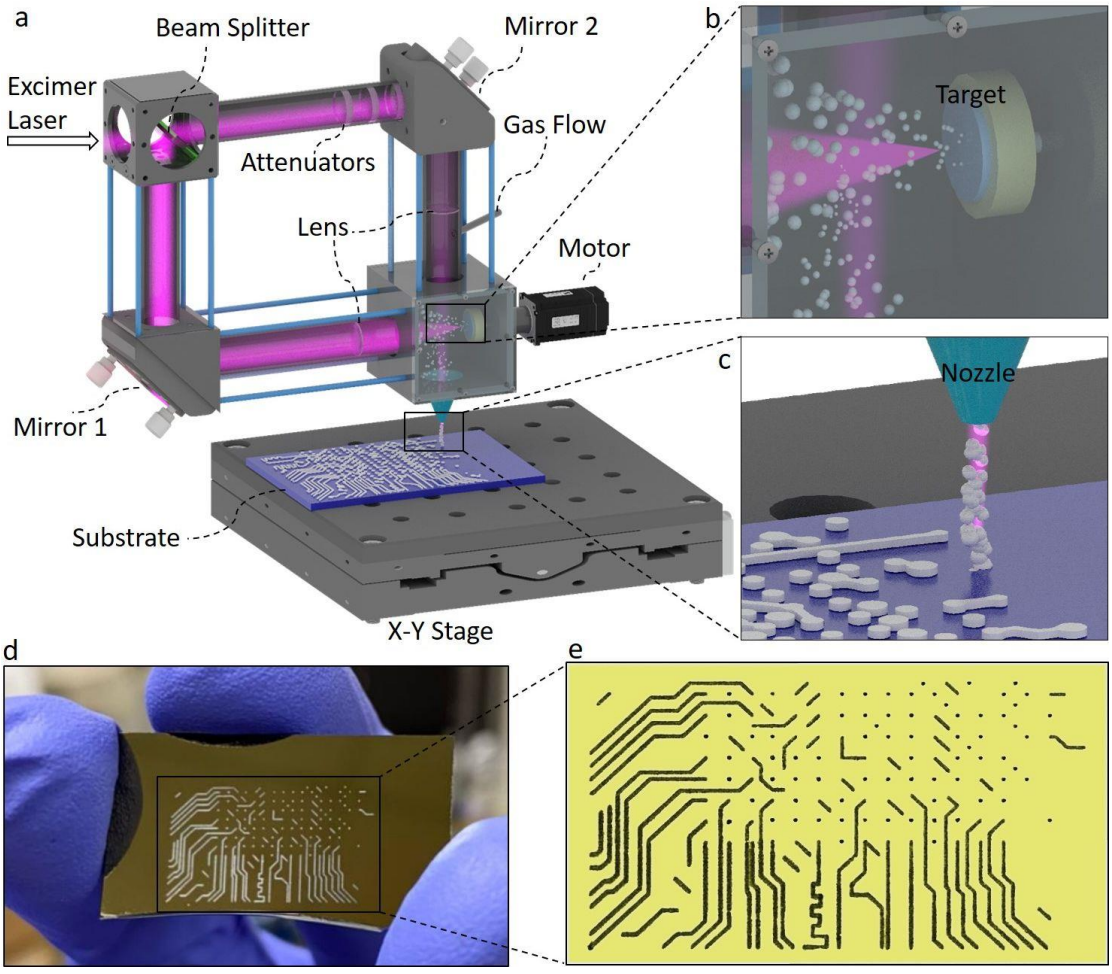

Figure 3.1. Schematic illustration of the ANM process used for printing various functional materials on the different substrates (a). Enlarged illustration of in-situ and on-demand generating of nanoparticles by pulsed laser ablation of the desired target materials in atmospheric pressure and temperature (b). Enlarged illustration of real-time laser sintering and crystallization of nanoparticles on the surface of the substrate (c). Optical image of printed circuit lines using the ANM process (d). Enlarged optical image of the printed circuit lines (e).

3.2.2Experimental Procedure

Solid targets (TiO_2, BTO, and ITO) with 99.9% purity were used for laser ablation and formation of nanoparticles. Different nozzles with hole diameters of ~100, 200, and 300 µm were used for the deposition. For the first set of experiments, TiO_2 was selected as the test target. Various laser fluences ranging from 1.9 to 2.3 J/cm^2 and 0.074 to 0.74 J/cm^2 were used for the ablation of the target and sintering/crystallization of produced pure amorphous nanoparticles, respectively.

Moreover, different repetition rates, including 5, 10, 15, and 20 Hz were used for the ablating and sintering processes. Various gas flow rates ranging from ~1 to 4.58 SLPM (standard liter per minute) were used to regulate the flow of nanoparticles out of the nozzle. A set of comprehensive experiments were performed to understand the effect of laser parameters (e.g., energy, frequency, gas flow rate, ablation and sintering time, and deposition overlap) on the printed materials.

3.3 Results and Discussion

3.3.1 Formation of Nanoparticle Building Blocks:

One of the key steps in this ANM process is the in-situ and on-demand formation of stoichiometric nanoparticles by condensation of laser-generated plasmas plume at room temperature and atmospheric pressure. These nanoparticles serve as the building blocks that can be sintered and crystallized in real-time during the printing process. To investigate the size and structures of these nanoparticles, we performed atomic imaging measurements. **Figure 3.2** shows the SEM and STEM images of the as-deposited TiO_2 nanoparticles (ablation energy (AE) = 2.3 J/cm^2, gas flow rate (GFR) = 2.8 SLPM, sintering/crystallization energy (S/C E) = blocked, repetition rate (RR) = 10 Hz). The as-deposited nanoparticles form an ensemble of a fluffy and porous deposition as shown by the SEM image in **Figure 3.2**a. These nanoparticles are mostly amorphous with a size distribution of about 3-7 nm in diameter, as shown by the STEM images in **Figure 2**b, c. The ability to generate such nanoparticle building blocks enables nanoscale precision in controlling the composition and thickness of the printed lines and allows simple integration and sintering into larger crystalline structures.

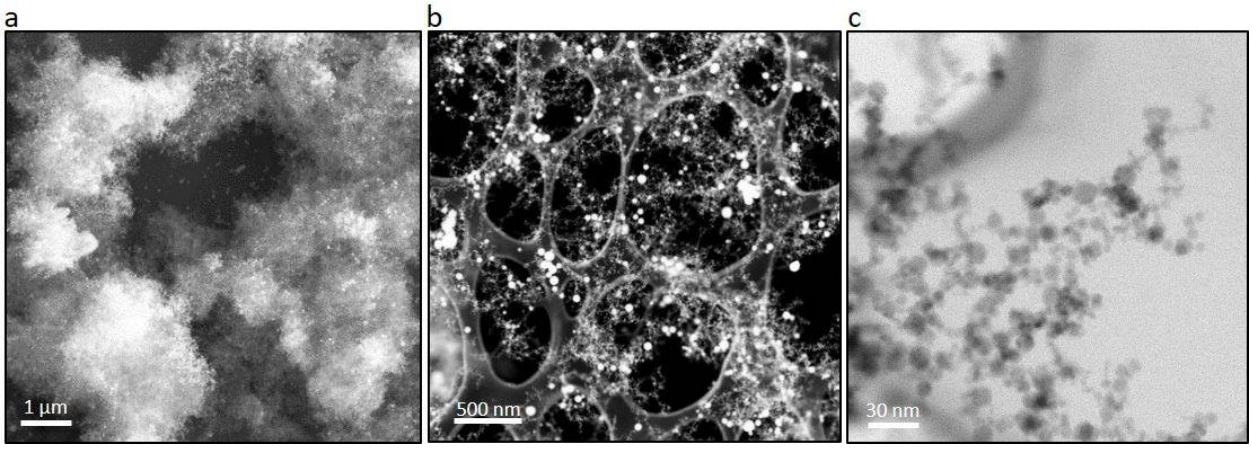

Figure 3.2. SEM image of ablated pure amorphous TiO_2 nanoparticles (a). STEM (b) and HAADF (c) images with different magnifications of ablated pure amorphous TiO_2 nanoparticles.

3.3.2 Sintering, Crystallization, and Printing Processes:

The interaction of the sintering/crystallization laser beam with in-situ generated TiO_2 nanoparticles at the surface of the substrate led to the formation of crystalline rutile TiO_2. To investigate the effect of the laser beam energy on the crystallization and sintering of amorphous TiO_2 nanoparticles, various samples were prepared and studied by Raman spectroscopy, as shown in **Figure 3.3**. Examining the Raman data from the in-situ generated pure amorphous nanoparticles (while sintering/crystallization beam was blocked) showed a broad spectrum with no explicit peaks suggesting that the generated TiO_2 nanoparticles are primarily amorphous (a-TiO_2). In addition, by increasing the crystallization energy (0.07 to 0.56 J/cm^2) while other parameters (AE = 2.3 J/cm^2, RR = 10 Hz, GFR = 2.8 SLPM, time = 30 s) kept constant, the in-situ generated a-TiO_2 nanoparticles started to sinter and crystallize on the surface of the Si/SiO_2 substrates. The explicit threshold of crystallization was observed by the appearance of several new Raman peaks when crystallization energy was around 0.217 J/cm^2 as shown in **Figure 3.3**. The Raman lines at 447 cm^{-1} and 612 cm^{-1} are assigned to the E_g, A_{1g} modes of the rutile TiO_2 phase, respectively.[116] The peak at 521 cm^{-1} is assigned to the silicon substrate Raman vibration

mode. The intensity of the E_g and A_{1g} modes increases by increasing the sintering/crystallization laser fluence from 0.217 J/cm^2 to 0.56 J/cm^2. The intensity of the Raman peaks is directly proportional to the crystallization quality and the thickness of the printed TiO_2.[117] It should be noted that increasing the sintering laser fluence beyond a certain threshold can re-ablate the printed layers from the substrate (~1 J/cm^2 for TiO_2). It is also worth mentioning that, depending on the substrate material, the energy of the sintering/crystallization beam may not be increased beyond the damage threshold of the substrate at the start of the deposition.

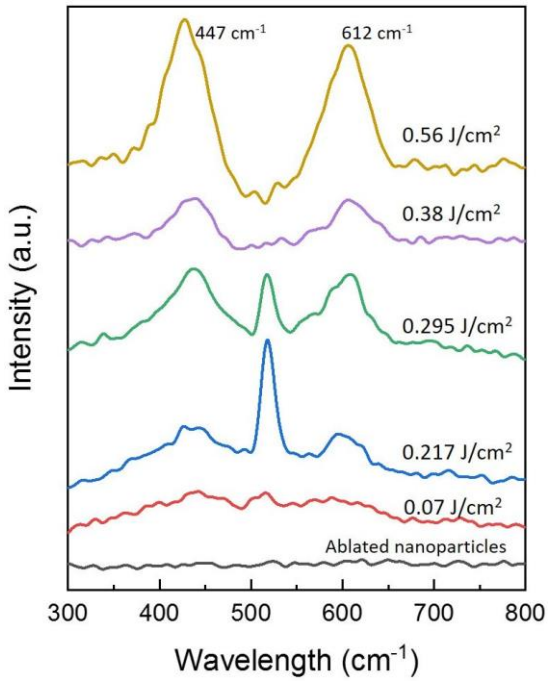

Figure 3.3. Representative Raman spectra of TiO_2 nanoparticles sintered at different crystallization energies, 0.07 up to 0.56 J/cm^2.

Morphologies of the printed TiO_2 layers on the Si/SiO_2 substrates at various process conditions were investigated by SEM, as shown in **Figure 3.4**. By turning off the sintering/crystallization beam, the printed nanoparticles were mainly agglomerates of amorphous TiO_2 nanoparticles (AE = 2.3 J/cm^2, GFR = 1.9 SLPM, RR = 10 Hz), as seen in **Figure 3.4**a and also confirmed by the STEM images in **Figure 3.2**. The SEM images shown in **Figure 3.4**b-h confirmed that during

laser sintering/crystallization, the nanoparticles fused together to form larger crystalline rutile TiO_2 structures. As depicted in **Figure 3.4b-d**, the feature size, as well as the thickness of the printed crystalline TiO_2 nanostructure, were continuously increased by increasing the time from 60 s to 270 s, while keeping all the other processing parameters constant (AE = 2.3 J/cm^2, GFR = 2.8 SLPM, S/C E = 0.3 J/cm^2, RR = 10 Hz). At longer deposition times, more TiO_2 nanoparticles were generated and delivered to the nozzle, resulting in thicker deposited layers. Other samples with different sintering/crystallization energies (0.295, 0.4, 0.67 J/cm^2), while keeping all the other processing parameters constant (AE = 2.3 J/cm^2, GFR = 2.8 SLPM, time = 60 s, RR = 10 Hz), were also investigated, and corresponding results are shown in **Figure 3.4**f-h. Accordingly, the density, thickness, and feature sizes of the printed TiO_2 layers were increased at higher sintering/crystallization energies, which was in agreement with the results observed from the Raman spectra shown in **Figure 3.3**.

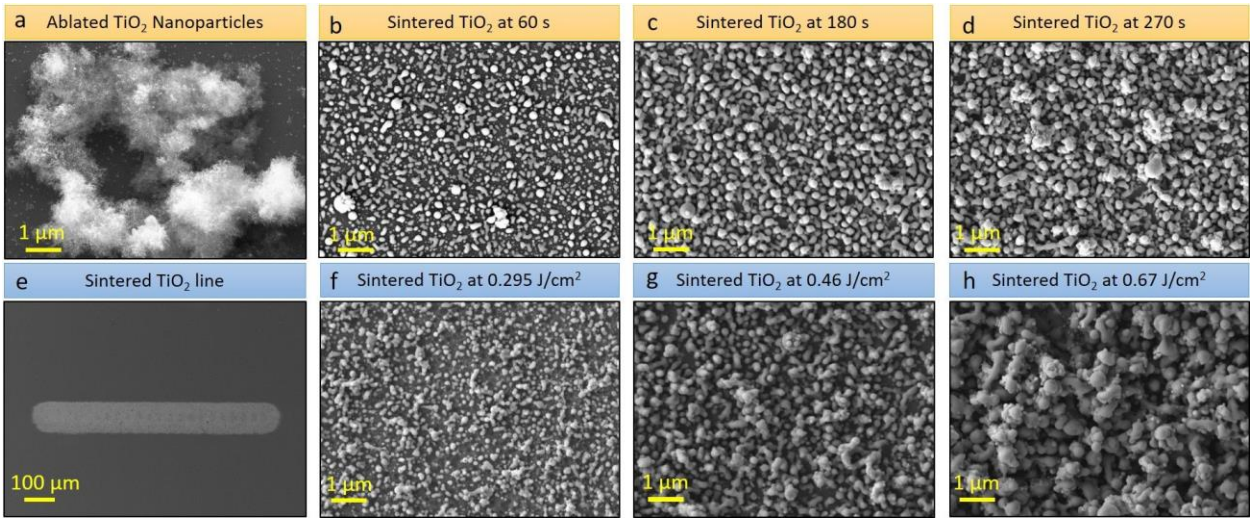

Figure 3.4. SEM image of as-produced amorphous TiO_2 ablated by laser (a), sintered TiO_2 at 60 s (b), 180 s (c) and 270 s (d) while crystallization energy and other parameters are kept constant. Line created by ANM method (ablation energy = 2.3 J/cm^2, gas flow rate = 2.8 SLPM, sintering/crystallization energy = 0.3 J/cm^2, repetition rate = 10 Hz, 90% overlap, X-Y delay = 5 s) with 100 µm diameter (e), sintered TiO_2 at 0.295 J/cm^2 (f), 0.4 J/cm^2 (g), 0.67 J/cm^2 (h) crystallization energy while time (60 s) and other parameters are kept constant.

3.3.3 Factors Affecting Printing Efficiency:

3.3.3.1 Influence of Gas Flow and Laser Repetition Rates

Understanding the role of process parameters is important in this ANM process as they govern the amount of nanoparticles that are generated, delivered, sintered to form crystalline printed layers and patterns. For a given ablation energy (2.3 J/cm^2), deposition time (60 s), and target material (TiO_2), the thickness variation of printed TiO_2 crystalline layers on the Si/SiO_2 substrate was analyzed, as a function of gas flow and laser repetition rates, as shown in **Figure 3.5**. The red and navy blue curves in **Figure 3.5**a show the thickness vs. gas flow rate while the repetition rate is 10 and 20 Hz, respectively. When GFR changed from 1 to 2.8 SLPM, as it is illustrated in **Figure 3.5**a, the thickness increased from ~175 to ~300 nm (in 10 Hz, red curve) and ~275 to ~450 nm (in 20 Hz, navy blue curve), suggesting that increased gas flow rate would result in increased deposition thicknesses. In **Figure 3.5**b (red curve), when the repetition rate changed from 5 Hz to 20 Hz, the thickness of printed TiO_2 crystalline layers increased from ~100 to ~275 nm. By changing the gas flow rate to 2.8 SLPM, **Figure 3.5**b (navy blue curve), while the repetition rate changed from 5 to 20 Hz, the thickness increased from ~125 to ~450nm, suggesting that increased repetition rate would result in increased deposition thicknesses. Moreover, the same measurements were performed while the crystallization energy changed to 0.46 J/cm^2, as shown in **Figure 3.5**c, d. A significant change in the thickness was observed compared to **Figure 3.5**a, b. It can be concluded that at lower sintering/crystallization laser energies, some of the amorphous nanoparticles coming out of the nozzle might rebound away from the surface before they have a chance to get sintered onto the printed lines. Higher sintering/crystallization laser energies tightly sinter the incoming nanoparticles on the substrate, and consequently, the thickness of the printed line increases. However, one should avoid

excessive energies beyond the re-ablation threshold, as mentioned above. These results show that both gas flow and repetition rates have a significant effect on the deposition thicknesses. Moreover, when the sintering/crystallization laser was blocked, due to the continuity of gas flow, most of the nanoparticles did not adhere well to the substrate and could be blown away from the surface.

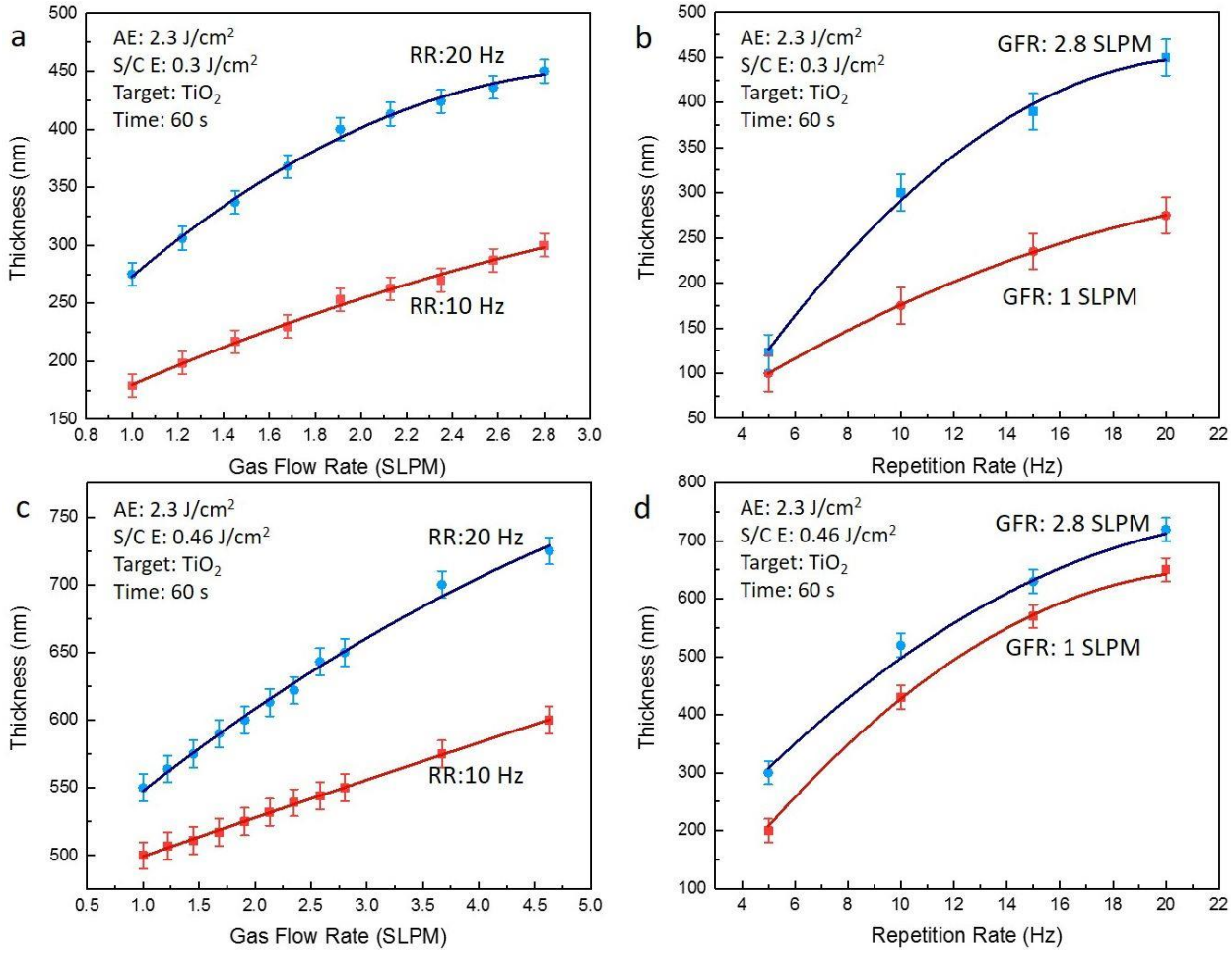

Figure 3.5. The thickness of ANM-printed dots as a function of gas flow rate for 0.3 J/cm^2 and 0.46 J/cm^2 in (a) and (c) sintering/crystallization energies. The thickness of ANM-printed dots as a function of repetition rate with 0.3 J/cm^2 and 0.46 J/cm^2 in (b) and (d) sintering/crystallization energies.

3.3.3.2 Influence of Deposition Time and Printing Overlap

Figure 3.6a shows the thickness of crystallized and sintered TiO_2 nanoparticles deposited on the SiO_2 substrate as a function of time. The thickness increases from ~250 to ~550 nm as the time increases from 10 s to 60 s (green curve, 1 SLPM). The changing trend of the thickness with time is the same for higher GFR, red and blue curves, implying that the thickness is also governed by time. **Figure 3.6**b, c shows the effect of deposition overlap (OL) on the thickness of deposited TiO_2 nanoparticles. Generally, increasing overlap via decreasing the stage velocity will result in the increment of the thickness. Three different overlaps numbers of 0, 50, and 75% were tested by the ANM system, while all other parameters were kept the same (AE = 2.3 J/cm^2, S/C E = 0.38 J/cm^2, GFR = 1.9 SLPM, RR = 10 Hz). The thickness measurement results showed an increment of thickness from ~200 nm (for 0% overlap) to ~600 nm (for 75% overlap).

According to the experimental results, we observed that larger diameter (>400 μm) nozzles would significantly disperse the nanoparticles, thus lowering the nanoparticles' confinement efficiency during the printing process. There was no evidence of noticeable deposition and sintering of TiO_2 on the substrate until the gas flow rate was set to more than 7.9 SLPM. However, the deposition/sintering area (circle with a diameter around ~ 250 μm) is still significantly smaller than the size of the nozzle, showing a low deposition rate at a larger diameter of the nozzle, while printed patterns with 100-200 μm diameter nozzles have the same size as the nozzle.

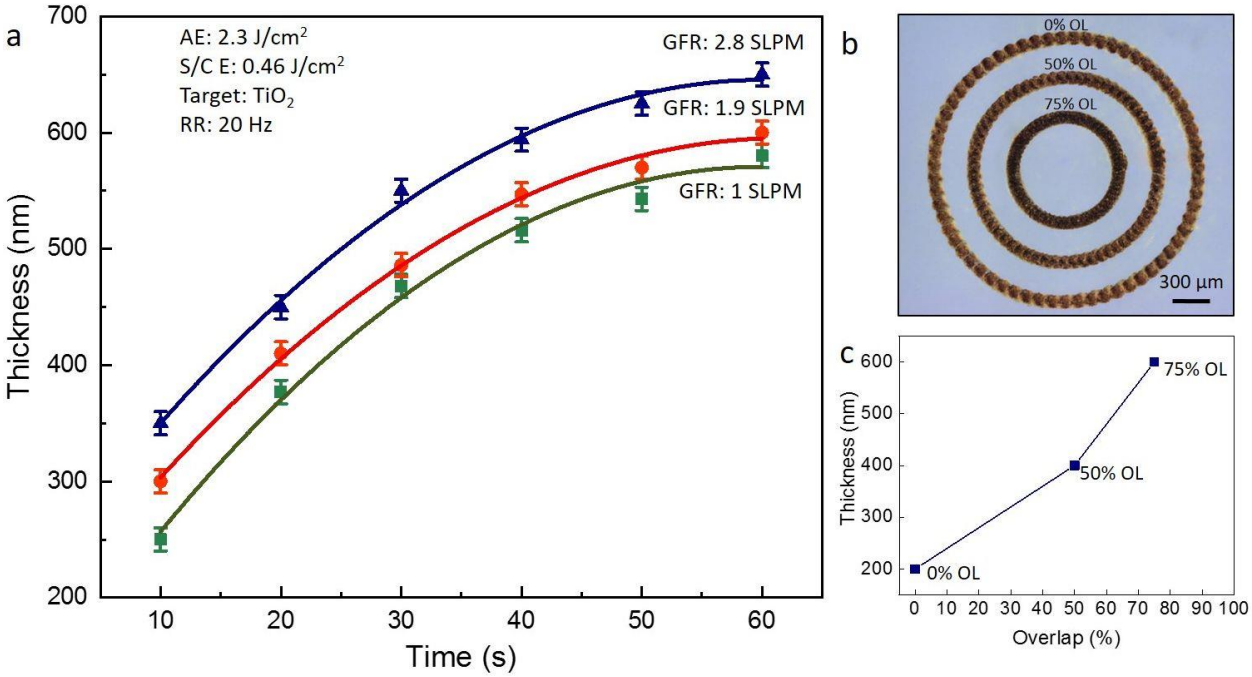

Figure 3.6. Sintered/crystallized TiO_2 thickness vs. sintering time at ablation energy = 2.3 J/cm^2, sintering/crystallization energy = 0.46 J/cm^2, repetition rate = 20 Hz, and different values of gas flow rate (a). Optical images of ANM-printed circles with different overlap ratio (b). Sintered/crystallized TiO_2 thickness vs. overlap (c).

3.3.2 Design and Printing of Various Patterns:

The remarkable ability of our novel ANM system enables the realization of any arbitrary patterns of sintered nanoparticles on the substrates. This can be simply realized by the programmable motion of the X-Y stage during the printing process. As shown in **Figure 3.7**a-e, we have demonstrated the printing of different shapes and patterns on Si/SiO_2 substrates. Experiment parameters are provided in **Table 1**. The nozzle diameter size was 100 µm for all experiments. The different line widths will be achieved by changing the diameter size of the nozzle. These experiments clearly showed the promising flexibility and adaptability of the ANM process for dry and vacuum-free printing of various materials and patterns.

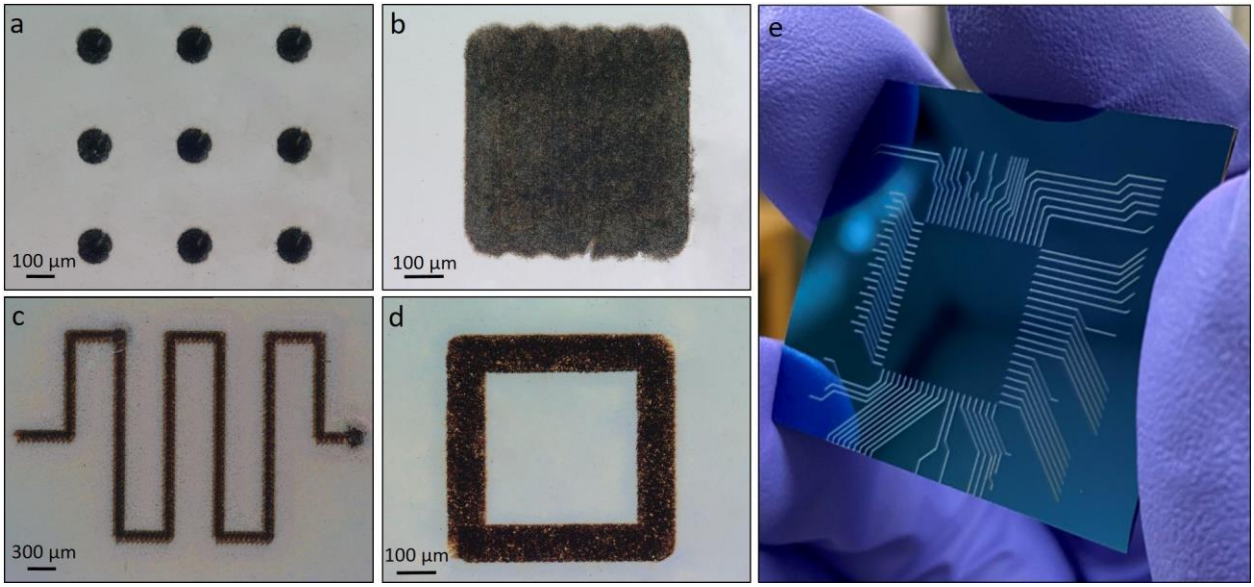

Figure 3.7. Optical images of printed TiO_2 (for a-d) and ITO (e) patterns on SiO_2 substrate by ANM method.

Table 3.1. Experimental parameters used for printing patterns of **Figure 3.7**.

Sample	AE (J/cm^2)	S/C E (J/cm^2)	Time (s)	GFR (SLPM)	RR (Hz)	OL (%)
a	2.3	0.46	60	2.8	20	0
b	2	0.54	5	1.9	10	90
c, d	1.7	0.3	5	2.8	10	90
e	2	0.25	5	2.8	10	90

3.3.3 Printing Compatibility with Different Type of Materials and Substrates:

To show the ANM's capability for printing other material systems, BTO and ITO patterns were also printed by this process. **Figures 3.8**a and d show the SEM images of ablated ITO (AE = 2.3 J/cm^2) and BTO (AE = 2.3 J/cm^2) nanoparticles, respectively. Based on the STEM images shown in **Figures 3.8**b, e, the size of the as-synthesized nanoparticles was in the range of 3-7 nm. Similarly, these nanoparticle building blocks could be laser sintered and crystallized to form desired patterns. **Figures 3.8**c and f show the sintered ITO (AE = 2.3 J/cm^2, S/C E = 0.23 J/cm^2,

GFR = 2.8 SLPM, RR = 10 Hz) and BTO (AE = 2.3 J/cm^2, S/C E = 0.15 J/cm^2, GFR = 2.8 SLPM, RR = 10 Hz) nanoparticles in the ANM method, respectively. As illustrated in **Figures 3.8**c and f, the approximate diameter of the sintered/crystallized ITO and BTO crystal structures became between ~ 50 to ~ 250 nm. Cross sectional SEM images of the printed ITO lines confirms the sintering of the ablated nanoparticles on SiO_2 substrate. The proposed ANM system allows for printing various multifunctional materials for the fabrication of functional devices for sensing and energy applications. For instance, BTO is an important functional material in the electronics industry because of its superior dielectric, ferroelectric, piezoelectric, pyroelectric, and electro-optical properties. Using these characteristics, BTO films may find applications in ion sensors, biosensors, and pH sensors. ITO is a key transparent conductive oxide, and its most prominent applications are in transparent electrodes in liquid-crystal displays, organic light-emitting diodes (LEDs), and touch-responsive screens, which can be found in smartphones and flat panel monitors. However, it is also used in applications such as low-emissivity windows, optoelectronic devices, solar cells, electrochromic windows, plasmonics, and lab-on-a-chip biosensing.

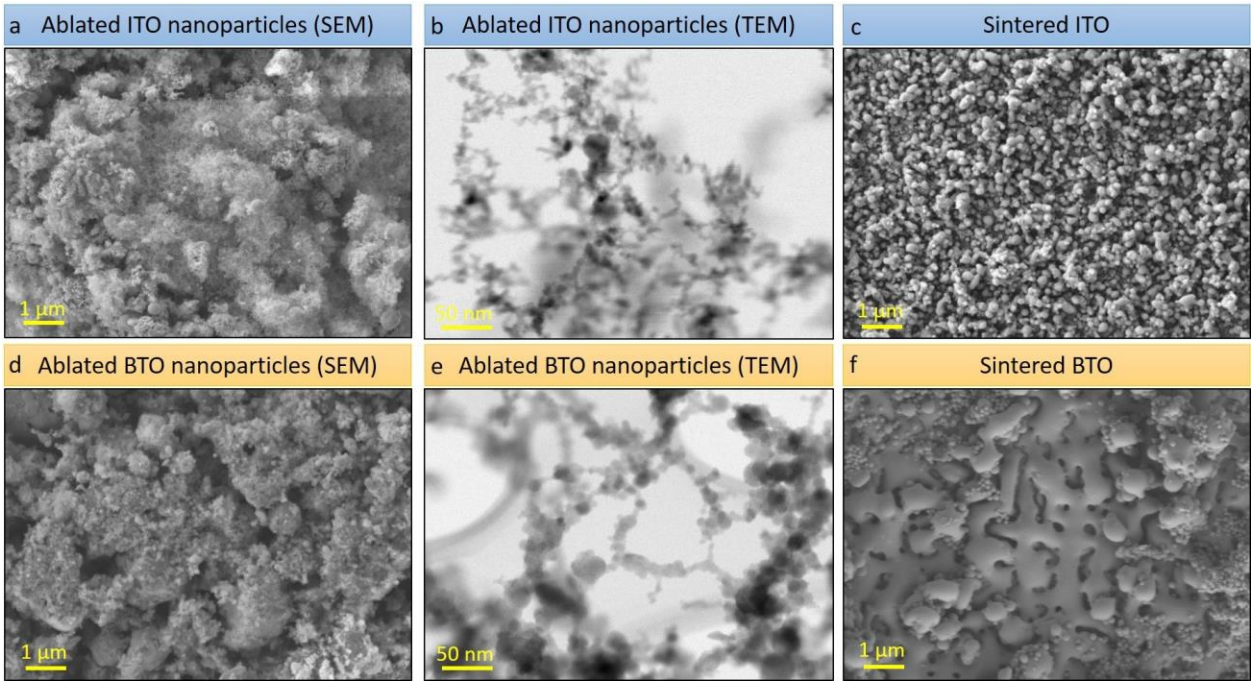

Figure 3.8. SEM images of ablated ITO (a) and BTO (d) nanoparticles. STEM images of ablated ITO (b) and BTO (e) nanoparticles. The SEM images of sintered and crystallized ITO (c) and BTO (f).

One of the fascinating advantages of this ANM process is it's suitability for printing on numerous substrates, including flexible substrates, paper, metals, glass, and ceramics. This is because of the dry printing and precision laser sintering nature of the ANM process. Hence, no liquid, polymer, or other binders are used in this system, and no post-processing steps are required after the printing process. This enables applications in a variety of fields, including biosensing, photonics, storage, and sensing.[118-120] **Figure 3.9** shows printed ITO patterns onto different substrates, including copper, alumina oxide (Al_2O_3), PDMS, and paper (AE = 2.3 J/cm^2, S/C E = 0.39 J/cm^2, GFR = 2.8 SLPM, RR = 10 Hz, used for all). This study will be further extended in future in order to understand the interaction of the sintered nanoparticles with various substrates and reveal their process-structure-property relationships.

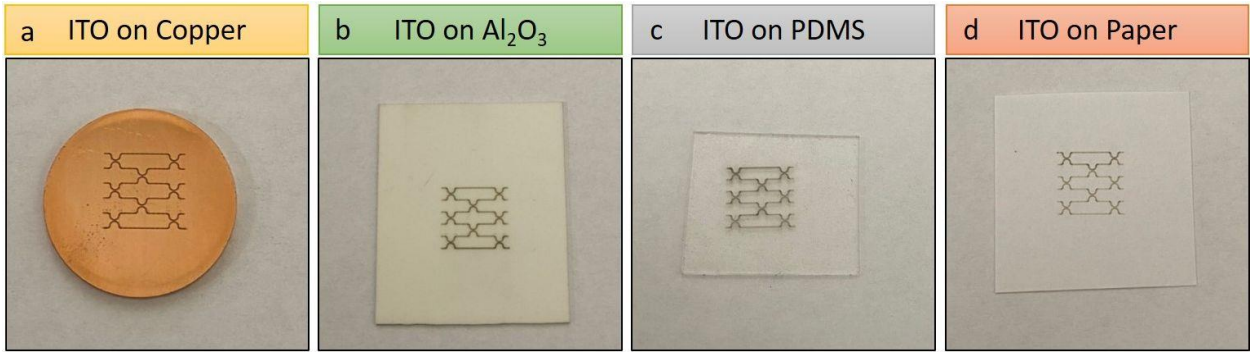

Figure 3.9. Photographic images of TiO_2 patterns (200 µm line width) printed on (a) copper, (b) Al_2O_3, (c) PDMS, and (d) paper.

ITO lines with variable resistance values were successfully printed by real-time resistance monitoring during the printing process, as demonstrated in **Figure 3.10**. The resistance that can be controlled over a large range from 1 kΩ to 10 MΩ is ideally suited for low cost flexible electronic circuits. The resistance of printed lines was altered by repeating the printed path (number of the printed layers) to increase the thickness, while the length and width of the printed resistor line remained unchanged. **Figure 3.10**a shows the schematic diagram of the printing process and real-time resistance measurement. First, two ITO contacts were fabricated on PET substrate. By connecting two contacts to a digital multimeter, the resistance of the line was obtained in real-time during the printing process. As shown in **Figures 3.10**b-e, the number of printed paths, or equivalently the thickness of the printed ITO line, affected its resistance. More number of printed paths resulted in lower resistances, while less number of printed paths resulted in higher resistances. In addition, the printing process parameters such as repetition rate and sintering/crystallization energy also affected the resistance versus the number of printed path relationships, as shown in **Figures 3.10**b-d.

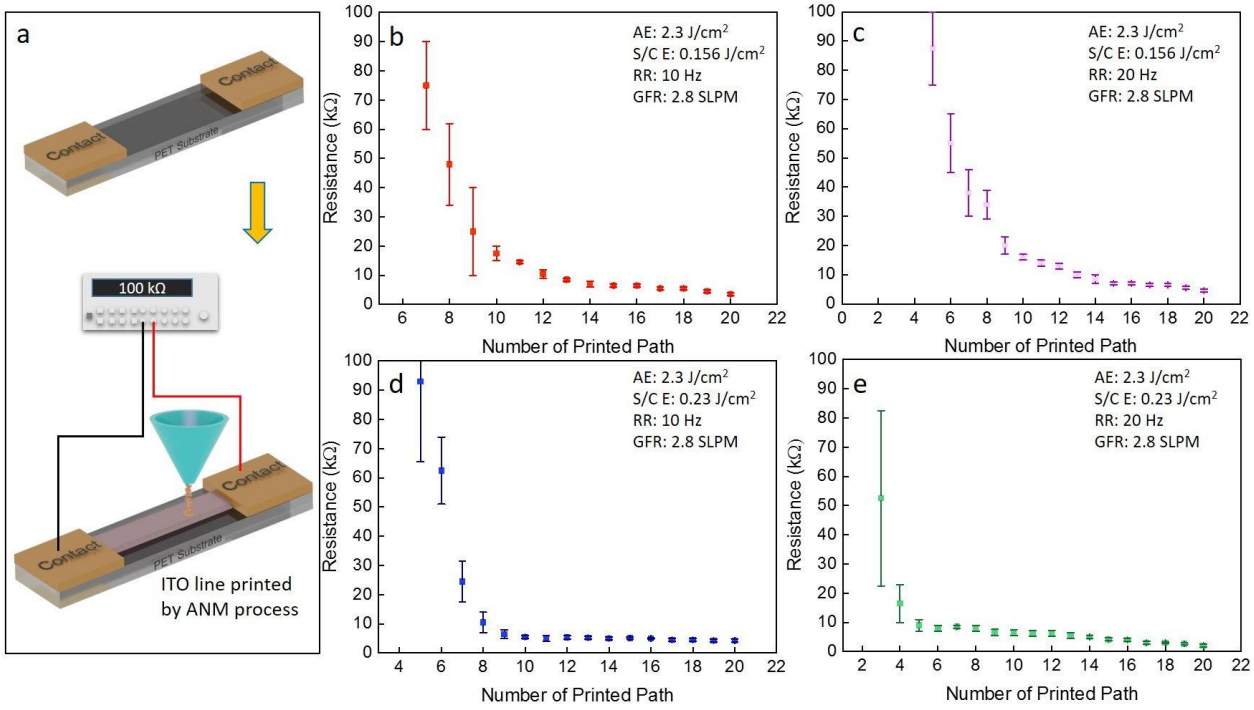

Figure 3.10. Real-time electrical resistivity measurement of 3 mm long lines while being printed by the ANM process as a function of the number of printed paths. Schematic illustration of deposited ITO line between two contact pads on a flexible PET substrate while the resistance is measured in real-time via a connected multimeter to pads (a). S/C E = 0.156 J/cm^2, RR = 10 Hz (b) S/C E = 0.156 J/cm^2, RR = 20 Hz (c) S/C E = 0.23 J/cm^2, RR= 10 Hz e) S/C E = 0.23 J/cm^2, RR = 20 Hz (d).

3.4 Conclusion

In summary, this paper reports the first demonstration of a novel laser-based additive nanomanufacturing method that enables the printing of various functional materials on different substrates. This new method allows the in-situ and on-demand formation of various nanoparticle building blocks in atmospheric pressure and at room temperature. These nanoparticle building blocks can be directed toward the substrate through a nozzle forming a stream of nanoparticles that can be laser sintered/crystallized on various substrates in real-time. A set of comprehensive experimental studies were performed to decipher the effects of process parameters (gas flow rate, time, overlap, sintering energy, frequency repetition rate, thickness) of this ANM process on the printed materials and structures. Scanning electron microscopy and transmission electron

microscopy were used for grain size confirmation. This method inherits the merits of producing nanoparticles that are dry, solution-free, and intrinsically pure that can be simultaneously laser sintered and crystallized to form contamination-free multifunctional materials prints on various rigid and flexible platforms such as PDMS, Si/SiO_2, paper, and ceramics. This method enables the future additive nanomanufacturing of hybrid multifunctional material and structures and print devices with complex functionalities.

CHAPTER 04

Dry Printing and Additive Nanomanufacturing of Flexible Hybrid Electronics and Sensors

4.1 Introduction

The research and development on flexible hybrid electronics (FHEs) has been rising rapidly due to its wide range of applications in healthcare, consumer products, automotive, aerospace, and energy industries.[121-127] The conventional lithography-based processes for manufacturing electronics are often complicated, time and energy-consuming, relatively expensive, and produce a large amount of waste materials (washing–cleaning–disposal requirements).[128] Thus, much effort has been put toward inventing new techniques for direct printing and additive manufacturing of electronics on desired flexible and rigid substrates,[106, 107, 129-134] such as polyimide and polyethylene terephthalate (PET).[135-137] Different fabrication strategies have been proposed for additive nanomanufacturing of electronics.[138-143] The most common direct-write technologies in the field of printed electronics are inkjet printing (IJP) and aerosol jet printing (AJP).[126, 144-148] These technologies allow the precise deposition of liquids containing functional materials. Recently, Patil et al. printed silver (Ag) nanowires (resistance < 50 Ω sq^{-1}) on flexible substrates via inkjet printing.[149] Gilshtein et al. demonstrated inkjet-printed indium tin oxide (ITO) patterns with a resistivity of 3.1×10^{-3} Ω cm on soda-lime glass.[150] Chen et al. showed aerosol jet printing of Ag with a sheet resistance of 1.13×10^{-2} Ω/m^2 on cellulose fiber paper substrate.[147] However, the current ink formulations used in IJP and AJP processes make device fabrication more complicated because they require toxic solvents and additives that limit the substrate's compatibility and hinder the device's performance.[151, 152] Also, nozzle clogging in

IJP is a common and extremely complex phenomenon.[153] Furthermore, to guarantee a high conductivity of the printed structures, aerosol printing usually requires a high sintering temperature (e.g., ~280 °C) and a long sintering time (e.g., 12h on a glass substrate). This limits the AJP to only a few types of substrates.[147] As a result, a new direct printing and patterning method is needed to overcome the challenges. Moreover, the new printing and patterning methods also need to be capable of printing structures with good reliability under repeated mechanical bending and unbending processes.

Motivated by these challenges, here, we demonstrated a novel additive nanomanufacturing technique recently developed in our lab for manufacturing FHEs and sensors by printing conductive Ag and ITO on different flexible platforms such as polyimide and PET substrates. Conductive Ag is typically used to print electronic tracks, electrodes, and antennas.[154, 155] Transparent conductors such as ITO are utilized in the printing of components such as flexible strain sensors, solar cells, and organic light-emitting diodes (OLEDs).[156-159] The main principle of our ANM printer is the in-situ formation of pure and dry nanoparticles produced by condensation of laser-plasma plume in atmospheric Ar pressure, which is then guided through a nozzle onto a substrate that is sintered in real-time, forming the desired patterns. The mechanical reliability of ANM-printed samples has been shown by investigating the resistance change of the samples via bending and cycling tests. FHEs and sensors such as near-field communication (NFC) tag antenna, ITO-based strain sensor and lighting circuits were fabricated on polyimide and PET substrates to demonstrate their performances in this printing approach. This novel ANM and device manufacturing method is a promising technology for future manufacturing of the FHEs and sensors directly from dry and pure nanoparticles generated and sintered in on-demand and in real-time.

4.2 Experimental Setup

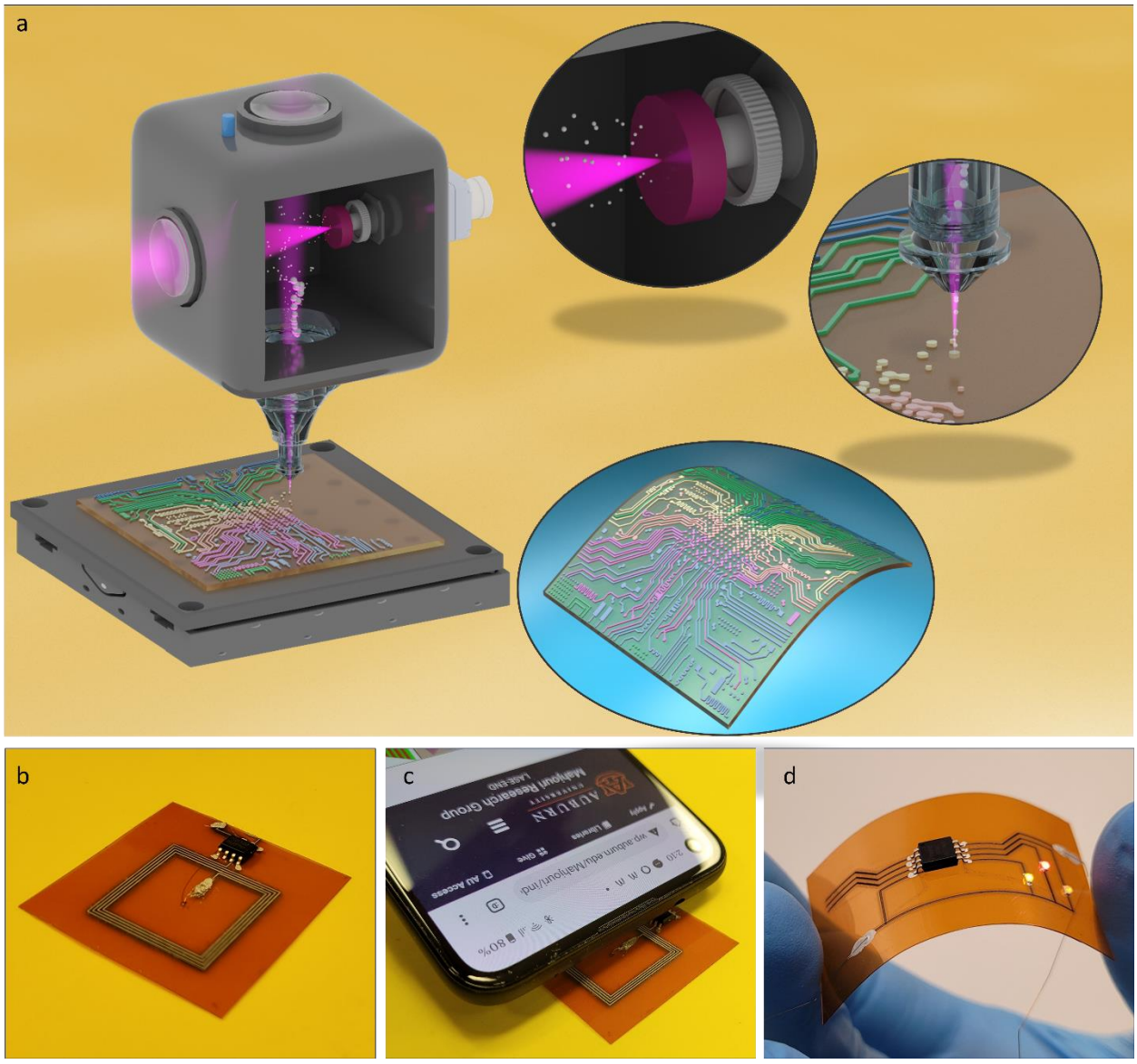

Figure 4.1. Schematic illustration of ANM process for dry printing Ag and ITO on flexible substrates (a). A 2 × 2 cm^2 printed Ag NFC tag antenna (four loops with a total length of ~32 cm and ~1.38 Ω cm resistance) connected to a self-power M24LR04E IC enabling communication with a phone device (b, c). Printed FHEs circuit on the polyimide substrate (d).

Figure 4.1 shows the schematic illustration of the ANM printer consisting of a microchamber, a rotating target, a nozzle, and a gas flow feeder system. A Coherent COMPex excimer laser (KrF, pulse duration 25 ns) beam was divided into two paths; one for laser ablation (LA) and the other

for laser sintering (LS) processes in the ANM system. These beams were focused onto the surface of targets and substrates via UV convex lenses. Depending on the type of the materials and substrates, LA and LS beams' energy were adjusted to achieve the formation of desired nanoparticles. Focused LA beam hits the rotating targets, which will result in the formation of plasma plume that interacts with background Ar gas resulting in condensations and formation of nanoparticles on-demand. These nanoparticles are then directed toward the substrate through a nozzle with different diameters ranging from 100 μm to 300 μm using a carrier gas. The LS beam with suitable energy sinters and crystallizes the arrived nanoparticles onto the substrate's surface in real-time. As more nanoparticles arrive, the deposition increases and forms a continuous film.

The substrates were placed on an XY positioning stage and moved according to the preprogrammed path. The distance between the apex of the nozzle and the substrate was kept constant at ~ 0.5 mm. Commercially available Ag and ITO targets with 99.99% purity were used for the ablation and formation of nanoparticles. The diameter of the nozzles used in ANM printer determined the feature size of the printed lines. The thickness of the printed lines was controlled by printing speed as well as the number of layer-by-layer printed paths.

It should be noted that since we used only an excimer laser for the ablation and sintering process, the repetition rate was always the same for ablation and sintering processes. Typically, lasers with shorter wavelengths (higher photon energy) and shorter pulse widths (high peak power) are suitable for the efficient ablation of a wide range of solid targets. Also, depending on the type of materials and substrates involved in the process, various sintering energies should be employed. Moreover, the shallow absorption depth of UV laser used here allowed us to slightly sinter the generated nanoparticles without damaging the underlying substrates.

Figure 4.1b shows an example of a 2 × 2 cm^2 printed Ag NFC tag antenna (four loops with a total length of ~32 cm and ~1.38 Ω cm resistance) printed on a polyimide substrate. The mounted M24LR04E IC was programmed to launch our group's website. As shown in **Figure 4.1**c, the group website pops up on display by holding the cellphone in the proximity (~ 1 cm) of the printed NFC tag. **Figure 4.1**d demonstrates the printed FHEs circuit on the polyimide substrate via ANM process.

4.3 Results and Discussion

4.3.1 Nanoparticles Generation and Sintering

To confirm the nanoparticle formation and analyze their size distribution, we performed scanning electron microscopy (SEM) and scanning transmission electron microscopy (STEM) measurements on the as-generated nanoparticles. While the LS beam was blocked, we collected laser-ablated Ag and ITO nanoparticles (ablation energy (AE) = 2 J cm^{-2}, gas flow rate (GFR) = 2.8 SLPM, sintering/crystallization energy (S/CE) = blocked, repetition rate (RR) = 10 Hz). The SEM images of the unsintered and laser-sintered nanoparticles are shown in **Figure 4.2**a and d. **Figure 4.2**b and e shows the bright-field (BF) STEM images of the captured Ag and ITO nanoparticle, which were directly deposited onto the TEM grids for measurements. According to the STEM images, the size of the generated nanoparticles was in the range of 3-10 nm diameters. The unsintered nanoparticles form a fluffy structure that is loosely attached to the substrate. When these nanoparticles were laser sintered during the process, they fused together to form a solid line. **Figure 4.2**c and f shows the sintered Ag and ITO nanoparticles. The sintering energy was 0.08 J cm^{-2} and 0.13 J cm^{-2} for Ag and ITO, respectively. **Figure 4.3** shows a cross-sectional SEM image of the printed Ag line confirming the sintering of the ablated nanoparticles on SiO_2 substrate.

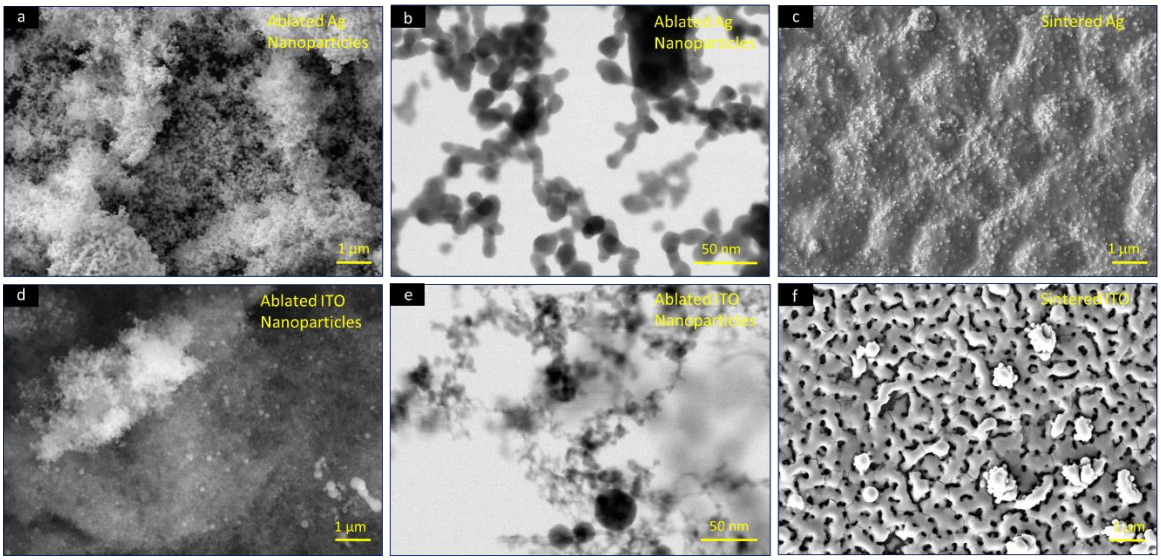

Figure 4.2. SEM images of laser-ablated Ag and ITO nanoparticles, respectively (a, d). BF-STEM images of laser-ablated Ag and ITO nanoparticles, respectively (b, e). SEM images of laser-sintered Ag (c) and ITO (f).

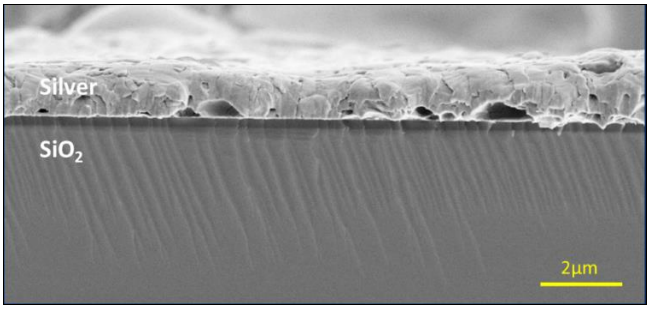

Figure 4.3. Cross-sectional image of printed and sintered silver nanoparticles on SiO_2 substrate via ANM process.

SEM images in **Figure 4.4** show the morphological and electrical resistance evolution of the sintered Ag nanoparticles at different sintering laser energies. By increasing the crystallization energy while other parameters (AE = 2 J cm^{-2}, RR = 40 Hz, GFR = 2.8 SLPM, laser beam overlap= 93%, deposition time in each point=20 ms, number if printed path= 6, and nozzle diameter size= 300 µm) are kept constant, the nanoparticles start to fuse together. The highest porosity was seen at the lower sintering energy (~0.03 J cm^{-2}), and the lowest porosity was achieved at the higher laser sintering energy (~0.11 J cm^{-2}), as shown in **Figures 4.4**a and i, respectively. It should be noted that the laser energies below the abovementioned lowest

threshold did not impact the particles, and energies above the higher threshold resulted in reablation of the deposited particles. Moreover, the electrical resistivity of the printed lines decreased as the sintering laser energy increased (shown in the upper right corner of the figures). As it has shown in **Figure 4.4**a-i, 40 Ω cm and 7 Ω cm resistance were measured for lowest and highest sintering laser energies, respectively.

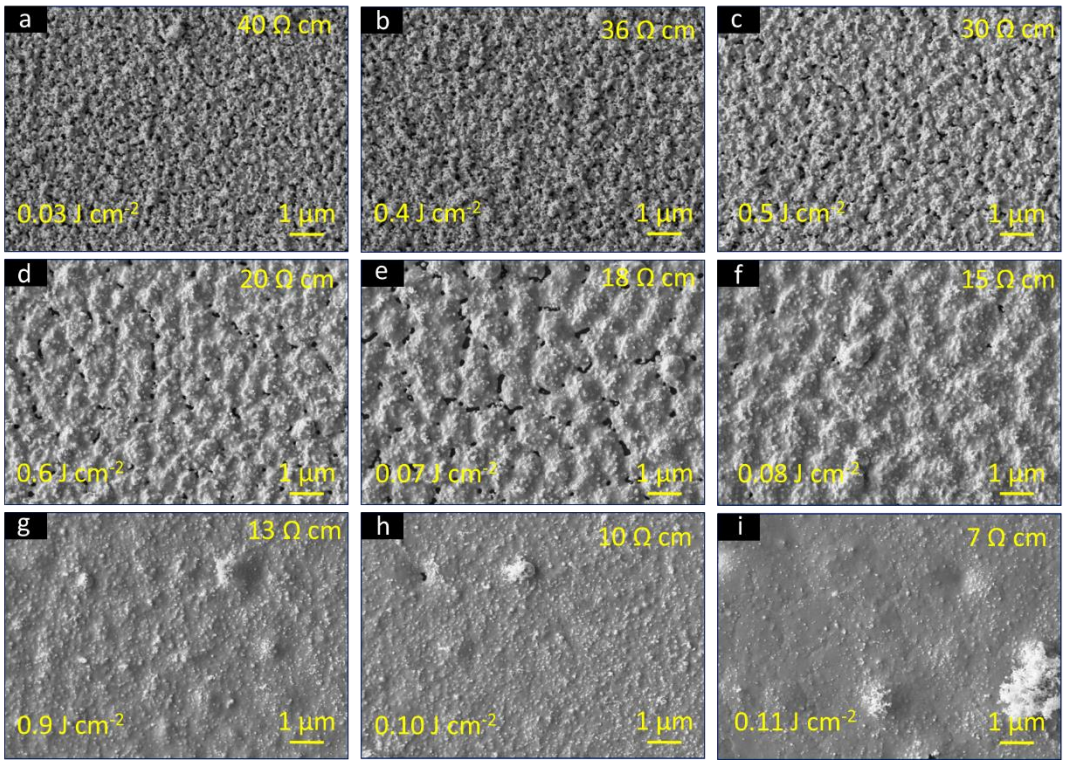

Figure 4.4. SEM images of morphological evolution of the printed Ag lines with different sintering laser energies as indicated on the bottom left corner of each figure (a-i). By increasing the sintering/crystallization energies, the porosity and resistance (shown upper right corner of each figure) of the printed lines decreased accordingly.

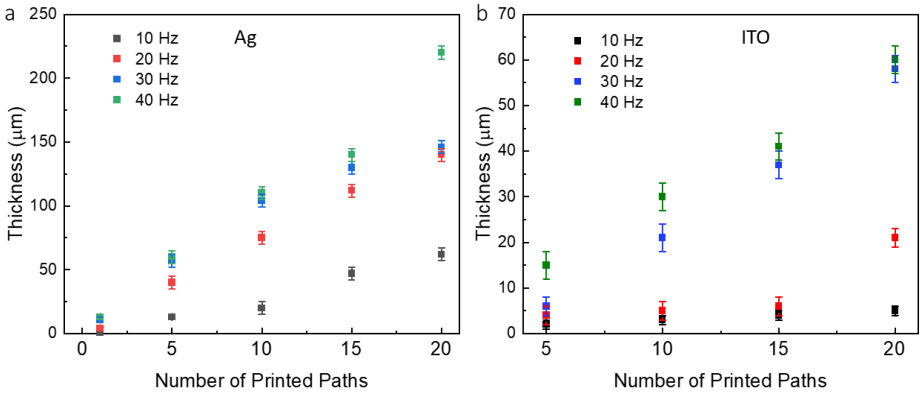

Figure 4.5. The thickness of sintered Ag (a) and ITO (b) as a function of the number of the printed paths at 4 different repetition rates 10 Hz, 20 Hz, 30 Hz, and 40 Hz.

4.3.2 Factors Determining Electrical Properties of the ANM-Printed Lines

For the given process parameters (AE = 2 J cm^{-2}, S/CE= 0.09 (Ag) and 0.39 (ITO) J cm^{-2}, GFR = 2.8 SLPM, laser beam overlap= 93%, deposition time in each point= 20 ms and nozzle diameter size= 300 µm), the thickness variation of the printed Ag and ITO lines on the polyimide substrates was analyzed at four different laser repetition rates (i.e., 10 Hz, 20 Hz, 30 Hz, and 40 Hz), as shown in **Figure 4.5**. In the case of Ag (**Figure 4.5**a), at 10 Hz repetition rate, the thickness increased from ~1 µm to ~60 µm when the number of printed paths increased from 1 to 20. Also, while the repetition rate increased (e.g. 40 Hz), the thickness of printed Ag layers increased in each path compared to a lower repetition rate (e.g. 10 Hz). This could be attributed to the fact that the ablation rate and hence the number of in-situ generated and sintered nanoparticles increase at higher repetition rates. The influence of gas flow rate (GFR), repetition rate (RR), and laser sintering/crystallization energy (S/CE) on thickness and resistance of printed TiO_2 and ITO is comprehensively discussed in our previous work,[122] where we showed that the thickness of the ANM-printed TiO_2 is directly proportional to the number of printed paths and repetition rate.

Here, we have also performed a systematic study to investigate the influence of repetition rates and the number of printed paths on the printing speed and electrical conductivity of printed Ag lines on polyimide substrates. Similar information for ITO lines are reported in our previous study.[122] **Figure 4.6**a-d represents the real-time resistance monitoring of 1 cm long printed Ag lines on polyimide substrates at different repetition rates ranging from 10 Hz to 40 Hz while other parameters were kept constant (AE = 2 J cm^{-2}, S/CE= 0.1 J cm^{-2}, GFR = 2.8 SLPM, laser beam overlap= 93%, deposition time in each point= 20 ms, and nozzle diameter size= 300 µm). As shown in **Figure 4.6**, the electrical resistance of the printed lines decreased by increasing the number of printed paths and hence increasing the thickness of the printed lines, while the length and width of the printed resistor line remained unchanged. Also, increasing the repetition rate from 10 Hz to 40 Hz increased the line thickness and hence reduced the resistance down to ~16 Ω cm with just one path of printing. It can be seen from **Figure 4.6**a and d that using 40 Hz repetition rate and one-time printing path, the resistance reaches ~ 16 Ω cm, while for achieving the same resistance at 10 Hz repetition rate, the number of printed paths should be around 30 times. The Ag resistance could be tuned from 1 Ω cm to ~200 KΩ cm by adjusting the abovementioned process parameters. As a result, the ANM-printed lines and materials could be potentially used to realize fully printed FHEs. The print resolution of the ANM was tested down to 100 µm using common commercial printing nozzles. Printing thinner lines (e.g., < 100 µm) may be possible using smaller diameter nozzles since our ANM technique uses nanoparticles with an average size of 3-10 nm.

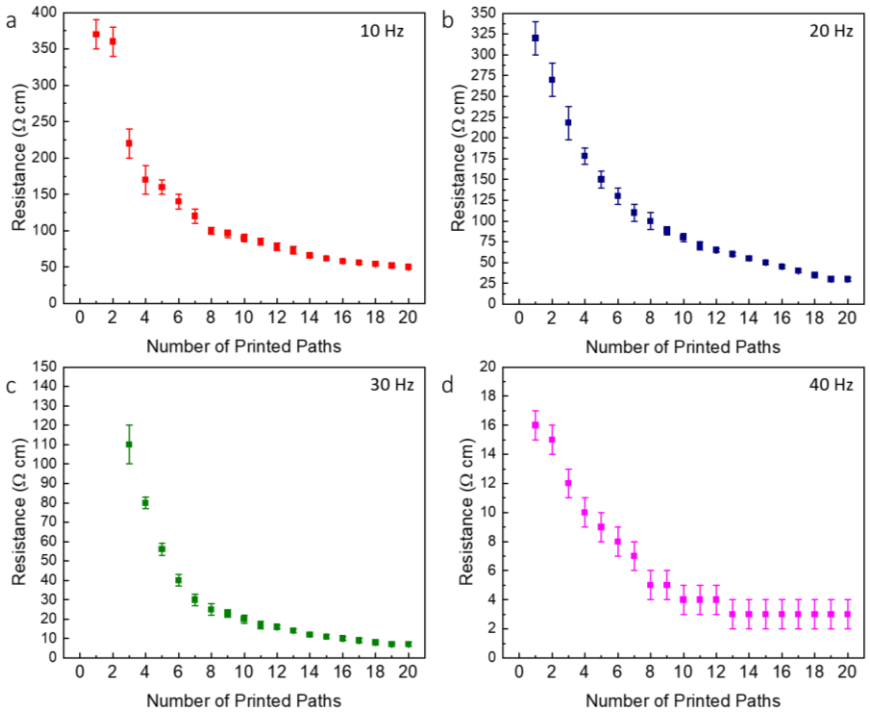

Figure 4.6. Resistance of ANM-printed Ag lines as a function of the number of printed paths for four different repetition rates, including 10 Hz (a), 20 Hz (b), 30 Hz (c), and 40 Hz (d).

4.3.3 Reliability Testing of the ANM-Printed Ag Lines on Flexible Substrates

To test the reliability of the printed lines, we printed a set of Ag lines with the experimental parameters shown in **Table 1**. The reliability of these ANM-printed lines was investigated under the static and cyclic bending studies. Consequently, mechanical strain such as bending, cycling, and stretching may change the electrical performance of the printed lines. Thus, we performed in-situ measurements to measure the changes in the resistance of the printed lines under different bending radii and compressive stresses. **Figure 4.7**a shows the schematic of the bending/cycling test setup. For instance, we tested different bending radii ranging from 77 mm to 16 mm equivalent to 0.08% to 0.5% strain. **Figure 4.7**b-d shows the variations in the electrical resistance of printed Ag lines as a function of different strains at three different numbers of

cycles. The resistance change ($\Delta R/R_0$) and the strain on the device were calculated using the equations:

$$\frac{\Delta R}{R_0}\ (\%) = \frac{R_s - R_0}{R_0} \times 100 \quad (1)$$

$$Strain\ (\%) = \frac{t_{substrate}}{2R_{bend}} \times 100 \quad (2)$$

where R_0, R_s, $t_{substrate}$, R_{bend} are initial resistance, under-stress resistance, substrate thickness, and bending radius, respectively.[160, 161] In the case of Ag, the resistance increased as it was bent for just one cycle, but the values of the resistance did not change drastically from the initial resistance values (e.g., R_0 = 10.4 Ω cm to R_s = 11.5 Ω cm at the maximum strain of 0.5%). As it is shown in **Figure 4.7**b-d, the resistance increased more at higher bending strains (lower bending radius). As shown in **Figure 4.7**b, the largest change in resistance was for conditions where the initial resistance was 22.4 Ω cm, and the final resistance was 25.5 Ω cm at 0.5% strain. Also, the smallest change in the resistance seen in **Figure 4.7**b was for resistance changing from an initial resistance value of 10.8 Ω cm to a final resistance of 10.9 Ω cm at 0.08% strain.

The results from the 50 cycling tests are demonstrated in **Figure 4.7**c. According to the results, the resistance increased only slightly. The mean average of the overall change in resistance was 1.97 Ω cm. Thus, these Ag samples could tolerate a large strain with a slight increase in their electrical resistance. The results for 1000 cycles for different strains are presented in **Figure 4.7**d. Also, we observed that during the first 50,000 cycles, the resistance increased for a 10 Ω cm Ag line up to ~20 Ω cm (i.e., 100%), then the resistance started to increase continuously to more than ~38 Ω cm at 1,000,000 cycles. Relaxation time for this sample was around ~1 hour, and the final measured resistance was ~27 Ω cm. Low resistance deviation in bending radius beyond 40 mm (0.19% strain) and after numerous folding/unfolding cycles demonstrates the

reliability of ANM printing process for manufacturing flexible electronics and sensors. Similar to the IJP and ASJ printing, the increase in electrical resistance could be attributed to the formation of cracks in deposited materials. When the substrate is stretched, the high flexibility of the substrate and the less stretchable Ag causes crack formation, which ultimately causes the change of the resistance. Higher bending and stress accelerated the dislocation and crack formation in the sintered materials.

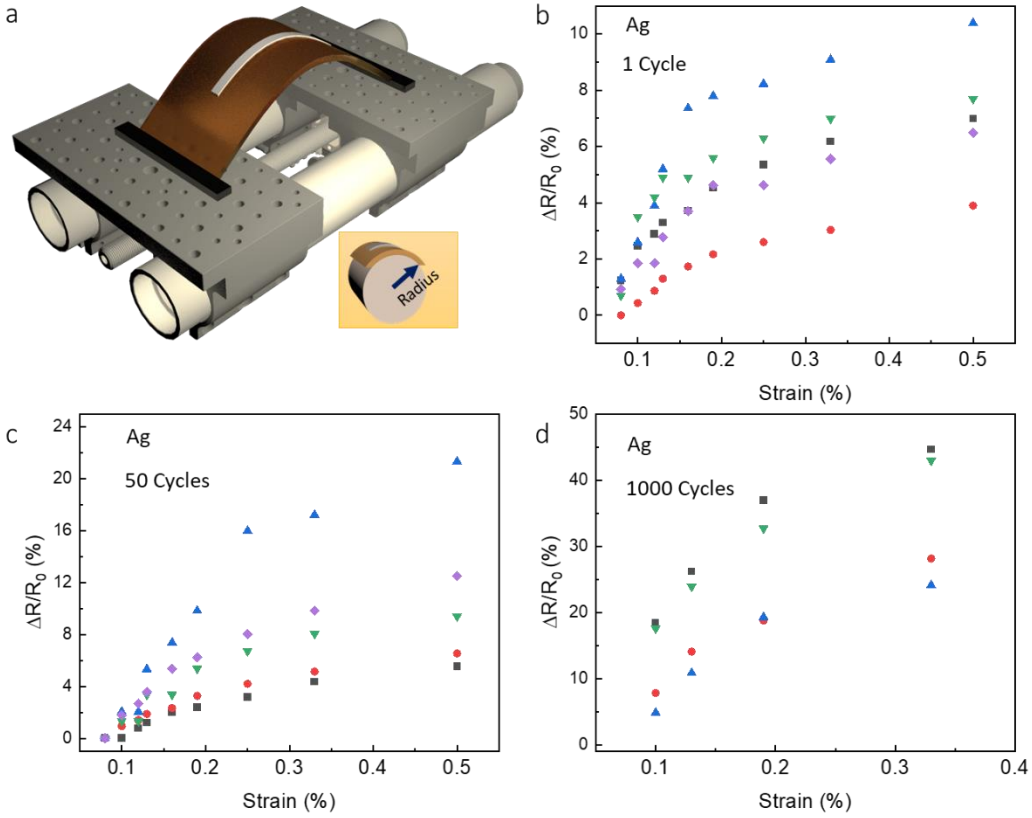

Figure 4.7. Schematic illustration of bending/cycling testing setup (a). Bending results of the ANM-printed Ag line for 1 cycle (b) and 50 cycles (c). (Initial resistance: red, 10.8 Ω cm; purple, 13.6 Ω cm; black, 22.5 Ω cm; green, 25 Ω cm; Blue, 22.4 Ω cm). Bending results of the ANM-printed Ag lines after 1000 cycles (d); (Initial resistance: red, 6.4 Ω cm; black, 20 Ω cm; green, 6.5 Ω cm; Blue, 8.3 Ω cm).

Table 4.1- Experimental parameters used for printing samples of **Figure 4.7**.

Figure 4.7	AE [J cm^{-2}]	S/CE [J cm^{-2}]	GFR [SLPM]	RR [Hz]	Number of Printed Path	Deposition Time in Each Point [ms]	Nozzle Diameter Size [µm]
a	2	0.08	2.8	10	30 to 40	20	300
b	2	0.08	2.8	10	30 to 40	20	300
c	2	0.08	2.8	40	1 to 7	20	300

4.4 Functionality Demonstration

4.4.1 Printing Strain and Temperature Sensors

ITO is a transparent conducting layer that has been used in numerous applications. Although ITO has a low sheet resistance and excellent transparency, printed ITO lines on flexible substrates are usually micro/nanocrystalline structures with grain boundaries and pores, which might form micro/nano cracks under tensile strains. These changes in properties can be exploited for strain sensors, touchscreens, and motion detectors applications.[157]

We used a servohydraulic fatigue testing machine for displacement-controlled stretching tests, as shown in **Figure 4.8**a. ITO lines were printed onto the PET substrates (55 mm×5 mm×0.175 mm) using process parameters reported previously.[122] Stretching tests for the printed ITO lines on PET were performed for different stretch levels. The amount of stretch was controlled with a precision of 0.18% to 0.9% displacement. All of the stretched samples were subjected to 100 cycles. For instance, **Figure 4.8**b shows the change in the resistance when subjected to 0.18% to 0.9% displacement for a printed ITO sample with initial resistance of ~1.18 KΩ cm. For the case of 0.18% displacement, the resistance change was less than 5%, while for 0.36% displacement, it is about 16%. For the case of 0.54% to 0.72% displacement, the resistance change was around ~50%. Applying 0.9% displacement resulted in a gradual resistance change of up to ~400%.

Above 0.9% displacement, permanent substrate plastic deformation was observed, resulting in resistance overload. The cycling frequency was kept at 1 Hz for all the samples.

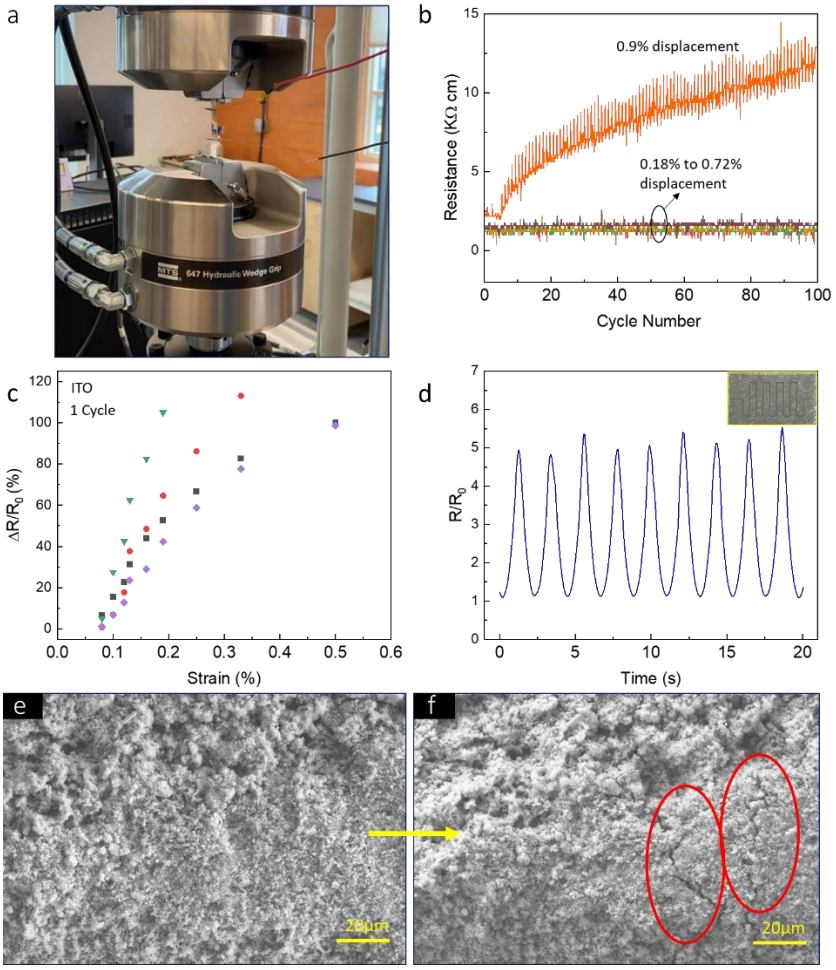

Figure 4.8. Digital image of fatigue setup used for stretching tests (a). Change of resistances in ANM-printed ITO strain sensor during 100 cycles at different strain levels (b). ITO bending results printed by ANM system for 1 cycle (c); Initial resistance: purple, 420 Ω cm; black, 550 Ω cm; red, 1300 Ω cm; green, 1600 Ω cm. The graph of normalized resistance variance at 0.19% strain during 9 cycles at 20 seconds (d) (inset is the optical image of the ITO strain sensor). SEM images of the ITO surface before (e) and after (f) stretching showing signs of crack formation (red ellipse).

The bending experiment was also used to demonstrate how the ITO resistance changes at different bending radii, as shown in **Figure 4.8**c. The initial resistance of printed samples was between 420 Ω cm to 1600 Ω cm. **Figure 4.8**d shows the normalized resistance variance of strain sensor during 20 seconds at 0.19% strain and 9 cycles. The inset image in **Figure 4.8**d

shows the printed ITO strain sensor on PET substrate. Furthermore, **Figure 4.8**e, f shows the SEM images of an ITO line before and after stretching. As it is shown in **Figure 4.8**f, under 0.9% displacement applied strain, small cracks appeared in the line that dramatically increased its resistance. Increased strain levels increase the crack density and widen the spacing between them, and hence the resistance increases. Adversely, when the cracks close, the resistance decreases.

4.4.2 Ag Temperature Sensor

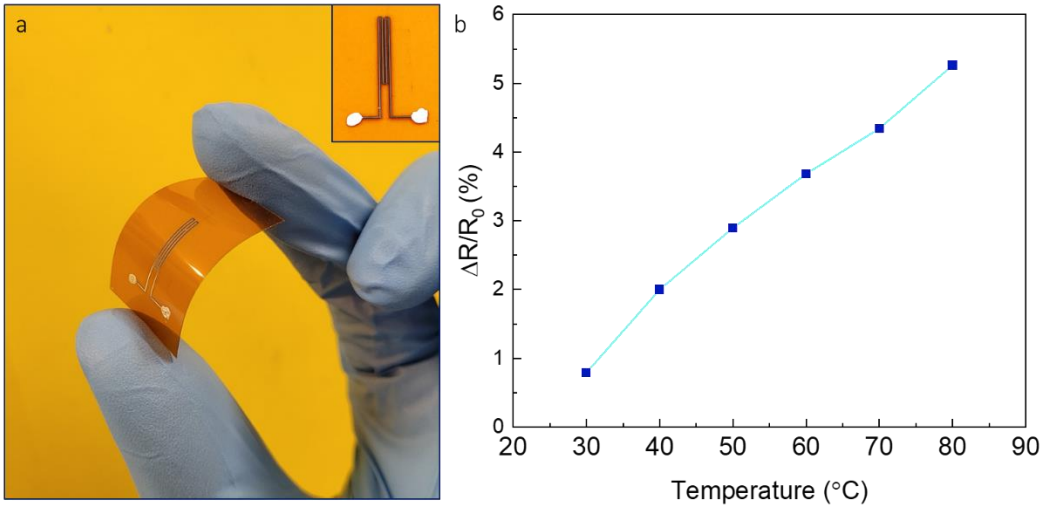

Figure 4.9. Optical image of a bent temperature sensor (a). The inset image shows the top-view picture of the temperature sensor. Relative resistance changes at temperatures ranging from 30 °C to 80 °C (b).

Ag meander-shaped ribbon (300 μm width and 1.5 cm length) was ANM-printed as a temperature sensor, as shown in **Figure 4.9**a. The sample was placed onto a hotplate to measure the sensor response, and the temperature measurement range was performed from 30 °C to 80 °C with 10 °C temperature increment and 5 minutes wait time at each temperature. **Figure 4.9**b presents the percentage of resistance change at different temperatures. The sensor temperature coefficient resistance was extracted to be about $8.77 \times 10^{-4} {}^{\circ}C^{-1}$ which is comparable with other Ag-based temperature sensors.[162]

4.4.3 Printing Flexible Hybrid Electronics (FHEs)

We designed and constructed several device prototypes to demonstrate the flexibility and applicability of our ANM process in printing FHEs on a polyimide substrate (**Figure 4.10**). As it is shown in **Figure 4.10**a, on the first step, conductive Ag tracks of the designed circuit were printed on polyimide substrates. Surface mount devices (SMD) and packaged electronic components (ICs and light-emitting diodes (LEDs)) were mounted on the predefined positions (**Figure 4.10**b). IC's pins and LEDs pads were connected to the ANM-printed circuit using a fast-drying Ag paint. The AT-Tiny 85 was programed by configuring an Arduino-Uno as an In-System Programming (ISP) using the Arduino IDE software. The program initialized the designated pins (0, 1, and 2) on the AT-Tiny 85 board (running at 8 MHz) as output pins for LED's and ran an infinite loop for sequentially powering the LED's with set delays. By applying 5V voltage to the circuit, as shown in **Figure 4.10**c-e, the LED's were turning on in sequential order. **Figure 4.10**f shows the circuit operating while it is bent and under strain.

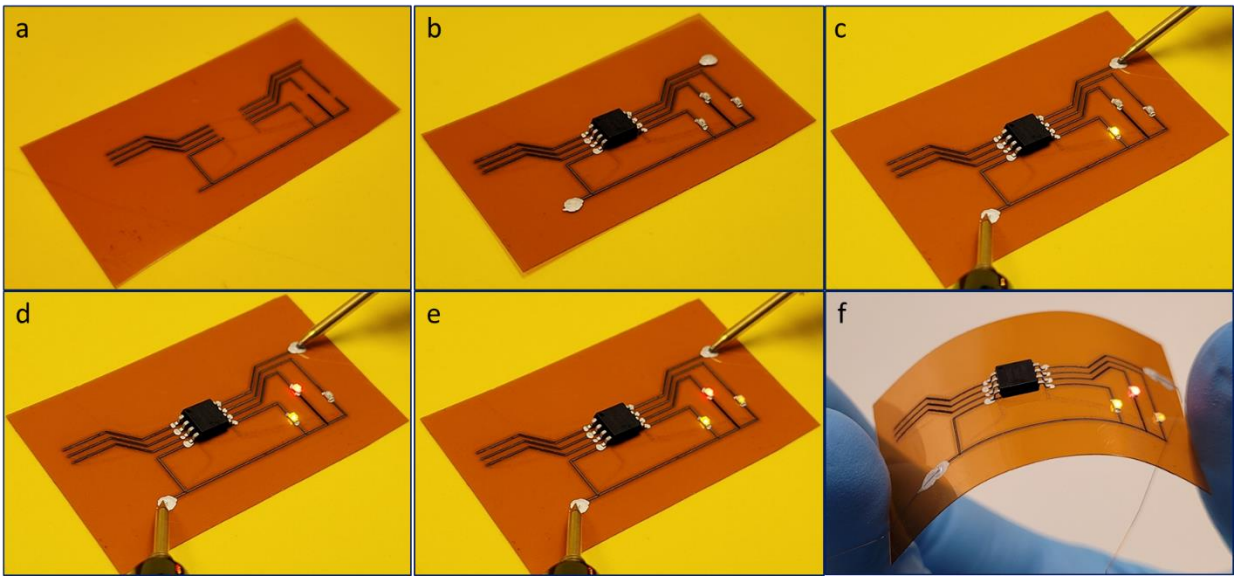

Figure 4.10. Conductive electronics circuit and pattern of Ag printed by ANM process on polyimide substrate (a). Mounted SMD IC and LEDs on the circuit (b). Sequential turning on LEDs programmed by IC while 5V is applied (c-e). Circuit working under bending pressure (f).

4.5 Conclusion

In summary, we demonstrated a dry printing additive nanomanufacturing of FHEs and sensors on flexible polyimide and PET substrates. In-situ laser-generated nanoparticles inside a microchamber were used as the building blocks for manufacturing and printing conductive and functional lines and patterns by laser sintering them onto the substrate as they exit the nozzle at room temperature and atmospheric pressure. Ag and ITO lines and patterns with resistance down to 1 Ω cm and 100 Ω cm, respectively, were achieved by controlling the number of printed paths and repetition rates while using optimum sintering laser energy. We ran mechanical reliability tests such as cycling (0.08% to 0.5% strain) and stretching (0.18% to 0.9% displacement) on additively manufactured Ag and ITO on 127 µm thick polyimide and 200 µm thick PET substrates, respectively. The results showed that all the Ag lines are still conductive at the highest testes strain, even after 1,000,000 cyclings. Also, ~5% to ~400% change of resistance in ITO-printed lines under 0.18% to 0.9% displacement. Conductive NFC antenna tag, strain sensor, temperate sensor, and FHEs were printed on polyimide and PET substrates, and their performances were measured. The printing flexibility, printed line quality, structural and mechanical properties as well as device performances demonstrated the potential use of the proposed system as an alternative and transformative approach for future printed flexible electronics and sensors.

CHAPTER 05

Ink-Free Printing of Copper via Additively Manufactured Electronics

5.1 Introduction

Conventional manufacturing techniques such as photolithography and vacuum deposition, involve many steps such as mask design and fabrication, dry and wet etching that are expensive, time consuming, and environmentally harmful. In addition to that, these techniques rely on high-temperature processing, therefore are limited to conventional substrates such as rigid silicon wafers and printed circuit boards since these substrates are able to withstand the high temperatures and pressures [13, 14]. A well-suited technology is needed for flexible or stretchable electronic devices.

An alternative approach is the additive manufacturing or 3D printing, which allows the creation of complex patterns layer by layer, and it has been adopted to fabricate various device components such as metals, ceramics and polymers. These technologies can help to reduce the number of steps and the environmental impact of manufacturing, and can also enable the use of a wide range of substrates, including flexible and wearable substrates. Micro-scale additive manufacturing (AM) technologies such as inkjet printing (IJP) and aerosol jet printing (AJP) have emerged as a solution for printable electronics technology [15-20]. The direct writing nature of AM eliminates waste of materials and many post processing steps of conventional methods. Many micro-scale additive manufacturing techniques use ink-based materials, such as conductive, resistive, and dielectric inks. Metal inks are needed to be annealed after printing so the nanoparticles sinter together for conductivity, and also to remove the solvents/additives in the

inks [21, 22]. Here the annealing temperature is much lower than conventional manufacturing technique, which enables the use of flexible substrates in micro-scale AM techniques. Nowadays, flexible substrates are recognized as one of the key foundations of printed electronics due to their extreme light weight, ability to conform and bend, and their wide range of applications including in wearables electronics, flexible displays, soft robotics, energy and storage [2-12].

Conductive materials such as gold (Au), silver (Ag) and copper (Cu) have many applications such as solar cells, flexible hybrid electronics, sensors, batteries and super capacitors [163-166]. Gold has high conductivity and it is also resistant to oxidation, however, high price of Au limits its use for printed electronics. As an alternative, copper and silver have similar conductive properties. Copper is cheaper than silver (1% of the price of silver) since its abundant in the Earth (copper is the 25^{th} while silver is the 68^{th}) [21]. Therefore, copper printed electronics and copper-based inks formulation are attracting great attention. However, there are some obvious problems in copper-based inks printing.

Firstly, melting temperature of Cu is more than silver. High electrical conductivity and resistivity of printed Cu demands optimized sintering process which is more than 150 °C. Flexible substrates such as PET, PDMS and paper cannot tolerate at that sintering temperature (>150 °C) [21, 167]. To overcome this limitation, polyimide (PI) kapton with high glass-transition temperature can be used. PI kapton is lightweight with a good thermal stability which makes it an ideal substrate for flexible and wearable technologies. Different ink formulations have been reported to lower the sintering temperature of copper inks [168-171]. Intense pulsed light sintering (IPL) has been proposed as a method to sinter as-printed Cu film by flash lamp exposure. This

technique enables inkjet and aerosol jet printing on thermal-sensitive flexible substrates without damaging underlying substrate [172].

The second challenge is that achieving low resistivity and long stability of ink-based Cu printed is difficult since copper is easily oxidized into copper oxide (CuO) and cuprous oxide (Cu_2O) when exposed to the air environment [173-175]. Some studies suggested stabilizing agents such as polyvinylpyrrolidone (PVP) in synthesizing copper nanoparticles (CuNPs) to protect from oxidation [176-178].

Deep knowledge, extensive effort, time, and cost of ink formulation in one hand, post thermal treatment to eliminate solvents and additives of inks on the other hand, has been resulted in many effort to invent new dry printing technology [121, 166, 179-181]. Sreenilayam et al. showed an additive-free process by using of laser ablation in liquid for nanoparticles generation and using it for aerosol jet printing, however, their technique still needs post processing [182]. Also, control of multiple parameters such as atomizer flow rate, sheath flow rate, nozzle size, printing speed, base temperature, and print height is not simple to get a fine print. Multi-material print via AJP is quite challenging due to different viscosity of the materials, cleaning of the nozzle to avoid blockage and so on [183]. The author reported a novel ink-free and dry additive nanomanufacturing (ANM) technique to print multifunctional materials and multi-materials such as TiO_2, BTO, ITO and silver on rigid and flexible substrates in a single step process with no need for post processing [121, 166, 179, 180].

In continuation of our previous works, we have used the additive nanomaufacturing technique as a dry and ink-free process to directly print and sinter Cu nanoparticles on flexible PI kapton substrates. On-demand dry Cu nanoparticles generation via a laser ablation process eliminated

the ink-related challenges mentioned before. In addition, dry, ink-free, and in-situ sintering of nanoparticles accelerates the printing process since no post treatment needed. We showed the good adhesion of printed Cu to the PI kapton substrate, perfect mechanical reliability under different bending radii and cycles, and some electronics devices and sensors to demonstrate the capability of our technique.

5.2 Results and Discussions

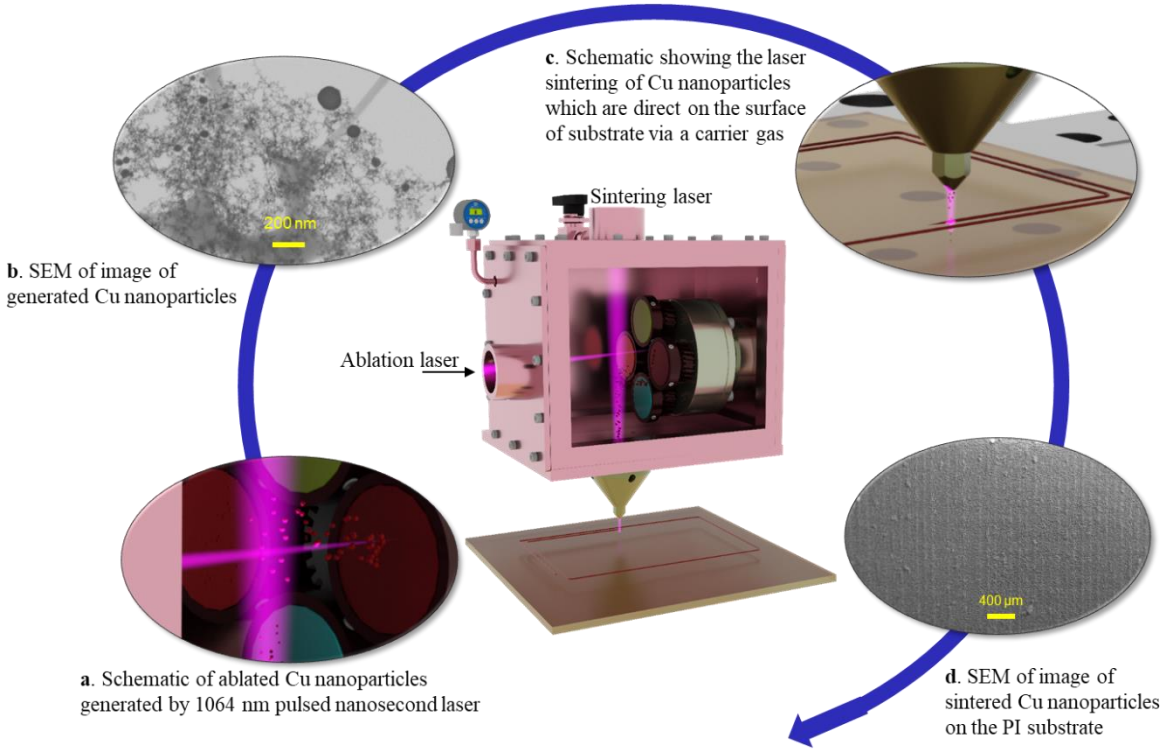

Figure 5.1. Schematic of additive nanomanufacturing printer. Enlarged illustration of on demand Cu nanoparticle generation (a) and in-situ sintering of Cu nanoparticles on the surface of a substrate (b). SEM of ablated Cu nanoparticle by a pulse nanosecond laser (c). SEM of real time sintered Cu nanoparticles onto the PI kapton substrate (d).

In principle, additive nanomanufacturing printer begins with on-demand Cu nanoparticles formation by laser ablation of a solid Cu target inside the chamber while an inert gas, here argon (Ar), is pumped in, as depicted in **Figure 5.1**. The generated Cu nanoparticles are streamed out

of the chamber through a nozzle by Ar carrier gas (1.186 SLPM), and are focused on the surface of the substrate. Simultaneously, while Cu nanoparticles are depositing on the substrate, a second laser passing through center of the nozzle sinters Cu nanoparticles. Enlarged schematic illustration of on-demand ablated and sintered Cu nanoparticles are demonstrated in **Figure 5.1a, c**, respectively. Scanning transmission electronic microscopy (STEM) and scanning electron microscope (SEM) were used to examine the morphology of ablated and sintered Cu nanoparticles. **Figure 5.1b** shows STEM image of on-demand ablated Cu nanoparticles with an average size of ~10 nm. The Cu nanoparticles with such as smaller radius can effectively reduce the temperature required for sintering [21, 184]. SEM image of laser sintered Cu nanoparticles is shown in **Figure 5.1d** which confirms the Cu nanoparticles sinter and fuse together to form a larger film. 1064 nm pulsed fiber laser coupled to a galvo scanner is used for the target scanning and ablation process. A second 1064 nm pulsed fiber laser passed through the nozzle and focused onto the substrate via a convex lens used for the sintering process.

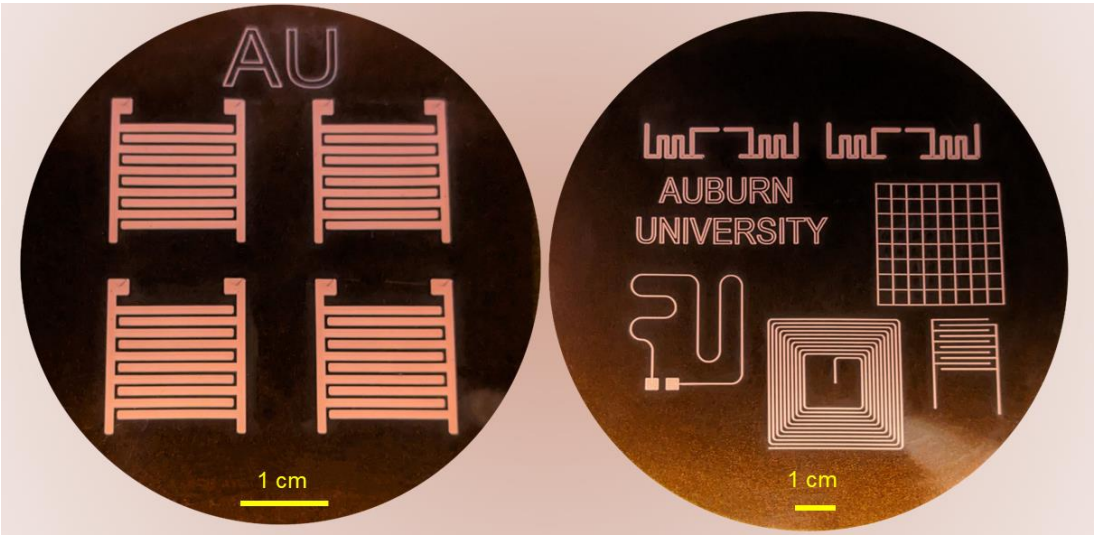

Figure 5.2. Cu-based interdigital pattern arrays, AU logo, RF and NFC antenna, heater and square matrix printed on PI kapton substrates by ANM technique.

As the main advantage of direct writing techniques, ANM does not need multiple masks designing for printing different patterns. Instead, it can easily be controlled by the printer software. **Figure 5.2** shows the potential of ANM technology to print some applications such as antenna, heater, interdigital patterns, humidity and temperature sensor on flexible substrates.

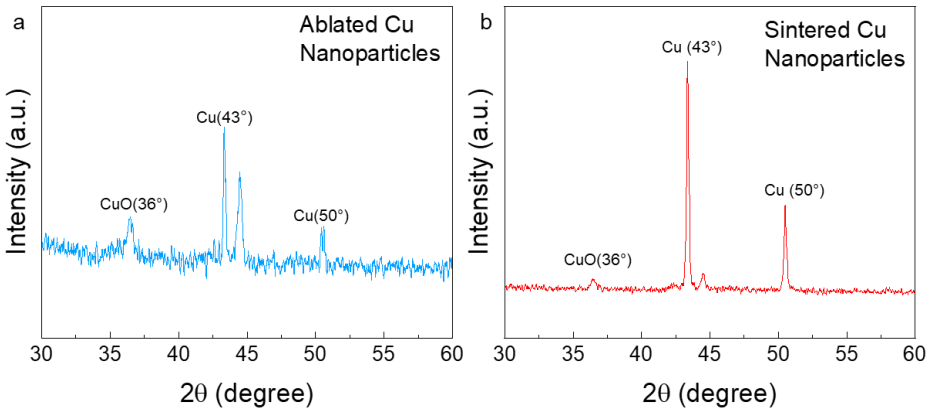

Figure 5.3. XRD plots of ablated Cu nanoparticles (a), and sintered Cu nanoparticles (b).

XRD measurements of air-exposed generated Cu nanoparticles before and after sintering is shown in **Figure 5.3 a-b** and two peaks at 43° and 50° are assigned for crystalline metallic copper. A general issue is that Cu nanoparticles are tending to oxidize in ambient and air conditions. The small peak at 36° is showing the presence of a small percentage of oxide in the ablated and sintered nanoparticles due to exposure to the air in ~4 hours. Some studies reported various approaches to prevent oxidation with coating of Cu nanoparticles by a protective layer such as organic polymer, alkene chains, and inorganic materials such as silica and inert metals [185]. The printed Cu samples with ANM printer were done at atmospheric pressure and room temperature. Creating an inert atmosphere with Ar around the print head, to eliminate water vapor and oxygen, will definitely improve the quality of oxygen-sensitive materials such as copper and aluminum.

Gas flow rate, laser ablation power, laser sintering power, nozzle size, print speed, number of printed layers and distance between the nozzle and substrate are the parameters which need to be controlled in the ANM process to print fine and good materials. For different gas flow rates, three different laser ablation powers, two different printing speed and five different printed layers has been studied while the laser sintering power, nozzle size and the nozzle and substrate distance kept constant 0.5 W, 400 µm and 1 mm, respectively. The summary of results has been shown in **Table 5.1**. It is worth to mention that increasing the power of ablation laser will result in generation of more nanoparticles and therefore increment of printed thickness in few printed layers which lead to lower resistance. Although, higher gas flow rate accelerates the deposition rate but since the higher flow affect the heat generated by the sintering laser and cooling process, and therefore at higher gas flow rate, sintering power needs to be more.

Table 5.1. ANM process parameters relationship at different gas flow rates, printing speed, and laser ablation powers.

Gas Flow Rate (SLPM)	Pass Layer	48W Laser Ablation Power		54W Laser Ablation Power		60W Laser Ablation Power	
		Resistance (Ω) at Printing Speed of 2mm/s	Resistance (Ω) at Printing Speed of 10mm/s	Resistance (Ω) at Printing Speed of 2mm/s	Resistance (Ω) at Printing Speed of 10mm/s	Resistance (Ω) at Printing Speed of 2mm/s	Resistance (Ω) at Printing Speed of 10mm/s
0.985	10	11.8	-	7.3	420	4.6	140
	20	5.8	210	4	45	3	26
	30	4.4	53	3.3	20	2.2	15
	40	4	31	2.9	15.3	2	13
	50	3.7	23	2.3	11.3	1.9	10
1.3	10	20	-	9.3	-	13	225
	20	7.3	-	5.5	90	4.5	58
	30	4.5	100	3.7	40	3.2	20.8
	40	3.2	40	3.3	36	3	15.8
	50	2.3	24	2.9	15	2.7	10.8
1.57	10	33	-	6.7	-	10	160

	20	8.1	-	3.4	42	6.1	48-
	30	5.3	238	2.4	19.6	3.8	27
	40	4.5	93	2.3	14	2.9	22.8
	50	3.7	27	1.9	8.6	2.3	19
2	10	26	-	13.2	-	10.8	260
	20	9.3	-	6	72	5.2	49
	30	6.3	350	4	31	4.1	26.4
	40	4.5	67	3.5	19	3.5	14.6
	50	4.2	31	3.2	15	3	13

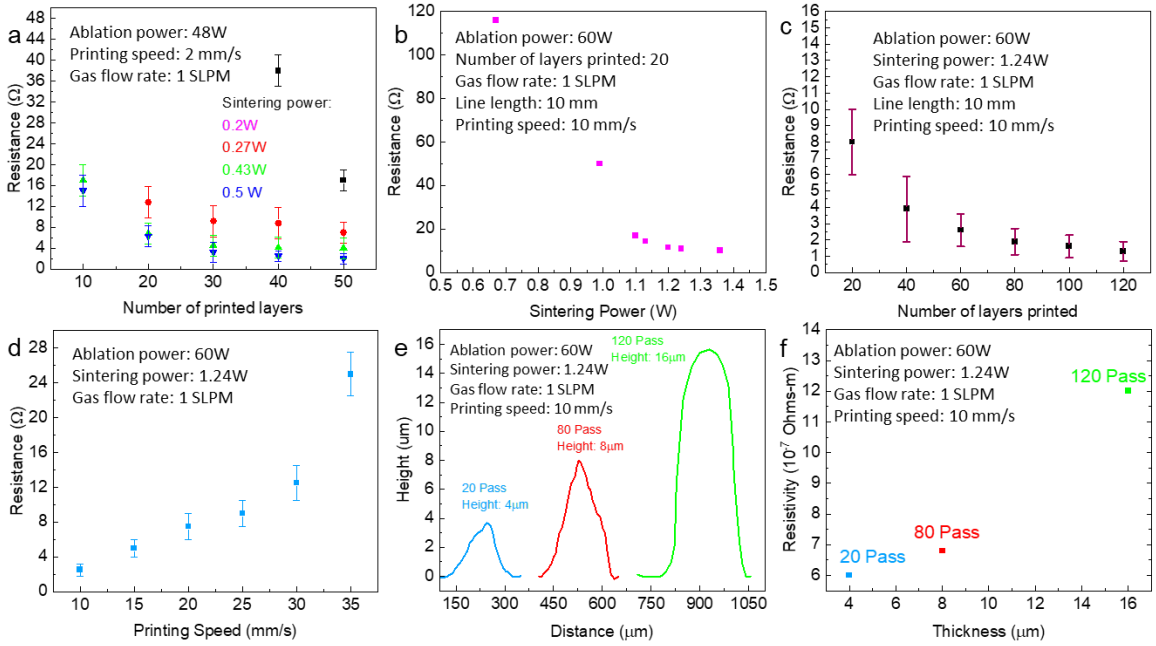

Figure 5.4. Resistance of 10 mm printed Cu as function of number of printed layers at different sintering powers for printing speed 2mm/s (a). Resistance of 20 layers printed Cu vs. sintering power at 10 mm/s printing speed (b). Resistance of Cu verses different layers printed (c). Resistance of Cu verses printing speed while all other parameters kept constant (d). Thickness profile of printed Cu at 3 different printed layers (e). Measured resistivity based on data of graph c and e (f).

Table 5.2. Comparison of materials, solvent/additive, method, post processing and resistivity of printed Cu using different technologies.

Materials	*Solvent/Additive*	*Substrate*	*Method*	*Post-processing method*	*Resistivity (μΩ.cm)*	*Reference*
Bulk Cu	-	NA	NA	NA	1.68	-
CuNPs	1-Octanethiol	PI	Inkjet	IPL	24	Ref.[186]
CuNPs	Polyvidone	PI	Inkjet	275 C° Thermal sintering	11.6	Ref. [177]
CuNPs	Polyvidone	PI	Inkjet	200 C° Thermal sintering	3.6	Ref. [187]
CuNPs	NA	PI	Aerosol	IPL	20	Ref. [183]
CuNPs	Not needed	PI	ANM	Not needed	12	This study

The effect of laser powers (0.2 to 0.5 W) on the resistance of Cu printed lines has been investigated at different printed layers for 2 mm/s printing speed. As it is showing in **Figure 5.4a**, at higher laser sintering power (such as 0.5 W), the resistance of printed 10 mm Cu line is lower than when using less sintering power such as 0.2 W. Suitable laser power will result in better melting and sintering of Cu nanoparticles and therefore better resistance. Higher speeds (such as 10 mm/s) need more power for sintering of the Cu nanoparticles and obtaining same resistance of 2 mm/s. **Figure 5.4b** confirm that at 10 mm/s, sintering power needs to be 1.24 W for better sintering. While all printing parameters such as ablation power, sintering power, gas flow rate and number of printed layers kept constant, the printing speed changed from 10 to 35 mm/s. As shown in the **Figure 5.4d**, the resistance increases at higher speed. It is possible to obtain lower resistance at higher speed by increasing several factors such as laser ablation power, the number of printed layers and sintering power. The thickness and resistivity of printed 1cm Cu lines as a function of number of printed layers are plotted in **Figure 5.4e, f**. The printed thickness in this case is in the range of 4 to 16 μm for the printing layers from 20 to 120. The Cu bulk resistivity is 1.6812 μΩ.cm. The lowest resistivity that we measured was 12 μΩ.cm. A comparison of materials, solvent/additive, method, post processing and resistivity of printed Cu

using different technologies such as inkjet and aerosol jet printing with our ANM technique is demonstrated in **Table 5.2**.

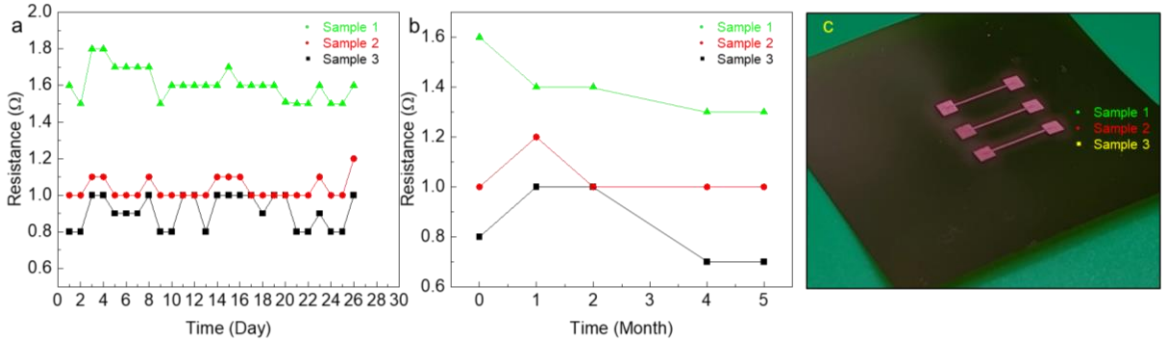

Figure 5.5. Plot of resistance variation versus day (a) and month (b) in air exposure for three different Cu printed on PI kapton showing the stable resistance in long period of time. Photograph of printed Cu samples (c).

The change in resistances of three different printed Cu 1 cm lines is measured with a multimeter under ambient condition and is plotted as a functional of day-by-day and per-month, as shown in **Figure 5.5a-b**. The resistances of printed Cu samples exhibited long-term stability (less than <0.3 Ohm change) over 5 months under ambient conditions without any encapsulation.

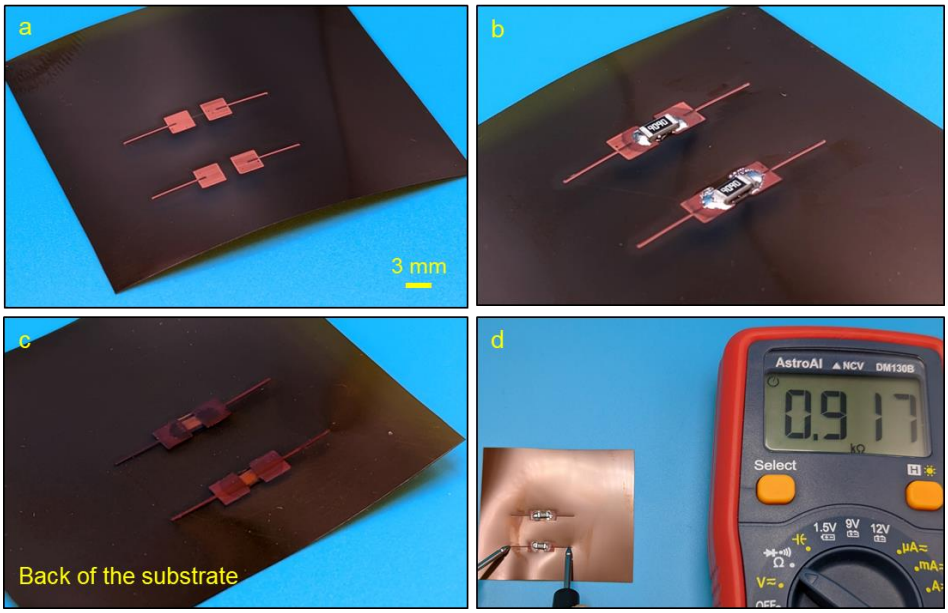

Figure 5.6. Photograph image of printed-Cu pads (a), ~900Ω SMD resistor reflow soldered to the Cu pads (b), back of the substrate after reflow soldering (c), measured resistance of the SMD resistor (d).

Low-temperature solder paste used to mount SMD components on ANM Cu printed pads. The solder paste used is SMDLTLFP Chipquik with a melting temperature of 138°C. All components were placed on PI kapton substrate with solder paste between each contact and its pad. Using a jet of hot air, the solder pastes melt and reflow and make all the connections. As shown in **Figure 5.6a-d**, we successfully mounted a ~909 **Ω** resistor using reflow soldering without any damage to the printed Cu pads which confirms the quality of sintering and printed Cu.

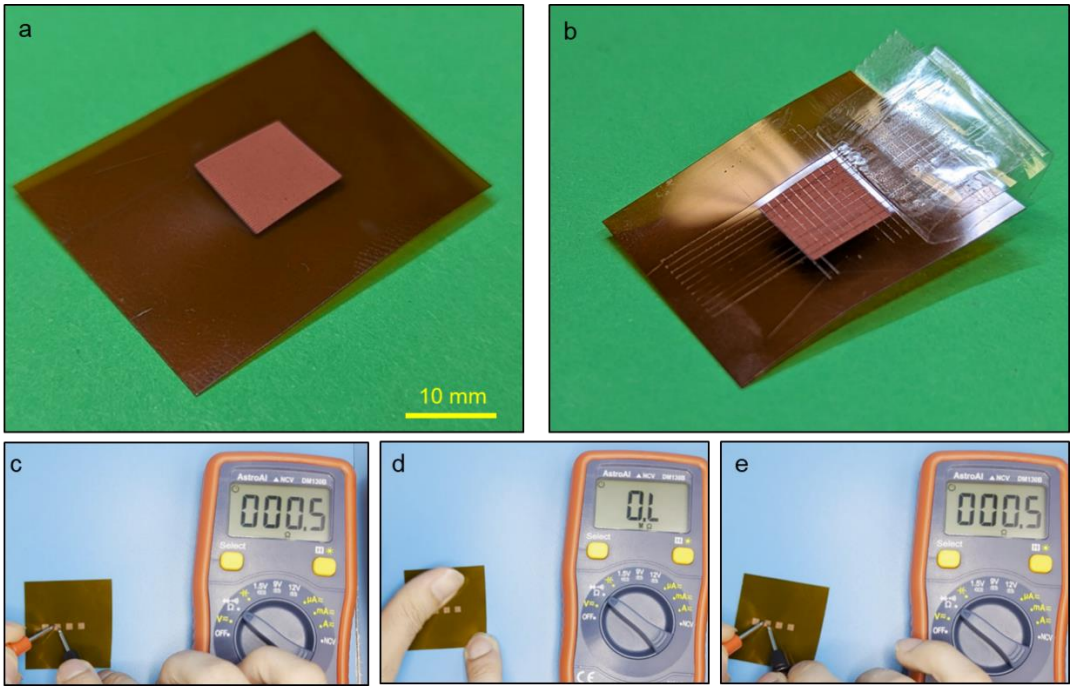

Figure 5.7. Digital photo of 1cm by 1cm Cu printed on PI kapton before adhesion test (a). Digital photo of same printed Cu sample after adhesion test and removing of adhesion tape (b). Photograph image of Cu printed samples before and after scratching the surface with hand showing same resistance (c).

In order for printed Cu on PI kapton substrate to fulfill its functionality for future flexible and wearable applications, the printed Cu must remain adhered well to the PI kapton substrate. The adhesion of the inkjet printed Cu to the substrate is a major problem. Researchers tried adding cellulose to ink or substrate pretreating to increase the adhesion of printed Cu to the substrates

[188]. Here, the adhesion test of ANM printed Cu films to the substrate was performed according to the American Society for Testing and Materials (ASTM D3359) procedure. Cross-cut pattern (1mm space) was generated on the printed sample using a multi-blade cutter. The adhesion tape was applied to the sample and then removed. **Figure 5.7a** shows a 1 cm by 1 cm printed Cu before the adhesion test. **Figure 5.7b** shows the remaining area rate after the tape test which shows ASTM 5B (the highest level of adhesion is 5B and lowest is 0B). In addition, as demonstrated in **Figure 5.7c-e**, the resistances of printed Cu samples was measured before and after scratching with bare hand multiple times, and the results showed no change in the resistance.

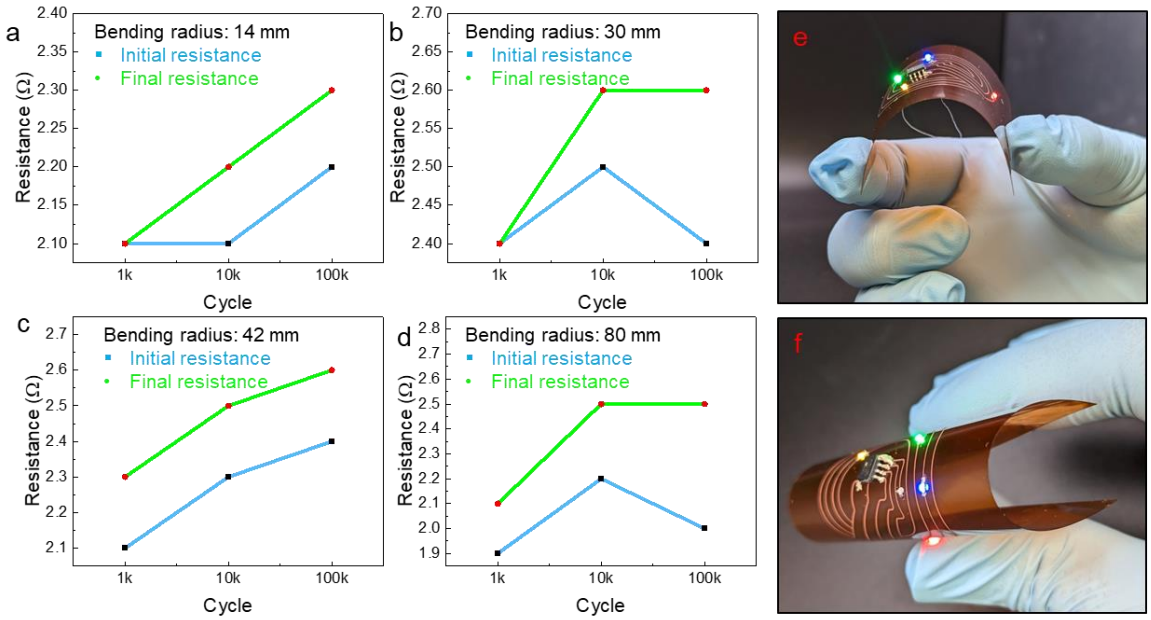

Figure 5.8. Initial and final resistance of Cu-printed 1 cm line samples at different bending cycles and radii (a-d). Photograph image showing well-functioning Cu-based flexible hybrid electronic at different bending radii (e, f).

Flexible devices must be capable of undergoing deformation and at the same time the functional properties and electronic performance parameters must be unaffected by the strain process. Different applications demands different flexibility of printed samples [189]. For example, biosensors directly connects to human skin, therefore high strain is needed. Repetitive strain

cycles are expected for some other applications such as flexible membrane switches [190]. Similarly, for devices that actively measure strains or harvest energy from strain (strain sensors and piezoelectric generators, for instance), the response to strain should be consistent throughout the entire device lifetime [190].

Figure 5.8 demonstrates another adhesion strength test of ANM printed Cu on PI kapton substrate. Here we have performed bending test at 1K, 10K and 100K cycles for different range of bending radii (14 to 80 mm) to confirm the suitability and applicability of printed Cu for the aforementioned applications. The initial and final resistance of 1 cm printed Cu lines at different bending radii and cycles are plotted in **Figure 5.8 a-d**. Resistance of the lines is stable at first 1K cycle in all different bending radii. At higher cycle (10K and 100K), the resistance is increasing slightly likely due to defects created by the compression-extension cycles. A 4 LED flexible hybrid electronic circuit printed by Cu nanoparticles were subjected to two different bending radii, as showing in **Figure 5.8 e,f**, and the circuits worked well even under too much strain.

5.3 Conclusion

We has used a new dry additive nanomanufacturing as an emerging technology to print pure and ink-free Cu nanoparticles on polyimide substrate for flexible hybrid electronics and sensors applications. The laser ablation of solid Cu target generates on-demand dry Cu nanoparticles in presence of an Ar gas. The generated Ar jet flow carries the Cu nanoparticles onto the surface of polyimide kapton substrate. A secondary laser sinters the Cu nanoparticles without damaging the substrate in real-time. Using this technique, we were able to get the 12 μΩ.cm resistivity. Resistance of printed Cu measured in 5 months showed negligible variation, confirming the good stability of printed Cu in long time. 5B classification of ASTM adhesion test confirmed the good

adhesion between the sintered Cu and polyimide kapton substrate. To demonstrate the mechanical reliability of printed Cu, different bending radii and cycles were tested and results showed the excellent reliability of samples. The ANM printer was used to print Cu-based patterns, flexible hybrid electronics, antenna and sensor that has wide range of applications in oil and gas industry, flexible electronics, medical and energy storage.

CHAPTER 06

Multimaterial Additive Nanomanufacturing and Dry Printing of Flexible Hybrid Electronics

6.1 Introduction

With the emergence of the internet of things (IoT), where most objects and systems are anticipated to be made smart, there is great interest in developing new materials and advanced manufacturing techniques in order to integrate various functionalities, including sensors, batteries, displays, and electronics directly onto different surfaces [191-196]. Printed flexible electronic devices are often lightweight, bendable, stretchable, and wearable, with potential applications in healthcare, energy, aerospace, and defense industries [197, 198]. Currently, flexible electronics are mostly fabricated with a single material in a single layer [199-202]. Most devices and structures with sophisticated functionalities, such as electronics, optoelectronics, and sensors, typically require multimaterial deposition. Thus, there are emerging needs for printing methods that allow multimaterial printing in multilateral configurations.

Currently, state-of-the-art printed electronics revolve around ink-based manufacturing techniques such as inkjet and aerosol jet printing (IJP and AJP) [17, 23, 28, 146]. These direct printing methods overcome the challenges of conventional lithography-based processes, which require expensive manufacturing facilities with complex and wasteful processes [166, 179, 180, 196, 203-211]. IJP and AJP techniques have been mostly successful in printing a limited single material in a single process step. A few printing methods have also been reported that are capable of printing multimaterials [212-218]. For example, Skylar-Scott et al.[219] reported a micrometer-scale printing strategy by fast switching between viscous materials which are extruded through a single nozzle. Wanjun Liu

et al.[220] developed an extrusion-based multimaterial bioprinting platform capable of depositing multiple coded bio-inks in a continuous manner with switching between different reservoirs. Ke Sun et al.[221] showed 3D interdigitated microbattery architectures by printing concentrated lithium oxide-based inks. Although these extrusion-based printing methods have been used to fabricate functional devices [221-227], the construction of multimaterial architectures often involves sequentially printing individual materials using multiple nozzles. Besides the limited availability of the source materials for printing, the drawbacks of printing one material at a time include the need for careful alignment of each nozzle as well as start-and-stop ink flow on demand without introducing defects [228, 229].

Ink-based printing techniques have several other disadvantages as well. The ink formulation is complex, and developing individual functional ink requires extensive effort, time, and cost. For example, preparing a functional ink requires multiple steps, including nanoparticle preparation, nanoparticle suspension in a solution, particle dispersion, centrifugation, homogenization, and controlling the adhesion and viscosity of inks [228]. Thus, multimaterial printing is mainly limited to non-functional materials due to the trade-off between ease of processing and functionality [230]. Also, using solvents and additives for tuning the concentration of the inks requires additional surfactant removal and thermal annealing steps, which complicates the device manufacturing process [151, 231]. Moreover, in solvent-based printing methods, only materials that are soluble in the printing solvent can be used. However, many functional materials do not dissolve in common solvents, which significantly limits material selection. New technology is therefore needed to print fully functional, pure multimaterial structures and devices using a single printer and in a single process step.

Here we introduce multimaterial additive nanomanufacturing (M-ANM) and dry printing technology for printing various pure materials and hybrid structures in a single print. This method can eliminate the need for assembly, reduce the need for post-processing, and promote the efficient design of multifunctional devices. This particle-by-particle and layer-by-layer printing approach is capable of printing various materials by switching between the target materials in a single run during the print process. The M-ANM is a laser-based technique that generates nanoparticles on-demand and in situ by pulsed laser ablation of solid targets. The generated nanoparticles inside the printer head are then guided toward the nozzle and onto the surface of the substrate by a gas flow, where they are sintered and printed in real-time by a second laser. A target carousel holding multiple targets is rotated to bring a particular target into engagement with the ablation laser beam when needed. The rotation of the targets in predetermined sequences allows the printing of multiple materials onto the substrate in a single process step. For instance, here, we show the printing of hybrid multimaterial structures using various materials such as barium titanate (BTO), titanium dioxide (TiO_2), tin oxide (SnO), zinc oxide (ZnO), aluminum oxide (Al_2O_3), and silver (Ag). In addition, to demonstrate the capability of the M-ANM system, fully printed multimaterial devices such as Ag/ZnO photodetectors and Ag/Al_2O_3 electronic circuits are prepared and tested.

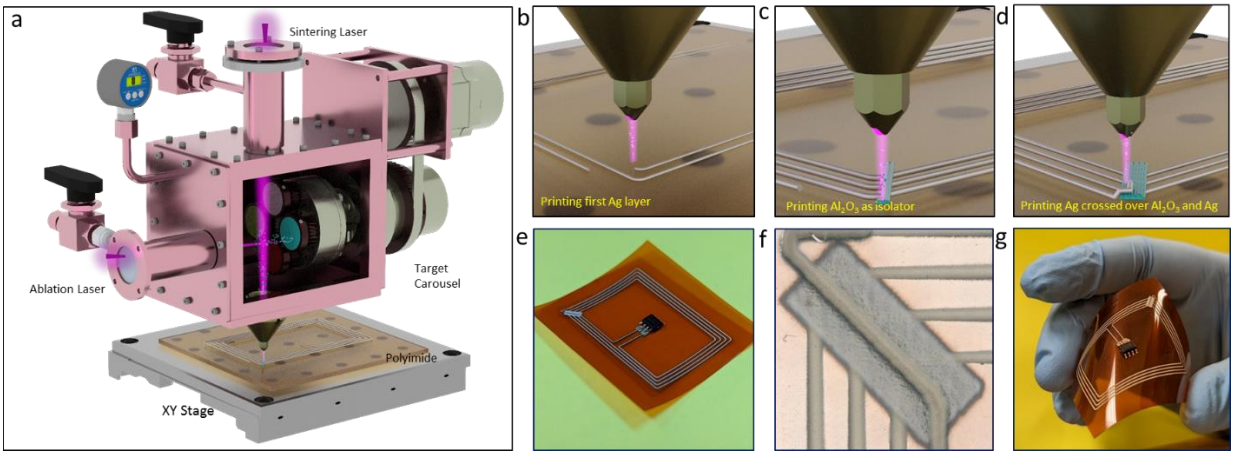

Figure 6.1. Schematic illustration of the multimaterial additive nanomanufacturing (M-ANM) and dry printing method (a). An example of the process flow for printing a multimaterial conductor/insulator (Ag/Al_2O_3) hybrid structure (b-g). First, Ag antenna pattern is printed on the polyimide substrate (b). The Al_2O_3 layer is printed on a section of the Ag lines as an isolating bridge layer (c). Ag is printed crossing over the top of the Al_2O_3 layer to complete the NFC antenna device (d). Photograph of a completed circuit with a M24LR04E IC chip mounted on the printed antenna (e). Close-up optical image of the printed insulating Al_2O_3 bridge with the crossed Ag lines (f). Image showing the flexibility of the multimaterial printed hybrid NFC antenna (g).

6.2 Experimental Section

A schematic representation of the dry printing M-ANM method is shown in **Figure 6.1**a. This dry multimaterial printer consists of a nanoparticle generation chamber, a nozzle, a target carousel holding multiple targets inside the chamber, a pulsed laser for target ablation and nanoparticle generation, a gas flow system, and a second laser for sintering the nanoparticles as they land on the substrates placed on an XY stage under the nozzle.

To demonstrate multimaterial printing, we first printed a silver-based NFC tag antenna with Al_2O_3 as the isolating layer. First, the target carousel was adjusted to position the Ag target for laser ablation and nanoparticle generation process. The nanoparticles were guided toward the substrate through the nozzle using an argon gas flow. These nanoparticles were then laser sintered on the flexible polyimide substrate in real-time (**Figure 6.1**b). After printing the first predesigned Ag layer, the nanoparticle generation stopped, and the printer head was quickly pumped to remove the residual silver nanoparticles. Then target carousel was rotated to bring the Al_2O_3 target in position for nanoparticle generation and subsequent printing processes (**Figure 6. 1**c). Finally, for printing the third layer Ag line crossing the insulator bridge, the printer head was quickly pumped, and the target carousel rotated back to position the Ag target for nanoparticle generation and printing processes (**Figure 6.1**d). The NFC tags are magnetically coupled by inductive loop antennas. A battery is not required to access the tag, whether in write or read

mode, since the tag harvests the energy needed to operate from the electromagnetic field generated by the reader. **Figure 6.1**e shows the completed circuit where the M24LR04E IC is mounted on the printed circuit. The mounted M24LR04E IC was programmed to launch the group's website when brought to the proximity of a cellphone with NFC system. **Figure 6.1**f and g show the close-up optical images of the isolating Al_2O_3 layer between crossed Ag lines and the flexibility of NFC antenna, respectively.

The important parameters for the ablation of a target and nanoparticle generation are laser power, scan speed, and repetition rate. Also, in our laser sintering process, the major processing parameters that affect the sintering of generated nanoparticles on the surface of polyimide substrate include the laser power, repetition rate, printing speed, and the number of printing layers. In general, the size and thickness of prints are controlled by nozzle diameter, the number of printing layers, printing speed, and gas flow rate.

The laser source for ablation was a pulsed fiber laser (1064 nm) with 1 mJ maximum energy per pulse. All the samples were printed at room temperature and atmospheric pressure onto ~127 μm thick polyimide substrates. The substrates were located ~1 mm below the nozzle tip, and the gas flow rate was kept at ~1000 sccm constant during all experiments. It is worth mentioning that we have previously shown the possibility of employing different types of lasers (e.g., 248 nm excimer laser) for both ablation and sintering processes [166, 179].

5.3 Results and Discussions

To get a better insight into the size and shape of the nanoparticles, scanning transmission electron microscopy (STEM) was used to confirm the formation of different nanoparticles such as BTO, TiO_2, SnO, and ZnO, as shown in **Figure 6.2**a-d, respectively. In general, the nanoparticles were in the order of ~3 to 10 nm in diameter. The scanning electron microscopy

(SEM) images in **Figure 6.2**e-h show the deposited and laser-sintered BTO, TiO_2, SnO and ZnO nanoparticles, respectively.

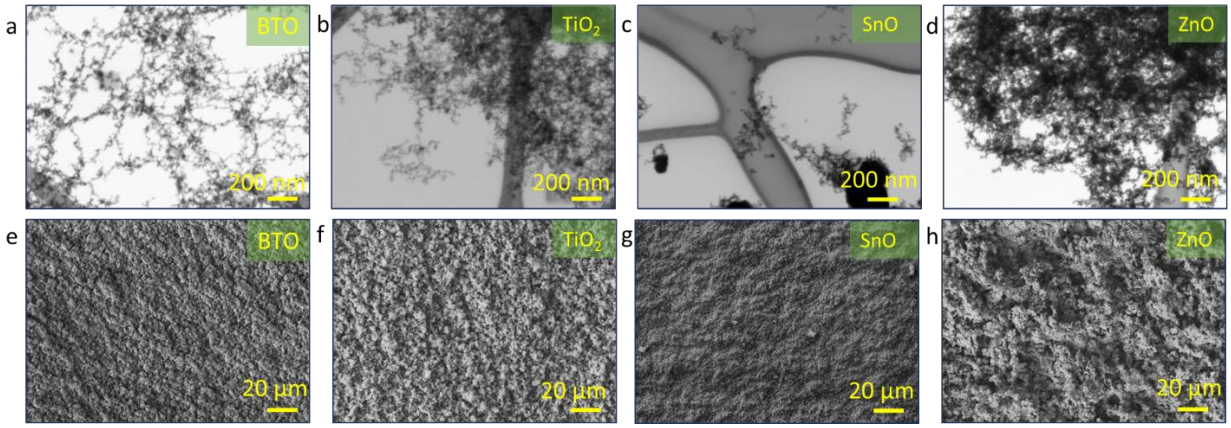

Figure 6.2. STEM images of BTO (a), TiO_2 (b), SnO (c), and ZnO (d) nanoparticles generated by M-ANM printer. SEM images of BTO (e), TiO_2 (f), SnO (g), and ZnO (h) sintered by ANM printer.

The effect of laser sintering on the crystallization and sintering of BTO, TiO_2, SnO, and ZnO nanoparticles were further studied by Raman and X-ray spectroscopy methods, as shown in **Figure 6.3**. After the sintering process, the Raman spectra clearly showed the characteristics vibrational modes of the samples. For instance, the Raman modes of the sintered BTO samples were observed at 260 cm^{-1}, 302 $cm^{-1,}$ and 717 cm^{-1}, representing the crystalline characteristics of the samples (**Figure 6.3**a). Similarly, the Raman active modes of TiO_2 crystals, including 137 cm^{-1}, 386 $cm^{-1,}$ and 625 cm^{-1} (**Figure 6.3**b) were observed, indicating the anatase phase of the crystallized TiO_2 samples. The Raman spectrum of SnO showed the A_{1g} phonon mode at ~204 cm^{-1} (**Figure 6.3**c), and ZnO showed the representative Raman modes at 435 $cm^{-1}$and 574 cm^{-1} (**Figure 6.3**d). **Figure 6.3**e-h demonstrates the X-ray spectra of sintered BTO, TiO_2, SnO, and ZnO, respectively, reconfirming the crystallinity of the sintered nanoparticles.

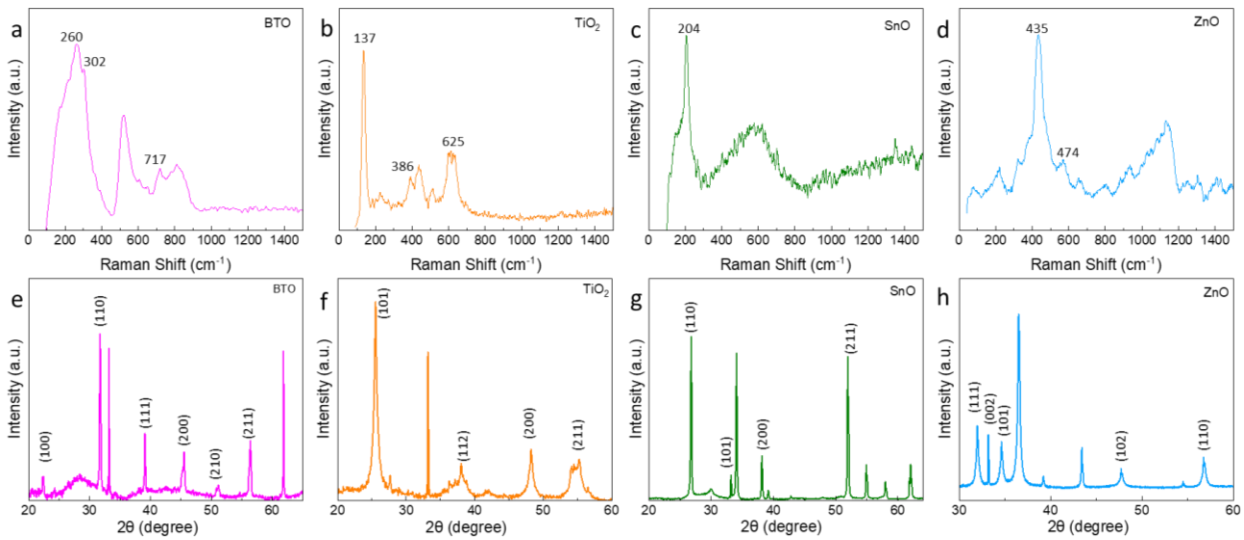

Figure 6.3. Raman spectra of sintered BTO (a), sintered TiO_2 (b), sintered SnO (c), and sintered ZnO (d). XRD plots of sintered BTO (e), sintered TiO_2 (f), sintered SnO (g), and sintered ZnO (h).

The versatility of the M-ANM technique enabled us to directly print multiple materials onto the desired location, either side-by-side or in a layer-by-layer configuration. As an example, the Ag-SnO-ZnO heterojunctions were printed side-by-side as shown in **Figure 6.4**a. The close-up views of the junctions are shown in **Figure 6.4**b-d. Also, as shown in **Figure 6.4**e and f, BTO/ZnO/TiO_2, and BTO/ZnO/SnO patterns were printed on polyamide substrates by rotating the target carousel to bring a particular target into position for nanoparticle generation and sintering processes. The SEM cross-section of the TiO_2-Ag multilayer produced by the M-ANM technique is presented in **Figure 6.4**g. Energy dispersive spectroscopy (EDS) element maps shown in **Figure 6.4**h-j indicate the capability of heterostructures formation made of multiple materials with clear boundaries.

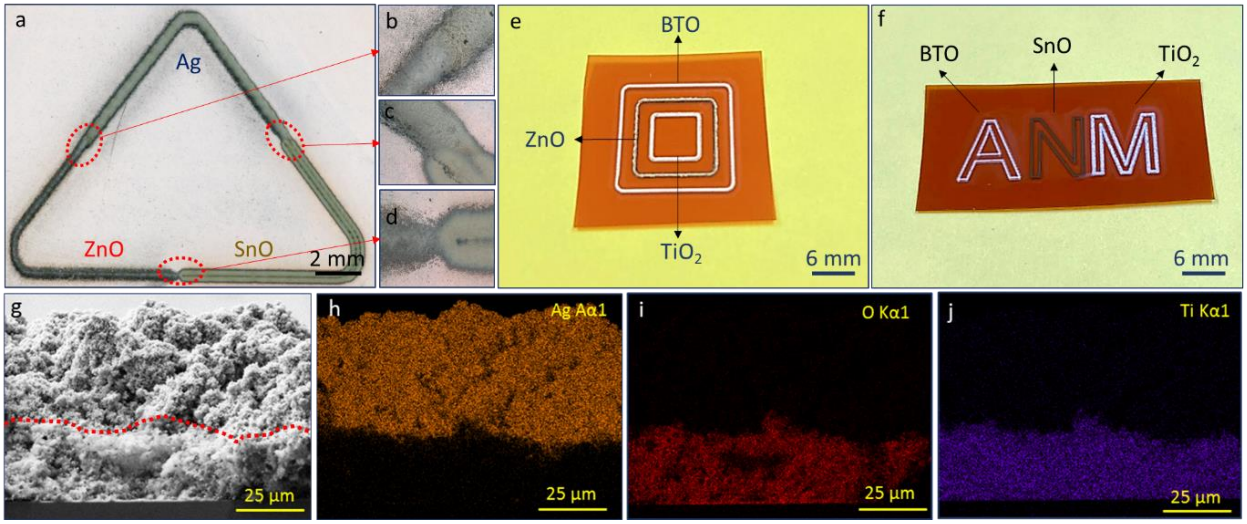

Figure 6.4. Optical image of side-by-side M-ANM printed Ag-SnO-ZnO lines (a). Optical images of Ag-ZnO (b), ZnO-SnO (c) and Ag-SnO (d) junction. (e, f) Optical images of BTO, ZnO, and TiO_2 printed on polyamide in a single run. Cross-section of printed Ag on top of TiO_2 (g). EDS elemental maps of printed TiO_2/Ag hybrid structure layer-by-layer (h-j).

To understand the correlation between the number of printed layers and the thickness of the printed lines, their height profiles were measured and analyzed using a KEYENCE optical microscope. As shown in **Figure 6.5**a, by increasing the number of printed passes, the thickness of the printed lines could simply be adjusted. For instance, increasing the number of printed passes from 10 to 100 layers resulted in thicknesses ranging from ~1 to 16 microns. **Figure 6.5**b represents the resistance of the printed Ag lines as a function of printed pass numbers. The lines resistance decreased by increasing the number of printed passes and hence increasing the thickness of the printed lines. Based on the results from **Figure 6.5**a,b, the resistivity of the 10 mm lines at different pass numbers was calculated and plotted in **Figure 6.5**c. Accordingly, we achieved resistivity as low as ~1×10^{-7} Ω m at a thickness of ~1 µm.

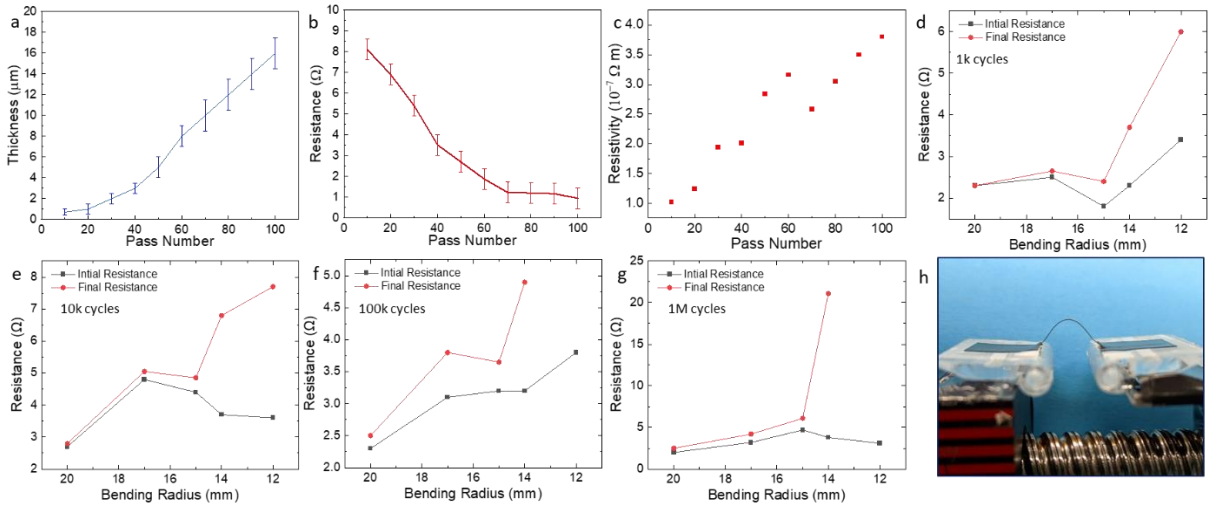

Figure 6.5. Thickness (a), resistance (b), and resistivity (c) plots as a function of the number of printed layers ranging from 10 to 100 passes. Initial and final resistances of the printed Ag-lines under various bending radii and cycles, including 10^3 (d), 10^4 (e), 10^5 (f), and 10^6 (g) cycles. Digital photo of custom-made bending and cycling machine (h).

The mechanical stability, structural durability, and electrical properties of the printed lines were characterized by performing bending and cycling tests (**Figure 6.5**d-g). The cycling test on a series of 10 mm printed Ag lines on 12×4×0.127 mm^3 polyimide substrates was performed using a custom-made bending system (**Figure 6.5**h). The initial and final resistance of printed lines at different bending radii (12-20 mm) and cycling numbers (10^3, 10^4, 10^5, and 10^6) were measured and plotted, as shown in **Figure 6.5**d-g.

To demonstrate the multimaterial printing capability of the approach, various devices were designed, printed, and tested. For instance, since photodetectors are an important class of optoelectronic devices and sensors that translate optical information into an electrical readout [232], we printed an array of Ag-ZnO photodetector printed on flexible polyimide substrate, as shown in **Figure 6.6**a-c with 2D and 3D optical images. First, Ag electrodes were printed, followed by switching the target and printing ZnO. The electrical and optoelectronic performances of the fabricated photodetectors were measured by a semiconductor

characterization system (Keithley 2400) under controlled UV LED (0.6 W@405 nm) illumination. All measurements were performed at atmospheric pressure and at room temperature. The UV LED was turned on and off with 0.5 Hz frequency. As shown in **Figure 6.6**d,e, the photocurrent spontaneously increased upon UV irradiation under different voltage biases (1-5V) and different illumination power densities (0.15 to 0.55W/cm^2). The device exhibited good flexibility and stability even after bending under different bending radii (**Figure 6.6**f,g). The UV intensity dependence in **Figure 6.6**h shows linearity over the power density from 0.15 to 0.55 W/cm^2, and the sensitivity is measured as 0.6 μA per 0.1 W/cm^2.

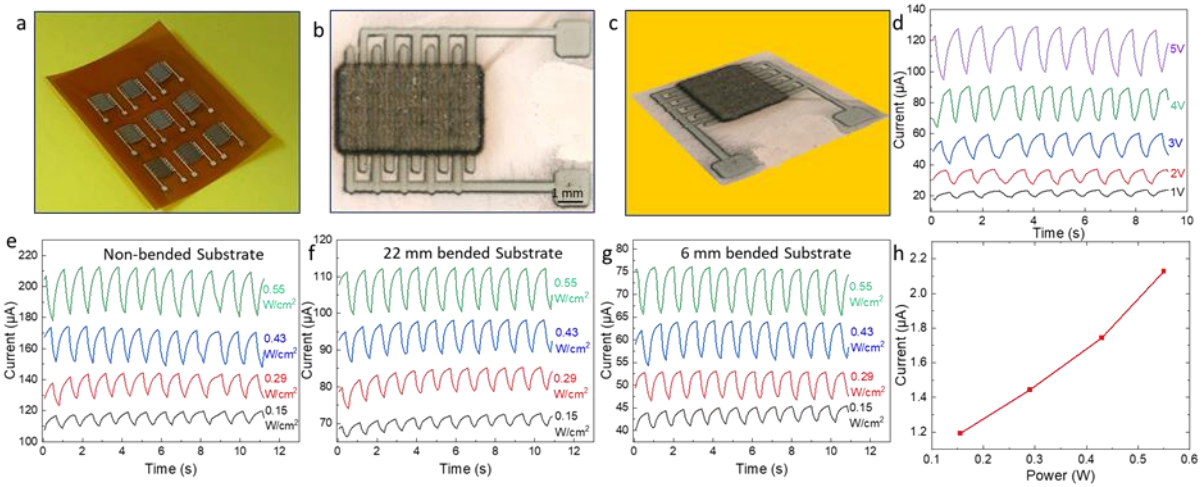

Figure 6.6. Digital photo of flexible Ag-ZnO photodetector arrays (a). 2D (b) and 3D (c) optical images of printed ZnO-based photodetector. Photoresponses of the sensor under various biased voltages (d) and light intensities (e). Photoresponses of the ZnO photodetector under various illumination intensities under different bending radii (f,g). Peak current of photodetector as a function of power density (h).

Another significant challenge in printed electronics is to create line cross-overs without shorting the circuit [123]. This requires a multimaterial printing capability for printing an insulating layer between the conducting lines. **Figure 6.7**a shows an example of a printed multimaterial flexible electronic circuit on polyimide using Ag lines as a conductive layer and Al_2O_3 layer as a dielectric isolator. To print this device, we designed and printed the first Ag layers. The Ag lines

exhibited a resistivity of ~1.2×10^{-7}Ω m. By rotating the target from Ag to Al_2O_3, the Al_2O_3 dielectric layer was printed on the pre-defined locations to electrically isolate the crossed Ag lines. Finally, the Ag lines were printed on the desired location and crossed over the insulating layers to complete the circuit. The 3D view image and height profile in **Figure 6.7**b,c shows the printed multilayer stack of Ag/Al_2O_3/Ag. After printing, the circuit electronics component, including the M24LR04E IC, AT-Tiny 85, two 1KΩ resistors, and two LEDs were mounted on the printed flexible circuits, as shown in **Figure 6.7**d. The printed device was powered by a 3.3v coin cell battery. This circuit used the printed NFC antenna along with NFC IC and AT-Tiny 85 microcontroller to read the NFC Data Exchange Format (NDEF) message from a phone via NFC program to control two output LED's. The expected operation of the circuit shows that the printed insulating Al_2O_3 layer completely isolated the bottom and top metal layers. Also, the crossed-over Ag lines were highly conductive. Furthermore, using this printing method, by controlling the printing conditions, vertical interconnects that can bridge different heights can be fabricated. The test results confirmed that separate multilevel metal interconnects were successfully formed.

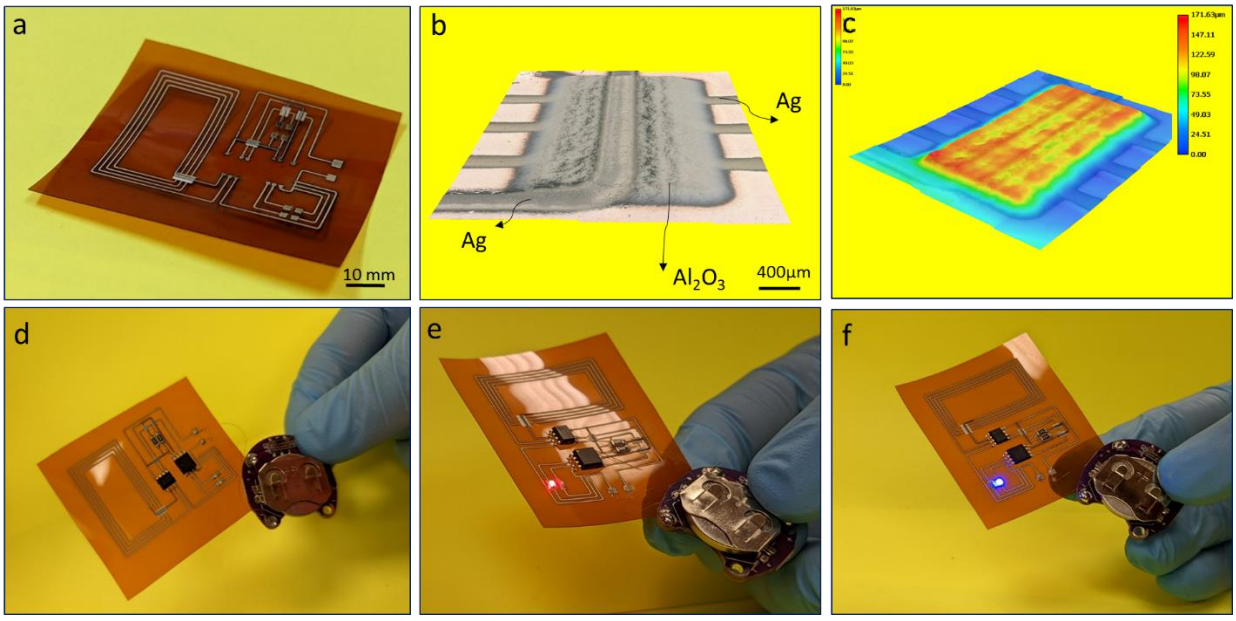

Figure 6.7. Digital photo of the M-ANM printed lines of flexible hybrid electronics (a). 3D optical image of the printed Al_2O_3 as the isolator layer between crossed Ag lines of the NFC antenna (b). The height profile image printed Al_2O_3 section in the NFC antenna with a thickness of ~140 μm (c). Completed flexible hybrid electronic circuit with all mounted components (d). Digital photo of the circuit showing the red (e) or blue (f) LED switching via NFC communication controlled by a mobile phone.

5.4 Conclusion

In summary, we developed a new dry multimaterial printing technique that is capable of printing multiple materials side-by-side and layer-by-layer. The unique feature of this technique was the generation of dry and pure nanoparticles through pulsed laser ablation of solid targets. The generated nanoparticles directly exited from the nozzle toward the substrate, where they were sintered by a real-time laser sintering process at room temperature and atmospheric pressure. A target carousel holding multiple targets was used to bring different targets in engagement with the ablation laser beam to print multiple materials. To demonstrate the capability, ZnO photodetectors with Ag electrodes and multimaterial Ag-Al_2O_3 FHE circuits were printed and tested. This versatile and unique M-ANM printing technique was used to print a variety of materials such as Ag, BTO, TiO_2, SnO, ZnO, and Al_2O_3 that could be used for broad applications ranging from flexible electronics, optoelectronics, energy storage and harvesting, space, and medical applications.

CHAPTER 7

Hybrid Subtractive and Additive Manufacturing for Flexible Electronics

7.1 Introduction

Flexible electronics has gained a lot of attention in recent years due to its many advantages and potential applications. Their flexibility makes them more durable to damage and other environmental stresses. In addition, flexible substrates are lighter and thinner than rigid substrates, which make them the ideal platform for lightweight applications such as wearables or medical sensors.[233-240]

One of the key advantages of flexible electronics is the ability to use in curved or irregularly shaped structures such as the human body. In addition, the most significant feature of flexible devices is where the printed material needs to be able to withstand repeated bending and flexing without delaminating from the substrate. Therefore, the reliability of flexible electronics is an important issue because the failure of flexible electronics can cause safety problems, as well as operational malfunctions. Manufacturing defects, crack and delamination are some causes of reliability failure in printed electronics processes.[191, 241-244] Improvement of such challenges has become a key issue in printing different nanoparticles on flexible substrates. Polymer substrates have attracted extensive research interest for flexible or wearable electronic devices. Among them, polyimide (PI) is a compatible and promising substrate because of its high heat resistance and stability, excellent mechanical property, and high chemical resistance.[245]

The formation of a trench is a useful technique for improving the reliability of printed materials, particularly for flexible electronics. The formation of a trench on PI substrate can improve the reliability of printed materials by increasing the mechanical interlocking and interfacial region

between the printed material and the substrate. When a trench is formed on the PI substrate, it creates a larger surface area for the printed material to adhere the PI substrate, which improves its adhesion and mechanical stability. In addition, the formation of a trench can also help to reduce the stress and strain on the printed material by distributing the forces more evenly across the surface of the material. This can help to prevent cracks and other forms of mechanical failure. For example, Matsumura et al. showed fabrication of trench structures by imprint lithography and subsequent electrodeposition of copper on the trench structures.[246] Rahimi et al. also reported CO_2 laser-induced carbonization for trench formation of PI and then trapping of aqueous silver (Ag) ionic ink solutions into the carbonized regions.[247] However, these techniques not only use different numbers of processes and setups which make them complex and costly.

In recent years many cost-effective direct-writing and additive technologies particularly for their use in printed flexible electronics have been explored as alternative approaches to conventional clean-room processes with attractive features including reduced material wastage and scalable manufacturing.[105-107, 138, 248-251] Among the additive manufacturing techniques[85, 115, 251, 252], inkjet printing, aerosol-jet printing, screen-printing, and gravure printing are some examples of patterning processes that can be used for flexible electronics.[23, 123, 126, 191, 253-255] Solvents, additives, surfactants, and binders are mixed with pristine semiconducting, insulating, and metallic materials to enhance the printability of functional inks, hence the available printable ink formulations are far from ideal.[240] While designing an ink, several considerations are made, namely, reducing the coffee-ring effect, improving wetting on the surface while suppressing ink spreading, long-term ink stability, and compatibility with a given printing technique.[123] Another crucial aspect of printing processes that use ink is that the additional surfactant removal and

thermal annealing steps complicate the device manufacturing process.[151] Lastly, printing multifunctional materials (e.g., ferromagnetic, piezoelectric) and hybrid structures with current technologies is still challenging. Therefore, a new printing technique is needed to address the aforementioned challenges of current printed electronics technologies.[256]

In our previous works, we proposed a new concept of additive nanomanufacturing printer.[121, 179] This printer addressed some of the challenges of current printed electronics technique by producing pure, dry and solution-free nanoparticles, and also printing multifunctional materials such as titanium dioxide (TiO_2), indium tin oxide (ITO) and barium tin oxide (BTO) on different substrates such as metals, plastics, glass and ceramics.

Here, we developed a subtractive and additive nanomanufacturing technique (SANM) to easily form trench structures on PI substrates and subsequently filling and sintering the trench structures with the Ag nanoparticles. The present approach relies on firstly fabrication of trench patterns using laser etching process, followed by filling and laser sintering the trench patterns with the Ag nanoparticles. Filling and laser sintering the nanoparticles onto the trench structures of PI will result in increasing in the mechanical interlocking and interfacial region of the printed Ag nanoparticles and accordingly improving the reliability and fatigue of printed structures.

7.2 Results and Discussions

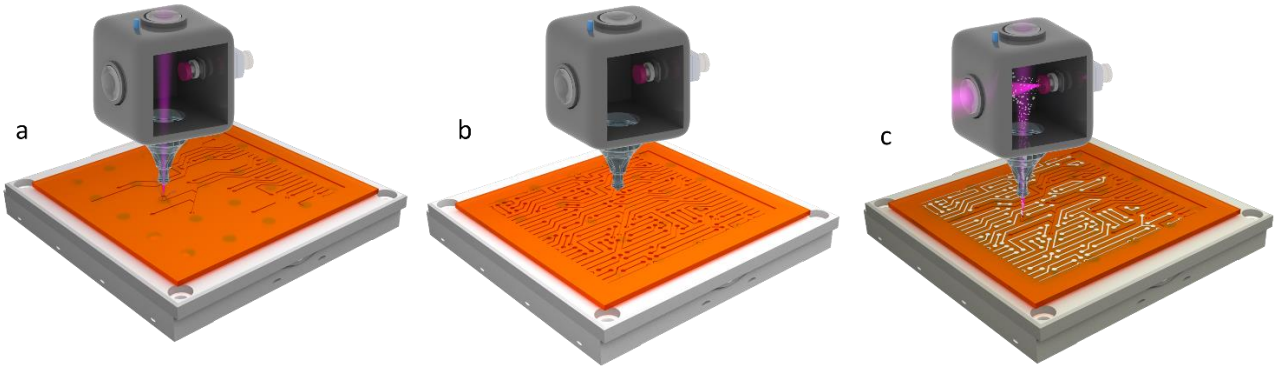

Figure 7.1 Schematic illustration of trench formation on PI substrate via 248nm laser etching process (**a**). Schematic illustration of completed trench pattern formed on the PI substrate (**b**). In-situ Ag nanoparticles generation, and laser sintering of the delivered Ag nanoparticles onto the pre-formed trench (**c**).

7.2.1 Subtractive Nanomanufacturing-Trench Formation

We have developed a system which is capable of simultaneously fabricating trenches on the PI substrates followed by filling these trenches with desired nanoparticles here Ag. **Figure 7.1** depicts the schematic illustration of the SANM printer. The SANM printer contains a microchamber, two vertical and horizontal 248nm laser beams, an Ag target, a nozzle, a XY positioning stage, and a gas flow system. The source of UV radiation was a coherent excimer laser with a pulse length of about 25 ns radiating at the KrF line (248nm).

For the trench formation, while the horizontal laser beam is blocked, the vertical laser beam passes through the microchamber and nozzle is hitting the surface of PI substrate. The schematic of trench formation process is demonstrated in **Figure 7.1a**. Absorption of the UV laser photons will result in direct bond breaking with a certain quantum yield. In general, the laser fluence must exceed a certain threshold value to cause an irreversible change in the PI surface and forms trench. This modification threshold fluence depends essentially on the material and the number of laser pulses applied to the same spot.

For deeper understanding the PI etching process, we investigated the influence of number of laser pulses, laser beam fluence, laser repetition rate and number of scanning path on the formation of trench onto the PI substrates. Flexible PI substrates (~127μm thick) bought from American Durafilm were used for all the experiments. The typical distance between the head of nozzle and surface of PI substrate kept ~ 0.5 mm constant during all experiments.

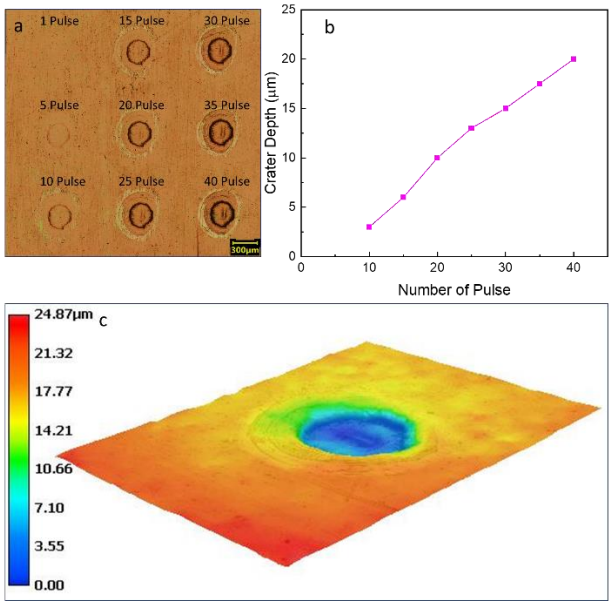

Figure 7.2. Laser ablated 300 µm diameter craters in PI substrate at different number of laser pulses (**a**). Depth of ablation plotted as a function of number of pulse (**b**). 3D view of ablated crater using 40 laser pulses (**c**). Laser fluence of ablation was 0.48 J cm^{-2}.

7.2.2 Influence of Laser Number of Pulses

The number of pulses N means the PI substrate is subjected to the laser irradiation N times. 1 to 40 number of pulses has been applied to the PI and the morphology of the PI surface was observed and measured with an optical microscope. **Figure 7.2a** shows the PI substrate subjected to 1 up to 40 laser pulses. As it is shown in **Figure 7.2a**, either the ablation does not start with the first pulse to around 5 pulses or the crater depth is too small to be measured. **Figure 7.2b** shows the measured ablation depth as a function of the number of pulses ranging from 1 to 40 pulses. A greater depth is observed for a higher number of pulses. **Figure 7.2c** shows 3D surface morphology of uniformly formed crater on the PI substrate irradiated with 248nm excimer laser fluence: 0.48 J cm^{-2} and 40 laser pulses.

7.2.3 Influence of Laser Fluence, Repetition Rate and Number of Scanning Path

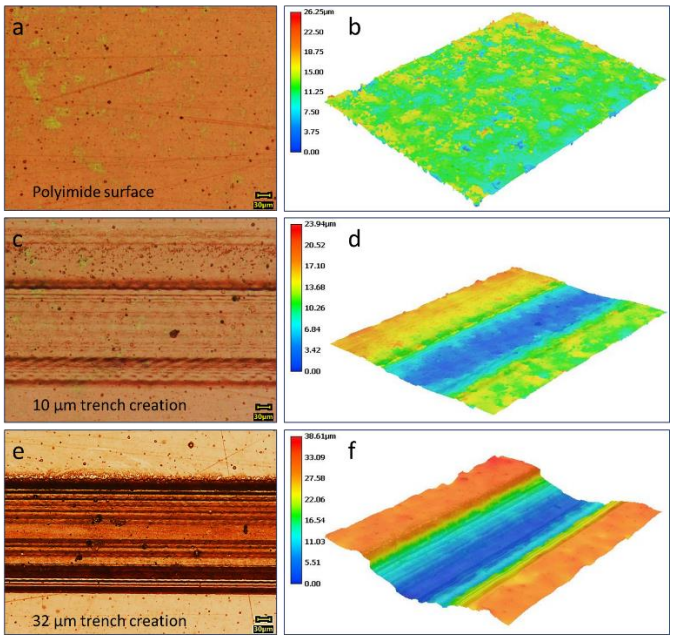

Figure 7.3. 2D (**a**) and 3D (**b**) optical image of PI surface. 2D and 3D view of 10 µm trench formed on PI substrate (**c**) and (**d**), respectively. 2D and 3D view of 32 µm trench formed on PI substrate (**e**) and (**f**), respectively.

For the trench formation, the XY position stage has to move according to desirable preprogrammed pattern. **Figure 7.3a**, **b** show the 2D and 3D view of flat PI substrate, respectively. As it is demonstrated in **Figure 7.3c**, **d**, 10 µm trench created while the laser fluence, number of scanning path, and repetition rate are 0.97 J cm^{-2}, 2 times, and 5 Hz, respectively. Employing 0.48 J cm^{-2} laser fluence, 10 Hz repetition rate, and 10 times repeating the scanning path, 32 µm trench formed onto the PI substrate, as it is shown **Figure 7.3e**, **f**. The nozzle diameter size, delay on each spot and the overlap were set to be 300 µm, 20 ms and 67% for these experiments, respectively.

Depth of trench as a function of number of scanning path for three different laser fluences, well above the ablation threshold (0.48, 0.71 and 0.97 J cm^{-2}), and four different repetition rates (5, 10, 15, 20 Hz) were investigated and the results have been plotted in **Figure 7.4a-d**.

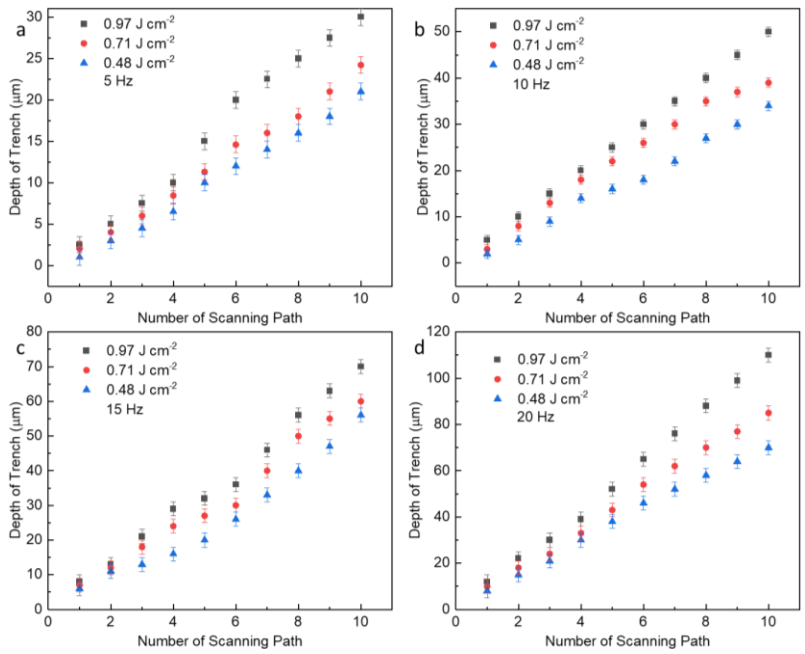

Figure 7.4. Depth of trench formed onto the PI substrate versus number of scanning path for three different laser fluences at four different repetition rates: 5 Hz (**a**), 10 Hz (**b**), 15 Hz (**c**) and 20 Hz (**d**).

Employing 5 Hz repetition rate, in the case of laser fluence 0.48 J cm^{-2}, the depth of trench increases from ~2 μm to ~20 μm as the number of scanning path increase from 1 to 10 times, while these changes are from ~3 μm to 25 μm, and ~3 μm to 30 μm for the laser fluence 0.71 J cm^{-2} and 0.97 J cm^{-2}, respectively. According to these experimental results shown in **Figure 7.4a-d**, higher laser fluence will result in deeper trench formation. In addition, the depth of trench has a proportional relationship with the laser repetition rate and number of scanning path, **Figure 7.4a-d**. Higher repetition rates form trench with bigger depth. For example, ~110 μm trench depth is formed for the case of 20 Hz repetition rate, 0.97 J cm^{-2} laser fluence and 10 times scanning path, as shown in **Figure 7.4d**. However, 10 Hz repetition rate, 0.97 J cm^{-2} laser fluence and 10 times scanning path will result in ~50 μm trench depth formation. As the number of scanning path increases, the depth of trench increases as well in all cases, **Figure 7.4a-d**.

7.2.4 Trench with Different Line Width

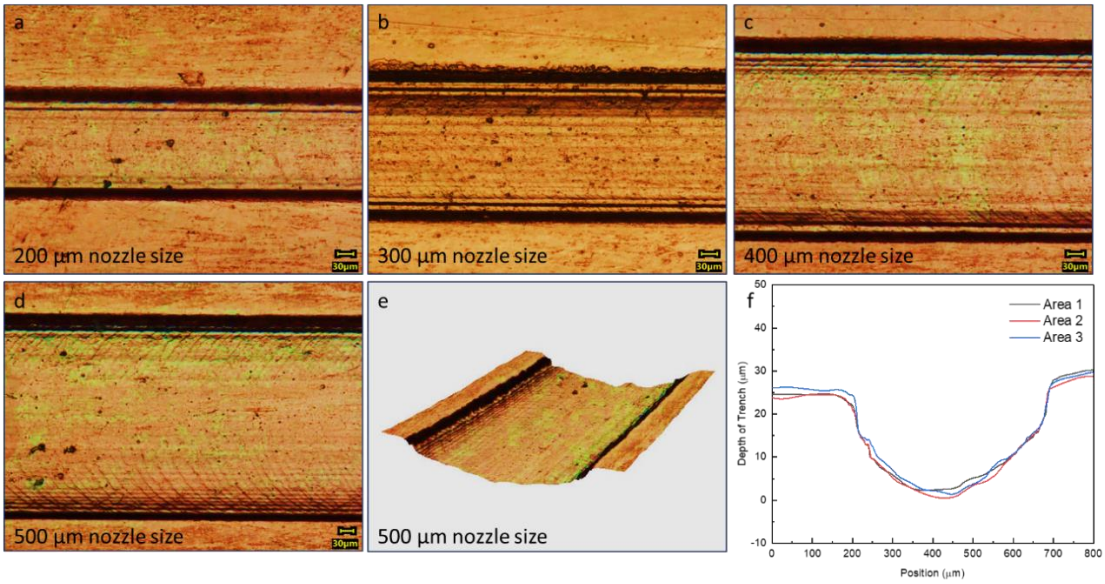

Figure 7.5. Optical images of trenches formed by laser ablation using different nozzle diameter sizes ranging from ~200 µm to ~500 µm (**a**) to (**d**). 3D view of created trench via nozzle diameter size 500 µm (**e**). Surface profile of ~500 µm trench (**f**).

Minimizing the feature size of trenches is another important issue. The sheet resistance is dependent on the line to width ratio of the printed structures. Trenches with different lines width can be achieved by employing nozzles with different diameter sizes. Considering the scanning delay of stage (20 ms), pulse repetition rate (10 Hz), laser fluence constant (0.97 J cm^{-2}) and number of scanning path (5 times), trenches with the width of ~200 µm to ~500 µm were fabricated using nozzle's diameter size ranging from 200 µm to 500 µm. The results are shown in **Figure 7.5a-d**. **Figure 7.5e** shows the surface morphology of 500 µm trench formed on PI substrate. Surface profile of ~500 µm trench shown in **Figure 7.5f** was measured at three different positions.

7.3 Additive Nanomanufacturing

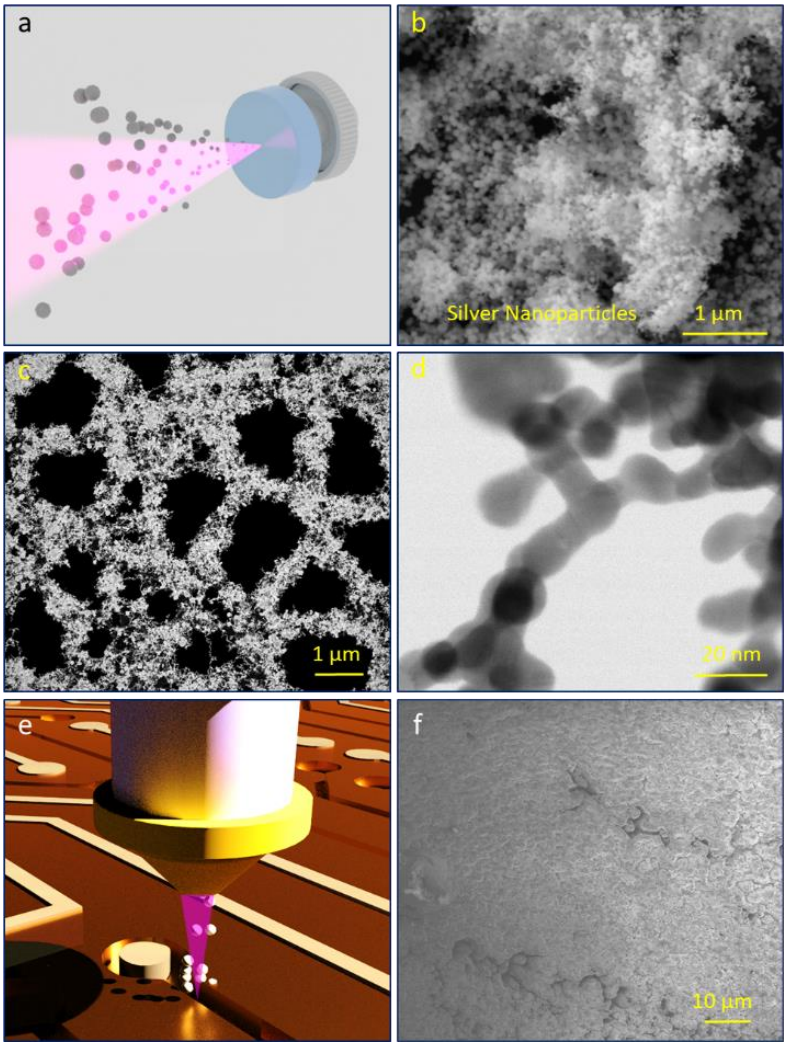

Figure 7.6. Schematic illustration of dry and pure Ag nanoparticles generated by laser ablation (**a**). SEM image of generated Ag nanoparticles (**b**). STEM image of ablated pure Ag nanoparticles (**c**). High-angle annular dark-field (HAADF) images of ablated pure Ag nanoparticles (**d**). Schematic illustration of laser sintering and printing the Ag nanoparticles onto the trench (**e**). SEM image of sintered nanoparticles onto the trench (**f**).

As shown in **Figure 7.6a**, when the horizontal laser beam hits the target of solid Ag, it turns the target into a plasma and will result in-situ and on-demand formation of stoichiometric nanoparticles, at room temperature and atmospheric pressure. **Figure 7.6b** shows the SEM image of generated Ag nanoparticles after hitting 0.2 J cm^{-2} laser beam to the Ag target. The morphology and size of the ablated Ag nanoparticles with ANM system was confirmed by STEM measurements. The STEM images of ablated Ag nanoparticles demonstrated in the

Figure 7.6c, d shows that the Ag nanoparticles are spherical-like and the average nanoparticle size is ~10 to 18 nm. The carrier gas such as argon flows and directs these in-situ generated Ag nanoparticles toward the nozzle head, and then nanoparticles are deposited and sintered by the ~ 0.1 J cm^{-2} vertical laser beam onto the trench formed on PI substrate, as shown in **Figure 7.6e**. SEM image shown in **Figure 7.6f** confirms sintering of the nanoparticles.

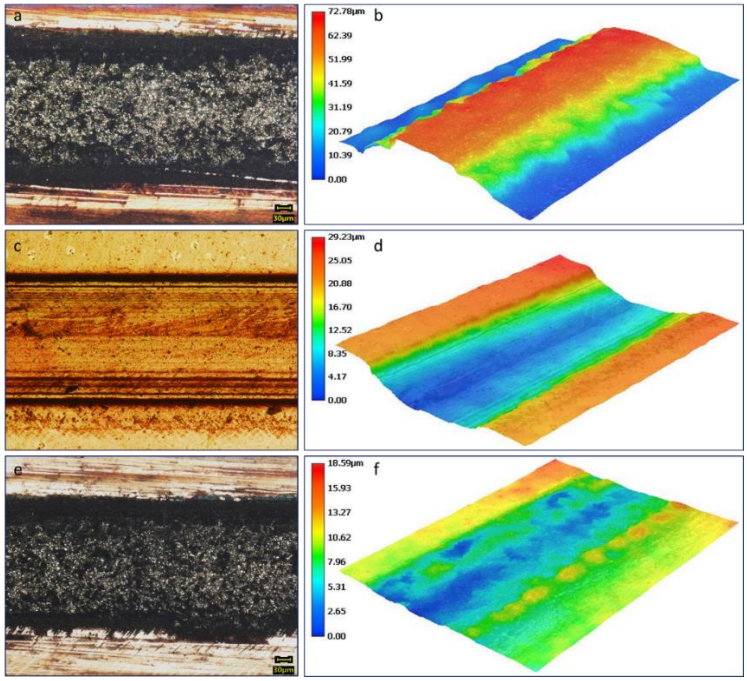

Figure 7.7. Optical image of printed Ag on the surface of PI substrate (**a**). Surface morphology of printed line on PI substrate with ~ 60 µm height (**b**). Optical image (**c**) and surface morphology (**d**) of ~20 µm trench formed on PI substrate. Optical image (**e**) and surface morphology (**f**) of laser sintered Ag nanoparticles embedded in the trench formed on PI substrate.

ANM printing of Ag conductive line on flat PI substrate without trench is shown in **Figure 7.7a**. 3D view of line demonstrated in **Figure 7.7b** shows the deposition of Ag line with ~ 60 µm height. We created a trench on a PI substrate, shown in **Figure 7.7c**, followed by filling and laser sintering the trench with Ag nanoparticles, as shown in **Figure 7.7e**. Surface morphology image in **Figure 7.7d** shows that the depth of formed trench is ~20 µm. Also, surface morphology in **Figure 7.7f** confirms filling and sintering the trench up to surface with Ag nanoparticles.

Thickness of printed Ag nanoparticles onto the trench is controllable with the number of printing pass.

7.4 Reliability Test

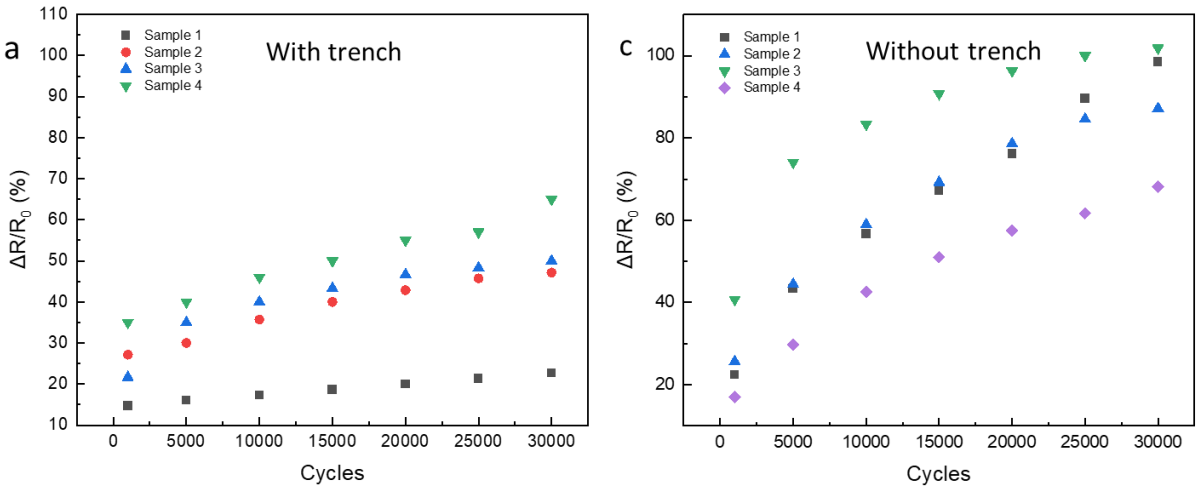

Figure 7.8. Cycling results of SANM printed Ag lines with (**a**) and without (**b**) trench onto PI substrates, respectively.

Special bending and stretching test setups were designed and fabricated. A set of 1 cm length Ag lines was printed on PI substrate with and without trench by SANM process. We studied and compared the bending reliability of these ANM printed lines. We measured changes in the resistance of the samples as they were bended at 16 mm bending radius from 1000 to 30,000 cycles. **Figure 7.8a** shows the variations in the electrical resistance of SANM printed Ag embedded into the trench as a function of different cycles. The resistance change ($\Delta R/R_0$) was expressed as follows:

$$\frac{\Delta R}{R_0} = \frac{R_s - R_0}{R_0}$$

where R_0 and R_s are initial and under-stress resistance, respectively. Same results are plotted in **Figure 7.8b** for the ANM printed Ag on flat PI substrate without trench formation. It can be seen from **Figure 7.8a**, **b** that the reliability of printed lines onto the trench improves drastically

compared to the lines printed on flat PI substrates. For instance, the resistance of the Ag lines embedded into trench increased around 20% to 60% after 30,000 bending cycles, while the printed Ag on flat PI increased around 70% to 100% after 30,000 bending cycles. Therefore, the Ag nanoparticles embedded into the trench of substrate may show a stronger adhesion as compared to the printed Ag on the flat PI substrate. This adhesion effect is not only because of a mechanical interlocking effect of the Ag nanoparticles printed at the interfacial region, but also increasing of the interfacial region. The other plausible explanation is that most likely the delamination or crack occurs faster in printed Ag on flat PI substrate. In the case of printing into the trench, it is more likely that the delamination or crack occurs at lower speed which results in improvement of reliability of lines.

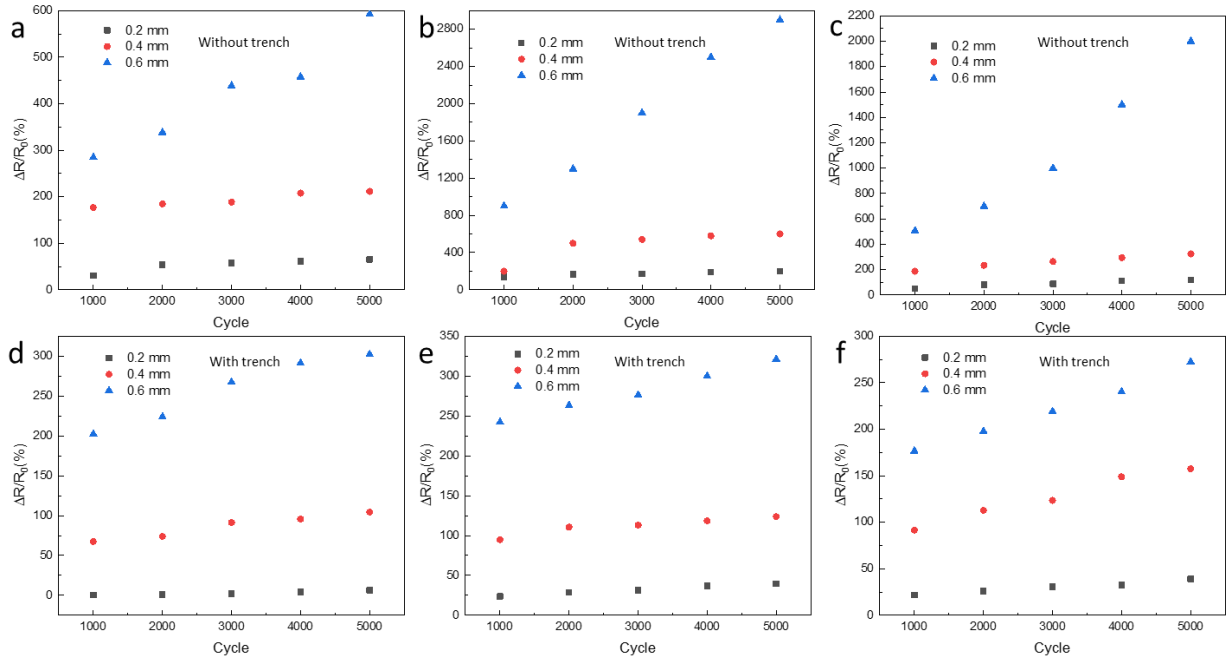

Figure 7.9. Normalized change of resistance-cycle curves in response to 0.2 to 0.6 mm displacement for the ANM printed Ag on flat PI substrates for 3 different samples (**a**, **b**, **c**). Graphs of stretching test for 0.2 to 0.6 mm displacement on ANM printed Ag onto trench (**d**, **e**, **f**).

Sets of 1 cm length Ag lines printed on 50 mm×5 mm×0.127 mm PI substrate, with and without trench. We measured the normalized change in the resistance as a function of the cycle for the 1000^{th}, 2000^{th}, 3000^{th}, 4000^{th}, and 5000^{th} cycles while the substrates are exposed to stretching force. **Figure 7.9a-c** shows the stretching results for the ANM printed Ag on flat PI substrates for different samples. We observed the variation in the resistance up to 200% in response to 0.2 mm stretching displacement and up to 2800% in response to 0.6 mm stretching displacement after 5000 cycles. The stretching results for printed Ag onto the trench is demonstrated in **Figure 7.9d-e**. The change in resistance after 5000 cycles is up to ~50% and ~300% at 0.2 and 0.6 mm stretching displacement, respectively. Comparing these results to those of the printed on flat PI confirms that high flexibility can be reached in the case of printing samples onto trench formed on PI substrates.

7.5 Conclusion

We demonstrated subtractive nanomanufacturing of trenches into the polyimide substrates followed by additive nanomanufacturing of Ag nanoparticles onto the formed trenches, all using one proposed setup. This setup consists of a nozzle, a rotating target and a gas flow system, all connected to a microchamber. The microchamber has two windows for passing the 248nm laser beams. The laser beam, passed through the nozzle, is used for polyimide ablation to form trenches with feature sizes ranging from ~200 µm to 500 µm. Laser-Ag target interaction is resulting in producing dry and pure Ag nanoparticles which are then delivered into the polyimide trenches via the carrier gas flow, followed by laser sintering the nanoparticles onto the trenches. We showed printed Ag nanoparticles onto the trenches formed on polyimide has higher mechanical interlocking and interfacial region compared to printed Ag nanoparticles on flat polyimide. As a result, the bending and stretching tests showed better reliability performance in

case of printing onto the trenches. The subtractive and additive nanomanufacturing printing technique suggests new potentials for applications in sensors, antenna, smart electronics, medicals and other applications.

Methods

Scanning Electron Microscopy images were obtained using Zeiss Crossbeam 550 microscope. The voltage and current were 5 KV and 2 nA, respectively.

KEYENCE VHX-6000 series microscope was used to measure the depth of trenches.

Temperature sensor: the Texas instruments CC2541 Bluetooth 4.0 module is attached to the AT-Tiny using Tx and Rx for serial transfer of resistance values. Both Bluetooth board and MCU are powered using a 3.7v battery (LIR-2032). Data is transmitted to an external device wirelessly (Serial Bluetooth Terminal application on phone or any similar application of PC) using Bluetooth signals and is visible in form of a plot/raw values. The raw values can either be logged on the external device or in real time be plotted to see the change in temperature with respect to time. The printed temperature sensor circuit measures values of resistance at the sensor location which is measured via AT-Tiny 85 (as a MCU) at a capture rate of 2 Hz+.

CHAPTER 08

CONCLUSION

Currently, printed electronics are manufactured by wet printing technologies such as inkjet and aerosol jet printers, which suffer from major drawbacks, including complex and expensive ink formulations, surfactants/contaminants, limited sources of inks, and the need for high-temperature post-processing. This dissertation presented a novel additive nanomanufacturing and dry printing technology for multimaterial printing of electronics, sensors, and energy devices.

First, we showed a new laser-based crystallization technique to print 2D materials on PDMS flexible substrate. This technique is capable of crystallizing the amorphous 2D materials deposited by pulsed laser deposition technique on PDMS. However, the need for lithography and transferring of sample for different process steps made this technique not the ideal for the future of printed electronics. Later, we introduced a dry and ink-free additive nanomanufacturing technique (ANM) to print multifunctional materials on rigid and flexible substrates. Using the ANM technique, silver-based flexible hybrid electronics and sensors printed, and their electrical and mechanical features were characterized. Multimaterial printing had been introduced to confirm the capability of the ANM printer. Lastly, as a cheap replacement of silver, copper printed on polyimide substrate via ANM printer. The dry nature, printing flexibility, purity, mechanical reliability, and device performance characteristics would bring excitement into the field of printing functional structures devices for future printed flexible electronics and sensors.

8.1 Additive Nanomanufactuirng of Multifunctional Materials

A new printing concept for additive nanomanufacturing (ANM) of multifunctional material and structures on various substrates had been demonstrated. In this method, a stream of pure nanoparticles can be laser-generated in real-time at room temperature and at atmospheric

pressure. These nanoparticles are then directed toward a printer nozzle and laser-sintered in-situ to form crystals with desired patterns and structures. Various functional materials (TiO_2, BTO, ITO) had been printed on different substrates, including SiO_2, PDMS, and paper. The remarkable ability of the ANM system is the ability to print any arbitrary patterns of sintered nanoparticles on the substrates realized by the programmable motion of the X–Y stage during the printing process.

8.2 Additive Nanomanufactuirng of Silver and Copper

Printed flexible electronics deposit various materials, such as silver and copper, onto a substrate to create electronic devices and sensors. These materials can be used to create conductive traces, antennas, interdigital electronics and flexible hybrid electronics. The use of Ag and Cu in printed electronics is attractive due to their high conductivity and low cost. Utilization the ANM technology, process parameters for printing of Ag and Cu has been developed, and the electrical and mechanical behavior has been characterized. The mechanical behavior of the ANM-printed Ag and Cu lines on polyimide substrates under bending and cycling at different bending radii is studied and the results showed that ANM-printed Ag and Cu lines have nearly no change in resistivity even after high bending cycles. These tests validated its good electrical conductivity and functionality of the printed devices under different strain which makes the ANM as a potential technique for printing flexible electronics and devices.

8.3 Multimaterial Additive Nanomanufacturing

A multimaterial additive nanomanufacturing (M-ANM) technique was demonstrated, allowing the printing of lateral and vertical hybrid structures and devices. This M-ANM technique involves pulsed laser ablation of solid targets placed on a target carousel inside the printer head for in-situ generation of contamination-free nanoparticles, which are then guided via a carrier gas

toward the nozzle and onto the surface of the substrate, where they are sintered and printed in real-time by a second laser. The target carousel is rotated so as to bring a particular target in engagement with the ablation laser beam in predetermined sequences to print multiple materials, including metals, semiconductors, and insulators, in a single process step. Various multimaterial devices such as photodetector composed of Ag/ZnO and flexible hybrid electronic circuit with Ag/Al_2O_3 interconnects are printed and characterized.

FUTURE WORKS

The additive nanomanufacturing (ANM) printer and technology has opened a new area of printed electronics and it has the capability to compete with currently commercialized printed electronics technologies such as inkjet and aerosol jet printers. As a new developed technique, ANM has a huge potential for future studies and researches. Additionally, ANM has enables some features not possible with other techniques. The following has been discussed the future work that can be done with ANM printer.

1. Solder printing: IJP and AJP are not capable of printing solder materials. The unique feature of ANM can be utilized for printing solder materials. Printing electronic circuits and solder simultaneously can reduce the manufacturing cost, and also eliminates the challenges of reflow soldering.
2. Gas study: Different gasses can be used in the ANM printer not only as the career gas, but also to make a new phase of materials while sintered. For instance, O_2 and CH_4 can be employed in ANM.
3. High temperature applications: The ANM printer can be used for printing new materials such as Ni or Nb on ceramics substrates for high temperature applications.

References

[1] M. Rafiee, R.D. Farahani, D. Therriault, Multi-Material 3D and 4D Printing: A Survey, Advanced Science 7(12) (2020).
[2] M. Gao, L. Li, Y. Song, Inkjet printing wearable electronic devices, Journal of Materials Chemistry C 5(12) (2017) 2971-2993.
[3] A. Boumegnane, A. Nadi, O. Cherkaoui, M. Tahiri, Inkjet printing of silver conductive ink on textiles for wearable electronic applications, Materials Today: Proceedings 58 (2022) 1235-1241.
[4] A. Ahmed, S. Sharma, B. Adak, M.M. Hossain, A.M. LaChance, S. Mukhopadhyay, L. Sun, Two-dimensional MXenes

: New frontier of wearable and flexible electronics, InfoMat 4(4) (2022).
[5] Y. Zhu, J. Qin, G. Shi, C. Sun, M. Ingram, S. Qian, J. Lu, S. Zhang, Y.L. Zhong, A focus review on 3D printing of wearable energy storage devices, Carbon Energy 4(6) (2022) 1242-1261.
[6] X. Gong, K. Huang, Y.-H. Wu, X.-S. Zhang, Recent progress on screen-printed flexible sensors for human health monitoring, Sensors and Actuators A: Physical 345 (2022).
[7] S. Li, Y. Zhang, X. Liang, H. Wang, H. Lu, M. Zhu, H. Wang, M. Zhang, X. Qiu, Y. Song, Y. Zhang, Humidity-sensitive chemoelectric flexible sensors based on metal-air redox reaction for health management, Nature Communications 13(1) (2022).
[8] M. Pietsch, S. Schlisske, M. Held, P. Maag, G. Hernandez-Sosa, Stretchable inkjet-printed electronics on mechanically compliant island-bridge architectures covalently bonded to elastomeric substrates, Flexible and Printed Electronics 7(2) (2022).
[9] M.A. Butt, N.L. Kazanskiy, S.N. Khonina, Revolution in Flexible Wearable Electronics for Temperature and Pressure Monitoring—A Review, Electronics 11(5) (2022).
[10] T.B. Carmichael, R. Österbacka, Flexible and printed electronics: a transition in leadership—reflecting on our successes and looking forward to the future, Flexible and Printed Electronics 7(1) (2022).
[11] C.H. Rao, K. Avinash, B.K.S.V.L. Varaprasad, S. Goel, A Review on Printed Electronics with Digital 3D Printing: Fabrication Techniques, Materials, Challenges and Future Opportunities, Journal of Electronic Materials 51(6) (2022) 2747-2765.
[12] E. Jansson, J. Lyytikäinen, P. Tanninen, K. Eiroma, V. Leminen, K. Immonen, L. Hakola, Suitability of Paper-Based Substrates for Printed Electronics, Materials 15(3) (2022).
[13] Z. Li, S. Chang, S. Khuje, S. Ren, Recent Advancement of Emerging Nano Copper-Based Printable Flexible Hybrid Electronics, ACS Nano 15(4) (2021) 6211-6232.
[14] M. Stoppa, A. Chiolerio, Wearable Electronics and Smart Textiles: A Critical Review, Sensors 14(7) (2014) 11957-11992.
[15] L.J. Deiner, T.L. Reitz, Inkjet and Aerosol Jet Printing of Electrochemical Devices for Energy Conversion and Storage Advanced Engineering Materials 19(7) (2017).
[16] M.A. Shah, D.-G. Lee, B.-Y. Lee, S. Hur, Classifications and Applications of Inkjet Printing Technology: A Review, IEEE Access 9 (2021) 140079-140102.
[17] V. Beedasy, P.J. Smith, Printed Electronics as Prepared by Inkjet Printing, Materials 13(3) (2020).
[18] X. Wang, M. Zhang, L. Zhang, J. Xu, X. Xiao, X. Zhang, Inkjet-printed flexible sensors: From function materials, manufacture process, and applications perspective, Materials Today Communications 31 (2022).

[19] N.J. Wilkinson, M.A.A. Smith, R.W. Kay, R.A. Harris, A review of aerosol jet printing—a non-traditional hybrid process for micro-manufacturing, The International Journal of Advanced Manufacturing Technology 105(11) (2019) 4599-4619.
[20] M. Borghetti, E. Cantu, A. Ponzoni, E. Sardini, M. Serpelloni, Aerosol Jet Printed and Photonic Cured Paper-Based Ammonia Sensor for Food Smart Packaging, IEEE Transactions on Instrumentation and Measurement 71 (2022) 1-10.
[21] X. Zeng, P. He, M. Hu, W. Zhao, H. Chen, L. Liu, J. Sun, J. Yang, Copper inks for printed electronics: a review, Nanoscale 14(43) (2022) 16003-16032.
[22] M.E.H. Bhuiyan, A. Behroozfar, S. Daryadel, S. Moreno, S. Morsali, M. Minary-Jolandan, A Hybrid Process for Printing Pure and High Conductivity Nanocrystalline Copper and Nickel on Flexible Polymeric Substrates, Scientific Reports 9(1) (2019).
[23] L. Nayak, S. Mohanty, S.K. Nayak, A. Ramadoss, A review on inkjet printing of nanoparticle inks for flexible electronics, Journal of Materials Chemistry C 7(29) (2019) 8771-8795.
[24] M. Singh, H.M. Haverinen, P. Dhagat, G.E. Jabbour, Inkjet Printing—Process and Its Applications, Advanced Materials 22(6) (2010) 673-685.
[25] Y. Khan, A. Thielens, S. Muin, J. Ting, C. Baumbauer, A.C. Arias, A New Frontier of Printed Electronics: Flexible Hybrid Electronics, Advanced Materials 32(15) (2020) 1905279.
[26] H. Li, J. Liang, Recent Development of Printed Micro-Supercapacitors: Printable Materials, Printing Technologies, and Perspectives, Advanced Materials 32(3) (2020) 1805864.
[27] Z. Zhan, J. An, Y. Wei, V.T. Tran, H. Du, Inkjet-printed optoelectronics, Nanoscale 9(3) (2017) 965-993.
[28] S. Lu, J.A. Cardenas, R. Worsley, N.X. Williams, J.B. Andrews, C. Casiraghi, A.D. Franklin, Flexible, Print-in-Place 1D–2D Thin-Film Transistors Using Aerosol Jet Printing, ACS Nano 13(10) (2019) 11263-11272.
[29] Y. Chu, C. Qian, P. Chahal, C. Cao, Printed Diodes: Materials Processing, Fabrication, and Applications, Advanced Science 6(6) (2019) 1801653.
[30] C. Zhang, L. McKeon, M.P. Kremer, S.-H. Park, O. Ronan, A. Seral-Ascaso, S. Barwich, C.Ó. Coileáin, N. McEvoy, H.C. Nerl, B. Anasori, J.N. Coleman, Y. Gogotsi, V. Nicolosi, Additive-free MXene inks and direct printing of micro-supercapacitors, Nature Communications 10(1) (2019) 1795.
[31] M. Rafiee, R.D. Farahani, D. Therriault, Multi-Material 3D and 4D Printing: A Survey, Advanced Science 7(12) (2020) 1902307.
[32] D.W. Yee, M.L. Lifson, B.W. Edwards, J.R. Greer, Additive Manufacturing of 3D-Architected Multifunctional Metal Oxides, Advanced Materials 31(33) (2019) 1901345.
[33] M. Alssabbagh, A.A. Tajuddin, M. Abdulmanap, R. Zainon, Evaluation of 3D printing materials for fabrication of a novel multi-functional 3D thyroid phantom for medical dosimetry and image quality, Radiation Physics and Chemistry 135 (2017) 106-112.
[34] S. Bodkhe, P. Ermanni, 3D printing of multifunctional materials for sensing and actuation: Merging piezoelectricity with shape memory, European Polymer Journal 132 (2020) 109738.
[35] A. Nadernezhad, N. Khani, G.A. Skvortsov, B. Toprakhisar, E. Bakirci, Y. Menceloglu, S. Unal, B. Koc, Multifunctional 3D printing of heterogeneous hydrogel structures, Scientific Reports 6(1) (2016) 33178.
[36] R. Gheisari, H. Chamberlain, G. Chi-Tangyie, S. Zhang, A. Goulas, C.-K. Lee, T. Whittaker, D. Wang, A. Ketharam, A. Ghosh, B. Vaidhyanathan, W. Whittow, D. Cadman, Y.C. Vardaxoglou, I.M. Reaney, D.S. Engstrøm, Multi-material additive manufacturing of low

sintering temperature Bi2Mo2O9 ceramics with Ag floating electrodes by selective laser burnout, Virtual and Physical Prototyping 15(2) (2020) 133-147.
[37] E.B. Joyee, Y. Pan, Additive manufacturing of multi-material soft robot for on-demand drug delivery applications, Journal of Manufacturing Processes 56 (2020) 1178-1184.
[38] D. Han, H. Lee, Recent advances in multi-material additive manufacturing: methods and applications, Current Opinion in Chemical Engineering 28 (2020) 158-166.
[39] V.G. Rocha, E. Saiz, I.S. Tirichenko, E. García-Tuñón, Direct ink writing advances in multi-material structures for a sustainable future, Journal of Materials Chemistry A 8(31) (2020) 15646-15657.
[40] R.D. Farahani, M. Dubé, D. Therriault, Three-Dimensional Printing of Multifunctional Nanocomposites: Manufacturing Techniques and Applications, Advanced Materials 28(28) (2016) 5794-5821.
[41] N. Mohandas, Y.J. Loke, L. Mackenzie, C. Bennett, S.F. Berkovic, J.M. Craig, L. Vadlamudi, Deciphering the role of epigenetics in self-limited epilepsy with centrotemporal spikes, Epilepsy Res 156 (2019).
[42] Z.N. Bao, X.D. Chen, Flexible and Stretchable Devices, Adv Mater 28(22) (2016) 4177-4179.
[43] J.D. Cain, E.D. Hanson, F.Y. Shi, V.P. Dravid, Emerging opportunities in the two-dimensional chalcogenide systems and architecture, Curr Opin Solid St M 20(6) (2016) 374-387.
[44] K.S. Novoselov, A.K. Geim, S.V. Morozov, D. Jiang, Y. Zhang, S.V. Dubonos, I.V. Grigorieva, A.A. Firsov, Electric field effect in atomically thin carbon films, Science 306(5696) (2004) 666-669.
[45] D. Akinwande, N. Petrone, J. Hone, Two-dimensional flexible nanoelectronics, Nat Commun 5 (2014).
[46] A. Bolotsky, D. Butler, C.Y. Dong, K. Gerace, N.R. Glayin, C. Muratore, J.A. Robinson, A. Ebrahimi, Two-Dimensional Materials in Biosensing and Healthcare: From In Vitro Diagnostics to Optogenetics and Beyond, Acs Nano 13(9) (2019) 9781-9810.
[47] R.H. Kim, J. Leem, C. Muratore, S. Nam, R. Rao, A. Jawaid, M. Durstock, M. McConney, L. Drummy, R. Rai, A. Voevodin, N. Glavin, Photonic crystallization of two-dimensional MoS2 for stretchable photodetectors, Nanoscale 11(28) (2019) 13260-13268.
[48] C. Muratore, A.A. Voevodin, N.R. Glavin, Physical vapor deposition of 2D Van der Waals materials: a review, Thin Solid Films 688 (2019).
[49] B. Sirota, N. Glavin, A.A. Voevodin, Room temperature magnetron sputtering and laser annealing of ultrathin MoS2 for flexible transistors, Vacuum 160 (2019) 133-138.
[50] H. Fang, S. Chuang, T.C. Chang, K. Takei, T. Takahashi, A. Javey, High-Performance Single Layered WSe2 p-FETs with Chemically Doped Contacts, Nano Lett 12(7) (2012) 3788-3792.
[51] G.H. Lee, Y.J. Yu, X. Cui, N. Petrone, C.H. Lee, M.S. Choi, D.Y. Lee, C. Lee, W.J. Yoo, K. Watanabe, T. Taniguchi, C. Nuckolls, P. Kim, J. Hone, Flexible and Transparent MoS2 Field-Effect Transistors on Hexagonal Boron Nitride-Graphene Heterostructures, Acs Nano 7(9) (2013) 7931-7936.
[52] I. Meric, C.R. Dean, N. Petrone, L. Wang, J. Hone, P. Kim, K.L. Shepard, Graphene Field-Effect Transistors Based on Boron-Nitride Dielectrics, P Ieee 101(7) (2013) 1609-1619.
[53] E. Bosman, G. Van Steenberge, B. Van Hoe, J. Missinne, J. Vanfleteren, P. Van Daele, Highly Reliable Flexible Active Optical Links, Ieee Photonic Tech L 22(5) (2010) 287-289.

[54] C.C. Choi, L. Lin, Y.J. Liu, J.H. Choi, L. Wang, D. Haas, J. Magera, R.T. Chen, Flexible optical waveguide film fabrications and optoelectronic devices integration for fully embedded board-level optical interconnects, J Lightwave Technol 22(9) (2004) 2168-2176.
[55] R. Dangel, F. Horst, D. Jubin, N. Meier, J. Weiss, B.J. Offrein, B.W. Swatowski, C.M. Amb, D.J. DeShazer, W.K. Weidner, Development of Versatile Polymer Waveguide Flex Technology for Use in Optical Interconnects, J Lightwave Technol 31(24) (2013) 3915-3926.
[56] L. Li, Y. Zou, H.T. Lin, J.J. Hu, X.C. Sun, N.N. Feng, S. Danto, K. Richardson, T. Gu, M. Haney, A Fully-Integrated Flexible Photonic Platform for Chip-to-Chip Optical Interconnects, J Lightwave Technol 31(24) (2013) 4080-4086.
[57] Y. Chen, H. Li, M. Li, Flexible and tunable silicon photonic circuits on plastic substrates, Sci Rep-Uk 2 (2012).
[58] L. Zhu, J. Kapraun, J. Ferrara, C.J. Chang-Hasnain, Flexible photonic metastructures for tunable coloration, Optica 2(3) (2015) 255-258.
[59] Y. Zou, L. Moreel, H.T. Lin, J. Zhou, L. Li, S. Danto, J.D. Musgraves, E. Koontz, K. Richardson, K.D. Dobson, R. Birkmire, J.J. Hu, Solution Processing and Resist-Free Nanoimprint Fabrication of Thin Film Chalcogenide Glass Devices: Inorganic-Organic Hybrid Photonic Integration, Adv Opt Mater 2(8) (2014) 759-764.
[60] L. Gao, Y.H. Zhang, V. Malyarchuk, L. Jia, K.I. Jang, R.C. Webb, H.R. Fu, Y. Shi, G.Y. Zhou, L.K. Shi, D. Shah, X. Huang, B.X. Xu, C.J. Yu, Y.G. Huang, J.A. Rogers, Epidermal photonic devices for quantitative imaging of temperature and thermal transport characteristics of the skin, Nat Commun 5 (2014).
[61] L. Fan, L.T. Varghese, Y. Xuan, J. Wang, B. Niu, M.H. Qi, Direct fabrication of silicon photonic devices on a flexible platform and its application for strain sensing, Opt Express 20(18) (2012) 20564-20575.
[62] S.M. Kamali, A. Arbabi, E. Arbabi, Y. Horie, A. Faraon, Decoupling optical function and geometrical form using conformal flexible dielectric metasurfaces, Nat Commun 7 (2016).
[63] W.D. Zhou, Z.Q. Ma, Breakthroughs in Photonics 2012: Breakthroughs in Nanomembranes and Nanomembrane Lasers, Ieee Photonics J 5(2) (2013).
[64] W. Cao, J. Wang, M. Ma, Exfoliation of Two-Dimensional Materials: The Role of Entropy, J Phys Chem Lett 10(5) (2019) 981-986.
[65] J.N. Coleman, M. Lotya, A. O'Neill, S.D. Bergin, P.J. King, U. Khan, K. Young, A. Gaucher, S. De, R.J. Smith, I.V. Shvets, S.K. Arora, G. Stanton, H.Y. Kim, K. Lee, G.T. Kim, G.S. Duesberg, T. Hallam, J.J. Boland, J.J. Wang, J.F. Donegan, J.C. Grunlan, G. Moriarty, A. Shmeliov, R.J. Nicholls, J.M. Perkins, E.M. Grieveson, K. Theuwissen, D.W. McComb, P.D. Nellist, V. Nicolosi, Two-Dimensional Nanosheets Produced by Liquid Exfoliation of Layered Materials, Science 331(6017) (2011) 568-571.
[66] L.Y. Niu, K. Li, H.Y. Zhen, Y.S. Chui, W.J. Zhang, F. Yan, Z.J. Zheng, Salt-Assisted High-Throughput Synthesis of Single- and Few-Layer Transition Metal Dichalcogenides and Their Application in Organic Solar Cells, Small 10(22) (2014) 4651-4657.
[67] R.J. Smith, P.J. King, M. Lotya, C. Wirtz, U. Khan, S. De, A. O'Neill, G.S. Duesberg, J.C. Grunlan, G. Moriarty, J. Chen, J.Z. Wang, A.I. Minett, V. Nicolosi, J.N. Coleman, Large-Scale Exfoliation of Inorganic Layered Compounds in Aqueous Surfactant Solutions, Adv Mater 23(34) (2011) 3944-+.
[68] J.X. Yu, J. Li, W.F. Zhang, H.X. Chang, Synthesis of high quality two-dimensional materials via chemical vapor deposition, Chem Sci 6(12) (2015) 6705-6716.

[69] J.D. Zhou, J.H. Lin, X.W. Huang, Y. Zhou, Y. Chen, J. Xia, H. Wang, Y. Xie, H.M. Yu, J.C. Lei, D. Wu, F.C. Liu, Q.D. Fu, Q.S. Zeng, C.H. Hsu, C.L. Yang, L. Lu, T. Yu, Z.X. Shen, H. Lin, B.I. Yakobson, Q. Liu, K. Suenaga, G.T. Liu, Z. Liu, A library of atomically thin metal chalcogenides, Nature 556(7701) (2018) 355-+.
[70] N. Azam, Z. Ahmadi, B. Yakupoglu, S. Elafandi, M.K. Tian, A. Boulesbaa, M. Mahjouri-Samani, Accelerated synthesis of atomically-thin 2D quantum materials by a novel laser-assisted synthesis technique, 2d Mater 7(1) (2020).
[71] Z. Ahmadi, B. Yakupoglu, N. Azam, S. Elafandi, M. Mahjouri-Samani, Application of lasers in the synthesis and processing of two-dimensional quantum materials, J Laser Appl 31(3) (2019).
[72] M.E. McConney, N.R. Glavin, A.T. Juhl, M.H. Check, M.F. Durstock, A.A. Voevodin, T.E. Shelton, J.E. Bultman, J. Hu, M.L. Jespersen, M.K. Gupta, R.D. Naguy, J.G. Colborn, A. Haque, P.T. Hagerty, R.E. Stevenson, C. Muratore, Direct synthesis of ultra-thin large area transition metal dichalcogenides and their heterostructures on stretchable polymer surfaces (vol 31, pg 967, 2016), J Mater Res 31(7) (2016) 975-975.
[73] I. Song, C. Park, M. Hong, J. Baik, H.-J. Shin, H.C. Choi, Patternable Large-Scale Molybdenium Disulfide Atomic Layers Grown by Gold-Assisted Chemical Vapor Deposition, Angewandte Chemie International Edition 53(5) (2014) 1266-1269.
[74] R.F. Hossain, I.G. Deaguero, T. Boland, A.B. Kaul, Biocompatible, large-format, inkjet printed heterostructure MoS2-graphene photodetectors on conformable substrates, npj 2D Materials and Applications 1(1) (2017).
[75] L. Huang, Y. Huang, J. Liang, X. Wan, Y. Chen, Graphene-based conducting inks for direct inkjet printing of flexible conductive patterns and their applications in electric circuits and chemical sensors, Nano Research 4(7) (2011) 675-684.
[76] Z. Ahmadi, B. Yakupoglu, N. Azam, S. Elafandi, M. Mahjouri-Samani, Self-limiting laser crystallization and direct writing of 2D materials, International Journal of Extreme Manufacturing 1(1) (2019).
[77] J. Jiang, A novel fabrication strategy for additive manufacturing processes, Journal of Cleaner Production 272 (2020) 122916.
[78] N. Li, S. Huang, G. Zhang, R. Qin, W. Liu, H. Xiong, G. Shi, J. Blackburn, Progress in additive manufacturing on new materials: A review, Journal of Materials Science & Technology 35(2) (2019) 242-269.
[79] W.E. Frazier, Metal Additive Manufacturing: A Review, Journal of Materials Engineering and Performance 23(6) (2014) 1917-1928.
[80] T.D. Ngo, A. Kashani, G. Imbalzano, K.T.Q. Nguyen, D. Hui, Additive manufacturing (3D printing): A review of materials, methods, applications and challenges, Composites Part B: Engineering 143 (2018) 172-196.
[81] J. Kranz, D. Herzog, C. Emmelmann, Design guidelines for laser additive manufacturing of lightweight structures in TiAl6V4, Journal of Laser Applications 27(S1) (2014) S14001.
[82] R. Russell, D. Wells, J. Waller, B. Poorganji, E. Ott, T. Nakagawa, H. Sandoval, N. Shamsaei, M. Seifi, 3 - Qualification and certification of metal additive manufactured hardware for aerospace applications**Disclaimer: The views presented in this paper are those of the authors and should not be construed as representing official rules interpretation or policy of ASTM International, General Electric (GE), Lockheed Martin Corporation (LMCO), National Aeronautics and Space Agency (NASA), Japanese Space and Exploration Agency (JAXA), or

the Federal Aviation Administration (FAA), in: F. Froes, R. Boyer (Eds.), Additive Manufacturing for the Aerospace Industry, Elsevier2019, pp. 33-66.
[83] K.S. Prakash, T. Nancharaih, V.V.S. Rao, Additive Manufacturing Techniques in Manufacturing -An Overview, Materials Today: Proceedings 5(2, Part 1) (2018) 3873-3882.
[84] S. Lee, Z. Ahmadi, J.W. Pegues, M. Mahjouri-Samani, N. Shamsaei, Laser polishing for improving fatigue performance of additive manufactured Ti-6Al-4V parts, Optics & Laser Technology 134 (2021) 106639.
[85] S.M. Thompson, L. Bian, N. Shamsaei, A. Yadollahi, An overview of Direct Laser Deposition for additive manufacturing; Part I: Transport phenomena, modeling and diagnostics, Additive Manufacturing 8 (2015) 36-62.
[86] B. Kumar, B.K. Kaushik, Y.S. Negi, Organic Thin Film Transistors: Structures, Models, Materials, Fabrication, and Applications: A Review, Polymer Reviews 54(1) (2014) 33-111.
[87] M.-s. Hwang, B.-y. Jeong, J. Moon, S.-K. Chun, J. Kim, Inkjet-printing of indium tin oxide (ITO) films for transparent conducting electrodes, Materials Science and Engineering: B 176(14) (2011) 1128-1131.
[88] S.K. Karunakaran, G.M. Arumugam, W. Yang, S. Ge, S.N. Khan, X. Lin, G. Yang, Recent progress in inkjet-printed solar cells, Journal of Materials Chemistry A 7(23) (2019) 13873-13902.
[89] H.-R. Lim, H.S. Kim, R. Qazi, Y.-T. Kwon, J.-W. Jeong, W.-H. Yeo, Advanced Soft Materials, Sensor Integrations, and Applications of Wearable Flexible Hybrid Electronics in Healthcare, Energy, and Environment, Advanced Materials 32(15) (2020) 1901924.
[90] W. Su, B.S. Cook, Y. Fang, M.M. Tentzeris, Fully inkjet-printed microfluidics: a solution to low-cost rapid three-dimensional microfluidics fabrication with numerous electrical and sensing applications, Scientific Reports 6(1) (2016) 35111.
[91] S. Maruo, K. Ikuta, H. Korogi, Submicron manipulation tools driven by light in a liquid, Applied Physics Letters 82(1) (2002) 133-135.
[92] A. Rashti, B. Wang, E. Hassani, F. Feyzbar-Khalkhali-Nejad, X. Zhang, T.-S. Oh, Electrophoretic Deposition of Nickel Cobaltite/Polyaniline/rGO Composite Electrode for High-Performance All-Solid-State Asymmetric Supercapacitors, Energy & Fuels 34(5) (2020) 6448-6461.
[93] T. Seifert, E. Sowade, F. Roscher, M. Wiemer, T. Gessner, R.R. Baumann, Additive Manufacturing Technologies Compared: Morphology of Deposits of Silver Ink Using Inkjet and Aerosol Jet Printing, Industrial & Engineering Chemistry Research 54(2) (2015) 769-779.
[94] W.Y. Padrón-Hernández, M.C. Ceballos-Chuc, D. Pourjafari, G. Oskam, J.C. Tinoco, A.G. Martínez-López, G. Rodríguez-Gattorno, Stable inks for inkjet printing of TiO2 thin films, Materials Science in Semiconductor Processing 81 (2018) 75-81.
[95] A.J. Huckaba, Y. Lee, R. Xia, S. Paek, V.C. Bassetto, E. Oveisi, A. Lesch, S. Kinge, P.J. Dyson, H. Girault, M.K. Nazeeruddin, Inkjet-Printed Mesoporous TiO2 and Perovskite Layers for High Efficiency Perovskite Solar Cells, Energy Technology 7(2) (2019) 317-324.
[96] D. Friedmann, A.F. Lee, K. Wilson, R. Jalili, R.A. Caruso, Printing approaches to inorganic semiconductor photocatalyst fabrication, Journal of Materials Chemistry A 7(18) (2019) 10858-10878.
[97] M. Mahjouri-Samani, M. Tian, A.A. Puretzky, M. Chi, K. Wang, G. Duscher, C.M. Rouleau, G. Eres, M. Yoon, J. Lasseter, K. Xiao, D.B. Geohegan, Nonequilibrium Synthesis of TiO2 Nanoparticle “Building Blocks” for Crystal Growth by Sequential Attachment in Pulsed Laser Deposition, Nano Letters 17(8) (2017) 4624-4633.

[98] M. Tian, M. Mahjouri-Samani, K. Wang, A.A. Puretzky, D.B. Geohegan, W.D. Tennyson, N. Cross, C.M. Rouleau, T.A. Zawodzinski, G. Duscher, G. Eres, Black Anatase Formation by Annealing of Amorphous Nanoparticles and the Role of the Ti2O3 Shell in Self-Organized Crystallization by Particle Attachment, ACS Applied Materials & Interfaces 9(26) (2017) 22018-22025.
[99] P. Fathi-Hafshejani, H. Johnson, Z. Ahmadi, M. Roach, N. Shamsaei, M. Mahjouri-Samani, Phase-Selective and Localized TiO2 Coating on Additive and Wrought Titanium by a Direct Laser Surface Modification Approach, ACS Omega 5(27) (2020) 16744-16751.
[100] B. Yang, M. Mahjouri-Samani, C.M. Rouleau, D.B. Geohegan, K. Xiao, Low temperature synthesis of hierarchical TiO2 nanostructures for high performance perovskite solar cells by pulsed laser deposition, Physical Chemistry Chemical Physics 18(39) (2016) 27067-27072.
[101] C. Polley, T. Distler, R. Detsch, H. Lund, A. Springer, A.R. Boccaccini, H. Seitz, 3D Printing of Piezoelectric Barium Titanate-Hydroxyapatite Scaffolds with Interconnected Porosity for Bone Tissue Engineering, Materials (Basel) 13(7) (2020) 1773.
[102] S.M. Gaytan, M.A. Cadena, H. Karim, D. Delfin, Y. Lin, D. Espalin, E. MacDonald, R.B. Wicker, Fabrication of barium titanate by binder jetting additive manufacturing technology, Ceramics International 41(5, Part A) (2015) 6610-6619.
[103] M. Mikolajek, T. Reinheimer, N. Bohn, C. Kohler, M.J. Hoffmann, J.R. Binder, Fabrication and Characterization of Fully Inkjet Printed Capacitors Based on Ceramic/Polymer Composite Dielectrics on Flexible Substrates, Scientific Reports 9(1) (2019) 13324.
[104] E. Gilshtein, S. Bolat, G.T. Sevilla, A. Cabas-Vidani, F. Clemens, T. Graule, A.N. Tiwari, Y.E. Romanyuk, Inkjet-Printed Conductive ITO Patterns for Transparent Security Systems, Advanced Materials Technologies n/a(n/a) (2020) 2000369.
[105] D.S. Engstrom, B. Porter, M. Pacios, H. Bhaskaran, Additive nanomanufacturing – A review, Journal of Materials Research 29(17) (2014) 1792-1816.
[106] C. Zhao, P.J. Shah, L.J. Bissell, Laser additive nano-manufacturing under ambient conditions, Nanoscale 11(35) (2019) 16187-16199.
[107] M.S. Alam, Q. Zhan, C. Zhao, Additive Opto-Thermomechanical Nanoprinting and Nanorepairing under Ambient Conditions, Nano Letters 20(7) (2020) 5057-5064.
[108] W. Xiong, Y.S. Zhou, X.N. He, Y. Gao, M. Mahjouri-Samani, L. Jiang, T. Baldacchini, Y.F. Lu, Simultaneous additive and subtractive three-dimensional nanofabrication using integrated two-photon polymerization and multiphoton ablation, Light: Science & Applications 1(4) (2012) e6-e6.
[109] Z. Zhang, J. Yan, T. Kuriyagawa, Manufacturing technologies toward extreme precision, International Journal of Extreme Manufacturing 1(2) (2019) 022001.
[110] K. Sugioka, Hybrid femtosecond laser three-dimensional micro-and nanoprocessing: a review, International Journal of Extreme Manufacturing 1(1) (2019) 012003.
[111] F. Fang, N. Zhang, D. Guo, K. Ehmann, B. Cheung, K. Liu, K. Yamamura, Towards atomic and close-to-atomic scale manufacturing, International Journal of Extreme Manufacturing 1(1) (2019) 012001.
[112] Z. Ahmadi, B. Yakupoglu, N. Azam, S. Elafandi, M. Mahjouri-Samani, Self-limiting laser crystallization and direct writing of 2D materials, International Journal of Extreme Manufacturing 1(1) (2019) 015001.
[113] Z. Ahmadi, B. Yakupoglu, N. Azam, S. Elafandi, M. Mahjouri-Samani, Application of lasers in the synthesis and processing of two-dimensional quantum materials, Journal of Laser Applications 31(3) (2019) 031202.

[114] M. Izadi, A. Farzaneh, M. Mohammed, I. Gibson, B. Rolfe, A review of laser engineered net shaping (LENS) build and process parameters of metallic parts, Rapid Prototyping Journal 26(6) (2020) 1059-1078.
[115] N. Shamsaei, A. Yadollahi, L. Bian, S.M. Thompson, An overview of Direct Laser Deposition for additive manufacturing; Part II: Mechanical behavior, process parameter optimization and control, Additive Manufacturing 8 (2015) 12-35.
[116] O. Frank, M. Zukalova, B. Laskova, J. Kürti, J. Koltai, L. Kavan, Raman spectra of titanium dioxide (anatase, rutile) with identified oxygen isotopes (16, 17, 18), Physical Chemistry Chemical Physics 14(42) (2012) 14567-14572.
[117] K.F. McCarty, Raman scattering as a technique of measuring film thickness: interference effects in thin growing films, Appl. Opt. 26(20) (1987) 4482-4486.
[118] A. Hu, R. Li, D. Bridges, W. Zhou, S. Bai, D. Ma, P. Peng, Photonic nanomanufacturing of high performance energy devices on flexible substrates, Journal of Laser Applications 28(2) (2016) 022602.
[119] W. Qiao, W. Huang, Y. Liu, X. Li, L.-S. Chen, J.-X. Tang, Toward Scalable Flexible Nanomanufacturing for Photonic Structures and Devices, Advanced Materials 28(47) (2016) 10353-10380.
[120] Z. Ahmadi, P. Fathi-Hafshejani, E. Kayali, M. Beidaghi, M. Mahjouri-Samani, Rapid laser nanomanufacturing and direct patterning of 2D materials on flexible substrates—2DFlex, Nanotechnology 32(5) (2020) 055302.
[121] Z. Ahmadi, S. Lee, N. Shamsaei, M. Mahjouri-Samani, H. Helvajian, B. Gu, H. Chen, Additive nanomanufacturing of functional materials and devices, Laser 3D Manufacturing VIII, 2021.
[122] Z. Ahmadi, S. Lee, R.R. Unocic, N. Shamsaei, M. Mahjouri-Samani, Additive Nanomanufacturing of Multifunctional Materials and Patterned Structures: A Novel Laser-Based Dry Printing Process, Advanced Materials Technologies (2021).
[123] Y. Khan, A. Thielens, S. Muin, J. Ting, C. Baumbauer, A.C. Arias, A New Frontier of Printed Electronics: Flexible Hybrid Electronics, Advanced Materials 32(15) (2019).
[124] L. Liu, Z. Shen, X. Zhang, H. Ma, Highly conductive graphene/carbon black screen printing inks for flexible electronics, Journal of Colloid and Interface Science 582 (2021) 12-21.
[125] R.D. Rodriguez, S. Shchadenko, G. Murastov, A. Lipovka, M. Fatkullin, I. Petrov, T.H. Tran, A. Khalelov, M. Saqib, N.E. Villa, V. Bogoslovskiy, Y. Wang, C.G. Hu, A. Zinovyev, W. Sheng, J.J. Chen, I. Amin, E. Sheremet, Ultra-Robust Flexible Electronics by Laser-Driven Polymer-Nanomaterials Integration, Advanced Functional Materials (2021).
[126] G. Tarabella, D. Vurro, S. Lai, P. D'Angelo, L. Ascari, S. Iannotta, Aerosol jet printing of PEDOT:PSS for large area flexible electronics, Flexible and Printed Electronics 5(1) (2020).
[127] Z. Zhou, H. Zhang, J. Liu, W. Huang, Flexible electronics from intrinsically soft materials, Giant 6 (2021).
[128] A.H. Espera, J.R.C. Dizon, Q. Chen, R.C. Advincula, 3D-printing and advanced manufacturing for electronics, Progress in Additive Manufacturing 4(3) (2019) 245-267.
[129] E. Castillo-Orozco, R. Kumar, A. Kar, Laser electrospray printing of nanoparticles on flexible and rigid substrates, Journal of Laser Applications 31(2) (2019).
[130] S. Wang, Y. Yu, D. Ma, D. Bridges, G. Feng, A. Hu, High performance hybrid supercapacitors on flexible polyimide sheets using femtosecond laser 3D writing, Journal of Laser Applications 29(2) (2017).

[131] A. Hu, R. Li, D. Bridges, W. Zhou, S. Bai, D. Ma, P. Peng, Photonic nanomanufacturing of high performance energy devices on flexible substrates, Journal of Laser Applications 28(2) (2016).
[132] P. Pathak, E. Castillo-Orozco, R. Kumar, A. Kar, H.J. Cho, Effect of laser power on conductivity and morphology of silver nanoparticle thin films prepared by a laser assisted electrospray deposition method, Journal of Laser Applications 33(1) (2021).
[133] A. Zolfaghari, T. Chen, A.Y. Yi, Additive manufacturing of precision optics at micro and nanoscale, International Journal of Extreme Manufacturing 1(1) (2019).
[134] F. Fang, N. Zhang, D. Guo, K. Ehmann, B. Cheung, K. Liu, K. Yamamura, Towards atomic and close-to-atomic scale manufacturing, International Journal of Extreme Manufacturing 1(1) (2019).
[135] A. Gumyusenge, X. Luo, Z. Ke, D.T. Tran, J. Mei, Polyimide-Based High-Temperature Plastic Electronics, ACS Materials Letters 1(1) (2019) 154-157.
[136] F. Yin, J. Yang, H. Peng, W. Yuan, Flexible and highly sensitive artificial electronic skin based on graphene/polyamide interlocking fabric, Journal of Materials Chemistry C 6(25) (2018) 6840-6846.
[137] V. Zardetto, T.M. Brown, A. Reale, A. Di Carlo, Substrates for flexible electronics: A practical investigation on the electrical, film flexibility, optical, temperature, and solvent resistance properties, Journal of Polymer Science Part B: Polymer Physics 49(9) (2011) 638-648.
[138] T. Santaniello, P. Milani, Additive nano-manufacturing of 3D printed electronics using supersonic cluster beam deposition, Cluster Beam Deposition of Functional Nanomaterials and Devices2020, pp. 313-333.
[139] G. Shin, B. Jeon, Y.-L. Park, Direct printing of sub-30 μ m liquid metal patterns on three-dimensional surfaces for stretchable electronics, Journal of Micromechanics and Microengineering 30(3) (2020) 034001.
[140] S. Kee, P. Zhang, J. Travas-Sejdic, Direct writing of 3D conjugated polymer micro/nanostructures for organic electronics and bioelectronics, Polymer Chemistry 11(28) (2020) 4530-4541.
[141] K.N. Al-Milaji, Q. Huang, Z. Li, T.N. Ng, H. Zhao, Direct Embedment and Alignment of Silver Nanowires by Inkjet Printing for Stretchable Conductors, ACS Applied Electronic Materials 2(10) (2020) 3289-3298.
[142] K.-S. Kwon, M.K. Rahman, T.H. Phung, S. Hoath, S. Jeong, J.S. Kim, Review of digital printing technologies for electronic materials, Flexible and Printed Electronics (2020).
[143] C. Zhao, Laser additive manufacturing at the nanoscales under ambient conditions, OSA Advanced Photonics Congress (AP) 2020 (IPR, NP, NOMA, Networks, PVLED, PSC, SPPCom, SOF), 2020.
[144] M. Singh, H.M. Haverinen, P. Dhagat, G.E. Jabbour, Inkjet Printing-Process and Its Applications, Advanced Materials 22(6) (2010) 673-685.
[145] N.C. Raut, K. Al-Shamery, Inkjet printing metals on flexible materials for plastic and paper electronics, Journal of Materials Chemistry C 6(7) (2018) 1618-1641.
[146] A. Sajedi-Moghaddam, E. Rahmanian, N. Naseri, Inkjet-Printing Technology for Supercapacitor Application: Current State and Perspectives, ACS Applied Materials & Interfaces 12(31) (2020) 34487-34504.
[147] Y.-D. Chen, V. Nagarajan, D.W. Rosen, W. Yu, S.Y. Huang, Aerosol jet printing on paper substrate with conductive silver nano material, Journal of Manufacturing Processes 58 (2020) 55-66.

[148] N. Ćatić, L. Wells, K. Al Nahas, M. Smith, Q. Jing, U.F. Keyser, J. Cama, S. Kar-Narayan, Aerosol-jet printing facilitates the rapid prototyping of microfluidic devices with versatile geometries and precise channel functionalization, Applied Materials Today 19 (2020).
[149] P. Patil, S. Patil, P. Kate, A.A. Kulkarni, Inkjet printing of silver nanowires on flexible surfaces and methodologies to improve the conductivity and stability of the printed patterns, Nanoscale Advances 3(1) (2021) 240-248.
[150] E. Gilshtein, S. Bolat, G.T. Sevilla, A. Cabas-Vidani, F. Clemens, T. Graule, A.N. Tiwari, Y.E. Romanyuk, Inkjet-Printed Conductive ITO Patterns for Transparent Security Systems, Advanced Materials Technologies (2020).
[151] C. Zhang, L. McKeon, M.P. Kremer, S.-H. Park, O. Ronan, A. Seral-Ascaso, S. Barwich, C.Ó. Coileáin, N. McEvoy, H.C. Nerl, B. Anasori, J.N. Coleman, Y. Gogotsi, V. Nicolosi, Additive-free MXene inks and direct printing of micro-supercapacitors, Nature Communications 10(1) (2019).
[152] S. Uzun, M. Schelling, K. Hantanasirisakul, T.S. Mathis, R. Askeland, G. Dion, Y. Gogotsi, Additive-Free Aqueous MXene Inks for Thermal Inkjet Printing on Textiles, Small 17(1) (2020).
[153] A. Lee, K. Sudau, K.H. Ahn, S.J. Lee, N. Willenbacher, Optimization of Experimental Parameters to Suppress Nozzle Clogging in Inkjet Printing, Industrial & Engineering Chemistry Research 51(40) (2012) 13195-13204.
[154] J.F. Salmerón, F. Molina-Lopez, D. Briand, J.J. Ruan, A. Rivadeneyra, M.A. Carvajal, L.F. Capitán-Vallvey, N.F. de Rooij, A.J. Palma, Properties and Printability of Inkjet and Screen-Printed Silver Patterns for RFID Antennas, Journal of Electronic Materials 43(2) (2013) 604-617.
[155] M.A. Mohd Asri, N.A. Ramli, A.N. Nordin, Electrical performance and reliability assessment of silver inkjet printed circuits on flexible substrates, Journal of Materials Science: Materials in Electronics 32(12) (2021) 16024-16037.
[156] D.-J. Lee, D.Y. Kim, Paper-Based, Hand-Painted Strain Sensor Based on ITO Nanoparticle Channels for Human Motion Monitoring, IEEE Access 7 (2019) 77200-77207.
[157] T. Lee, Y.W. Choi, G. Lee, P.V. Pikhitsa, D. Kang, S.M. Kim, M. Choi, Transparent ITO mechanical crack-based pressure and strain sensor, Journal of Materials Chemistry C 4(42) (2016) 9947-9953.
[158] S.-H. Park, S.-J. Lee, J.H. Lee, J. Kal, J. Hahn, H.-K. Kim, Large area roll-to-roll sputtering of transparent ITO/Ag/ITO cathodes for flexible inverted organic solar cell modules, Organic Electronics 30 (2016) 112-121.
[159] F. Zhu, K. Zhang, E. Guenther, C.S. Jin, Optimized indium tin oxide contact for organic light emitting diode applications, Thin Solid Films 363(1-2) (2000) 314-317.
[160] P. Jha, S.P. Koiry, V. Saxena, P. Veerender, A. Gusain, A.K. Chauhan, A.K. Debnath, D.K. Aswal, S.K. Gupta, Air-stability and bending properties of flexible organic field-effect transistors based on poly[N-9′-heptadecanyl-2,7-carbazole-alt-5,5-(4′,7′-di-2-thienyl-2′,1′,3′-benzothiadiazole)], Organic Electronics 14(10) (2013) 2635-2644.
[161] V. Raghuwanshi, D. Bharti, S.P. Tiwari, Flexible organic field-effect transistors with TIPS-Pentacene crystals exhibiting high electrical stability upon bending, Organic Electronics 31 (2016) 177-182.
[162] D. Barmpakos, C. Tsamis, G. Kaltsas, Multi-parameter paper sensor fabricated by inkjet-printed silver nanoparticle ink and PEDOT:PSS, Microelectronic Engineering 225 (2020).

[163] P.T. Bishop, L.J. Ashfield, A. Berzins, A. Boardman, V. Buche, J. Cookson, R.J. Gordon, C. Salcianu, P.A. Sutton, Printed gold for electronic applications, Gold Bulletin 43(3) (2010) 181-188.
[164] A. Määttänen, P. Ihalainen, P. Pulkkinen, S. Wang, H. Tenhu, J. Peltonen, Inkjet-Printed Gold Electrodes on Paper: Characterization and Functionalization, ACS Applied Materials & Interfaces 4(2) (2012) 955-964.
[165] E. Redondo, M. Pumera, Fully metallic copper 3D-printed electrodes via sintering for electrocatalytic biosensing, Applied Materials Today 25 (2021).
[166] Z. Ahmadi, S. Lee, A. Patel, R.R. Unocic, N. Shamsaei, M. Mahjouri-Samani, Dry Printing and Additive Nanomanufacturing of Flexible Hybrid Electronics and Sensors, Advanced Materials Interfaces 9(12) (2022).
[167] A. Kamyshny, S. Magdassi, Conductive Nanomaterials for Printed Electronics, Small 10(17) (2014) 3515-3535.
[168] A. Oliva-Puigdomènech, J. De Roo, H. Van Avermaet, K. De Buysser, Z. Hens, Scalable Approaches to Copper Nanocrystal Synthesis under Ambient Conditions for Printed Electronics, ACS Applied Nano Materials 3(4) (2020) 3523-3531.
[169] N. Sarwar, S.H. Choi, G. Dastgeer, U.B. Humayoun, M. Kumar, A. Nawaz, D.I. Jeong, S.F.A. Zaidi, D.H. Yoon, Synthesis of citrate-capped copper nanoparticles: A low temperature sintering approach for the fabrication of oxidation stable flexible conductive film, Applied Surface Science 542 (2021).
[170] M.B. Gawande, A. Goswami, F.-X. Felpin, T. Asefa, X. Huang, R. Silva, X. Zou, R. Zboril, R.S. Varma, Cu and Cu-Based Nanoparticles: Synthesis and Applications in Catalysis, Chemical Reviews 116(6) (2016) 3722-3811.
[171] B. Lee, Y. Kim, S. Yang, I. Jeong, J. Moon, A low-cure-temperature copper nano ink for highly conductive printed electrodes, Current Applied Physics 9(2) (2009) e157-e160.
[172] T. Öhlund, A.K. Schuppert, M. Hummelgård, J. Bäckström, H.-E. Nilsson, H. Olin, Inkjet Fabrication of Copper Patterns for Flexible Electronics: Using Paper with Active Precoatings, ACS Applied Materials & Interfaces 7(33) (2015) 18273-18282.
[173] S.-J. Oh, T.G. Kim, S.-Y. Kim, Y. Jo, S.S. Lee, K. Kim, B.-H. Ryu, J.-U. Park, Y. Choi, S. Jeong, Newly Designed Cu/Cu10Sn3 Core/Shell Nanoparticles for Liquid Phase-Photonic Sintered Copper Electrodes: Large-Area, Low-Cost Transparent Flexible Electronics, Chemistry of Materials 28(13) (2016) 4714-4723.
[174] D. Tomotoshi, H. Kawasaki, Surface and Interface Designs in Copper-Based Conductive Inks for Printed/Flexible Electronics, Nanomaterials 10(9) (2020).
[175] W. Li, L. Li, Y. Gao, D. Hu, C.-F. Li, H. Zhang, J. Jiu, S. Nagao, K. Suganuma, Highly conductive copper films based on submicron copper particles/copper complex inks for printed electronics: Microstructure, resistivity, oxidation resistance, and long-term stability, Journal of Alloys and Compounds 732 (2018) 240-247.
[176] B.K. Park, D. Kim, S. Jeong, J. Moon, J.S. Kim, Direct writing of copper conductive patterns by ink-jet printing, Thin Solid Films 515(19) (2007) 7706-7711.
[177] S. Jeong, K. Woo, D. Kim, S. Lim, J.S. Kim, H. Shin, Y. Xia, J. Moon, Controlling the Thickness of the Surface Oxide Layer on Cu Nanoparticles for the Fabrication of Conductive Structures by Ink-Jet Printing, Advanced Functional Materials 18(5) (2008) 679-686.
[178] Y. Li, X. Tang, Y. Zhang, J. Li, C. Lv, X. Meng, Y. Huang, C. Hang, C. Wang, Cu nanoparticles of low polydispersity synthesized by a double-template method and their stability, Colloid and Polymer Science 292(3) (2013) 715-722.

[179] Z. Ahmadi, S. Lee, R.R. Unocic, N. Shamsaei, M. Mahjouri-Samani, Additive Nanomanufacturing of Multifunctional Materials and Patterned Structures: A Novel Laser-Based Dry Printing Process, Advanced Materials Technologies 6(5) (2021).
[180] Z. Ahmadi, S. Lee, R.R. Unocic, N. Shamsaei, M. Mahjouri-Samani, A.V. Kabashin, M. Farsari, M. Mahjouri-Samani, Laser-based additive nanomanufacturing of functional hybrid materials, structures, and devices, Nanoscale and Quantum Materials: From Synthesis and Laser Processing to Applications 2022, 2022.
[181] F. Sawamura, C.Y. Ngu, R. Hanazaki, K. Kozuki, S. Kado, M. Sakai, K. Kudo, Dry Printing of Ag–Ni Conductive Particles Using Toner-Type Printed Electronics, Applied Sciences 12(19) (2022).
[182] S.P. Sreenilayam, É. McCarthy, L. McKeon, O. Ronan, R. McCann, K. Fleischer, B. Freeland, V. Nicolosi, D. Brabazon, Additive-free silver nanoparticle ink development using flow-based Laser Ablation Synthesis in Solution and Aerosol Jet printing, Chemical Engineering Journal 449 (2022).
[183] P. Lall, V. Soni, C. Hill, Process Development for Printing Copper Conductible Ink on Flexible Substrates using Aerosol Jet Printing Technology, 2021 20th IEEE Intersociety Conference on Thermal and Thermomechanical Phenomena in Electronic Systems (iTherm), 2021, pp. 1073-1084.
[184] N.K. Roy, D. Behera, O.G. Dibua, C.S. Foong, M.A. Cullinan, Single shot, large area metal sintering with micrometer level resolution, Optics Express 26(20) (2018).
[185] S. Magdassi, M. Grouchko, A. Kamyshny, Copper Nanoparticles for Printed Electronics: Routes Towards Achieving Oxidation Stability, Materials 3(9) (2010) 4626-4638.
[186] Y.-H. Son, J.-Y. Jang, M.K. Kang, S. Ahn, C.S. Lee, Application of flash-light sintering method to flexible inkjet printing using anti-oxidant copper nanoparticles, Thin Solid Films 656 (2018) 61-67.
[187] Y. Lee, J.-r. Choi, K.J. Lee, N.E. Stott, D. Kim, Large-scale synthesis of copper nanoparticles by chemically controlled reduction for applications of inkjet-printed electronics, Nanotechnology 19(41) (2008).
[188] A. Sheng, S. Khuje, Z. Li, J. Yu, S. Ren, Conformal Cu–CuNi Thermocouple Using Particle-Free Ink Materials, ACS Applied Electronic Materials 4(11) (2022) 5558-5564.
[189] Y.-T. Kwon, Y.-S. Kim, Y. Lee, S. Kwon, M. Lim, Y. Song, Y.-H. Choa, W.-H. Yeo, Ultrahigh Conductivity and Superior Interfacial Adhesion of a Nanostructured, Photonic-Sintered Copper Membrane for Printed Flexible Hybrid Electronics, ACS Applied Materials & Interfaces 10(50) (2018) 44071-44079.
[190] K.D. Harris, A.L. Elias, H.J. Chung, Flexible electronics under strain: a review of mechanical characterization and durability enhancement strategies, Journal of Materials Science 51(6) (2015) 2771-2805.
[191] D. Corzo, G. Tostado-Blázquez, D. Baran, Flexible Electronics: Status, Challenges and Opportunities, Frontiers in Electronics 1 (2020).
[192] H. Liu, H. Zhang, W. Han, H. Lin, R. Li, J. Zhu, W. Huang, 3D Printed Flexible Strain Sensors: From Printing to Devices and Signals, Advanced Materials 33(8) (2021).
[193] G.C. Righini, J. Krzak, A. Lukowiak, G. Macrelli, S. Varas, M. Ferrari, From flexible electronics to flexible photonics: A brief overview, Optical Materials 115 (2021).
[194] P. Giannakou, M.G. Masteghin, R.C.T. Slade, S.J. Hinder, M. Shkunov, Energy storage on demand: ultra-high-rate and high-energy-density inkjet-printed NiO micro-supercapacitors, Journal of Materials Chemistry A 7(37) (2019) 21496-21506.

[195] R. Šakalys, B.S. Mohammadlou, R. Raghavendra, Fabrication of multi-material electronic components applying non-contact printing technologies: A review, Results in Engineering 15 (2022).
[196] A. Renteria, V.H. Balcorta, C. Marquez, A.A. Rodriguez, I. Renteria-Marquez, J. Regis, B. Wilburn, S. Patterson, D. Espalin, T.-L. Tseng, Y. Lin, Direct ink write multi-material printing of PDMS-BTO composites with MWCNT electrodes for flexible force sensors, Flexible and Printed Electronics 7(1) (2022).
[197] J. Wu, H. Pang, L. Ding, Y. Wang, X. He, Q. Shu, S. Xuan, X. Gong, A lightweight, ultrathin aramid-based flexible sensor using a combined inkjet printing and buckling strategy, Chemical Engineering Journal 421 (2021).
[198] Z. Ahmadi, P. Fathi-Hafshejani, E. Kayali, M. Beidaghi, M. Mahjouri-Samani, Rapid laser nanomanufacturing and direct patterning of 2D materials on flexible substrates—2DFlex, Nanotechnology 32(5) (2020).
[199] S. Choi, H. Lee, R. Ghaffari, T. Hyeon, D.-H. Kim, Recent Advances in Flexible and Stretchable Bio-Electronic Devices Integrated with Nanomaterials, Advanced Materials 28(22) (2016) 4203-4218.
[200] J.A. Rogers, T. Someya, Y. Huang, Materials and Mechanics for Stretchable Electronics, Science 327(5973) (2010) 1603-1607.
[201] S. Ma, Y. Kumaresan, A.S. Dahiya, R. Dahiya, Ultra-Thin Chips with Printed Interconnects on Flexible Foils, Advanced Electronic Materials 8(5) (2021).
[202] N. Divakaran, J.P. Das, A.K. P V, S. Mohanty, A. Ramadoss, S.K. Nayak, Comprehensive review on various additive manufacturing techniques and its implementation in electronic devices, Journal of Manufacturing Systems 62 (2022) 477-502.
[203] E. MacDonald, R. Wicker, Multiprocess 3D printing for increasing component functionality, Science 353(6307) (2016).
[204] H.W. Tan, Y.Y.C. Choong, C.N. Kuo, H.Y. Low, C.K. Chua, 3D printed electronics: Processes, materials and future trends, Progress in Materials Science 127 (2022).
[205] L. Jaksa, D. Pahr, G. Kronreif, A. Lorenz, Development of a Multi-Material 3D Printer for Functional Anatomic Models, International Journal of Bioprinting 7(4) (2021).
[206] R. Bernasconi, D. Hatami, H.N. Hosseinabadi, V. Zega, A. Corigliano, R. Suriano, M. Levi, G. Langfelder, L. Magagnin, Hybrid additive manufacturing of a piezopolymer-based inertial sensor, Additive Manufacturing 59 (2022).
[207] Y. Li, R. Wang, X. Zhu, J. Yang, L. Zhou, S. Shang, P. Sun, W. Ge, Q. Xu, H. Lan, Multinozzle 3D Printing of Multilayer and Thin Flexible Electronics, Advanced Engineering Materials (2022).
[208] W.Y. Yeong, G.L. Goh, G.D. Goh, S. Lee, J. Altherr, J. Tan, D. Campolo, 3D printing of soft grippers with multimaterial design: Towards shape conformance and tunable rigidity, Materials Today: Proceedings (2022).
[209] R. Wick-Joliat, M. Schroffenegger, D. Penner, Multi-material ceramic material extrusion 3D printing with granulated injection molding feedstocks, Ceramics International (2022).
[210] S. Tibbits, 4D Printing: Multi-Material Shape Change, Architectural Design 84(1) (2014) 116-121.
[211] L.R. Lopes, A.F. Silva, O.S. Carneiro, Multi-material 3D printing: The relevance of materials affinity on the boundary interface performance, Additive Manufacturing 23 (2018) 45-52.

[212] D. Wang, L. Liu, G. Deng, C. Deng, Y. Bai, Y. Yang, W. Wu, J. Chen, Y. Liu, Y. Wang, X. Lin, C. Han, Recent progress on additive manufacturing of multi-material structures with laser powder bed fusion, Virtual and Physical Prototyping 17(2) (2022) 329-365.
[213] U. Shaukat, E. Rossegger, S. Schlögl, A Review of Multi-Material 3D Printing of Functional Materials via Vat Photopolymerization, Polymers 14(12) (2022).
[214] B. Grigoryan, D.W. Sazer, A. Avila, J.L. Albritton, A. Padhye, A.H. Ta, P.T. Greenfield, D.L. Gibbons, J.S. Miller, Development, characterization, and applications of multi-material stereolithography bioprinting, Scientific Reports 11(1) (2021).
[215] D. Chen, X. Zheng, Multi-material Additive Manufacturing of Metamaterials with Giant, Tailorable Negative Poisson's Ratios, Scientific Reports 8(1) (2018).
[216] A.C. Lamont, M.A. Restaino, M.J. Kim, R.D. Sochol, A facile multi-material direct laser writing strategy, Lab on a Chip 19(14) (2019) 2340-2345.
[217] A.D. Valentine, T.A. Busbee, J.W. Boley, J.R. Raney, A. Chortos, A. Kotikian, J.D. Berrigan, M.F. Durstock, J.A. Lewis, Hybrid 3D Printing of Soft Electronics, Advanced Materials 29(40) (2017).
[218] G.L. Goh, H. Zhang, T.H. Chong, W.Y. Yeong, 3D Printing of Multilayered and Multimaterial Electronics: A Review, Advanced Electronic Materials 7(10) (2021).
[219] M.A. Skylar-Scott, J. Mueller, C.W. Visser, J.A. Lewis, Voxelated soft matter via multimaterial multinozzle 3D printing, Nature 575(7782) (2019) 330-335.
[220] W. Liu, Y.S. Zhang, M.A. Heinrich, F. De Ferrari, H.L. Jang, S.M. Bakht, M.M. Alvarez, J. Yang, Y.-C. Li, G. Trujillo-de Santiago, A.K. Miri, K. Zhu, P. Khoshakhlagh, G. Prakash, H. Cheng, X. Guan, Z. Zhong, J. Ju, G.H. Zhu, X. Jin, S.R. Shin, M.R. Dokmeci, A. Khademhosseini, Rapid Continuous Multimaterial Extrusion Bioprinting, Advanced Materials 29(3) (2017).
[221] K. Sun, T.-S. Wei, B.Y. Ahn, J.Y. Seo, S.J. Dillon, J.A. Lewis, 3D Printing of Interdigitated Li-Ion Microbattery Architectures, Advanced Materials 25(33) (2013) 4539-4543.
[222] J.J. Adams, E.B. Duoss, T.F. Malkowski, M.J. Motala, B.Y. Ahn, R.G. Nuzzo, J.T. Bernhard, J.A. Lewis, Conformal Printing of Electrically Small Antennas on Three-Dimensional Surfaces, Advanced Materials 23(11) (2011) 1335-1340.
[223] J.T. Muth, D.M. Vogt, R.L. Truby, Y. Mengüç, D.B. Kolesky, R.J. Wood, J.A. Lewis, Embedded 3D Printing of Strain Sensors within Highly Stretchable Elastomers, Advanced Materials 26(36) (2014) 6307-6312.
[224] B.G. Compton, J.A. Lewis, 3D Printing: 3D-Printing of Lightweight Cellular Composites (Adv. Mater. 34/2014), Advanced Materials 26(34) (2014) 6043-6043.
[225] D.B. Kolesky, R.L. Truby, A.S. Gladman, T.A. Busbee, K.A. Homan, J.A. Lewis, 3D Bioprinting of Vascularized, Heterogeneous Cell-Laden Tissue Constructs, Advanced Materials 26(19) (2014) 3124-3130.
[226] C.J. Hansen, R. Saksena, D.B. Kolesky, J.J. Vericella, S.J. Kranz, G.P. Muldowney, K.T. Christensen, J.A. Lewis, High-Throughput Printing via Microvascular Multinozzle Arrays, Advanced Materials 25(1) (2013) 96-102.
[227] D.J. Lorang, D. Tanaka, C.M. Spadaccini, K.A. Rose, N.J. Cherepy, J.A. Lewis, Photocurable Liquid Core-Fugitive Shell Printing of Optical Waveguides, Advanced Materials 23(43) (2011) 5055-5058.
[228] J.O. Hardin, T.J. Ober, A.D. Valentine, J.A. Lewis, Microfluidic Printheads for Multimaterial 3D Printing of Viscoelastic Inks, Advanced Materials 27(21) (2015) 3279-3284.

[229] W.C. Liu, V.H.Y. Chou, R.P. Behera, H. Le Ferrand, Magnetically assisted drop-on-demand 3D printing of microstructured multimaterial composites, Nature Communications 13(1) (2022).
[230] R. Hensleigh, H. Cui, Z. Xu, J. Massman, D. Yao, J. Berrigan, X. Zheng, Charge-programmed three-dimensional printing for multi-material electronic devices, Nature Electronics 3(4) (2020) 216-224.
[231] V.-T. Tran, Y. Wei, H. Du, On-Substrate Joule Effect Heating by Printed Micro-Heater for the Preparation of ZnO Semiconductor Thin Film, Micromachines 11(5) (2020).
[232] S.H. Park, R. Su, J. Jeong, S.Z. Guo, K. Qiu, D. Joung, F. Meng, M.C. McAlpine, 3D Printed Polymer Photodetectors, Advanced Materials 30(40) (2018).
[233] H. Li, Y. Ma, Y. Huang, Material innovation and mechanics design for substrates and encapsulation of flexible electronics: a review, Materials Horizons 8(2) (2021) 383-400.
[234] J. Guo, Y. Yu, L. Cai, Y. Wang, K. Shi, L. Shang, J. Pan, Y. Zhao, Microfluidics for flexible electronics, Materials Today 44 (2021) 105-135.
[235] P. Wang, M. Hu, H. Wang, Z. Chen, Y. Feng, J. Wang, W. Ling, Y. Huang, The Evolution of Flexible Electronics: From Nature, Beyond Nature, and To Nature, Advanced Science 7(20) (2020).
[236] Y. Zhao, J. Guo, Development of flexible Li-ion batteries for flexible electronics, InfoMat 2(5) (2020) 866-878.
[237] F. Gheorghiu, R. Stanculescu, L. Curecheriu, E. Brunengo, P. Stagnaro, V. Tiron, P. Postolache, M.T. Buscaglia, L. Mitoseriu, PVDF–ferrite composites with dual magneto-piezoelectric response for flexible electronics applications: synthesis and functional properties, Journal of Materials Science 55(9) (2019) 3926-3939.
[238] P. Zhu, Y. Wang, Y. Wang, H. Mao, Q. Zhang, Y. Deng, Flexible 3D Architectured Piezo/Thermoelectric Bimodal Tactile Sensor Array for E-Skin Application, Advanced Energy Materials 10(39) (2020).
[239] T. Zhang, Q. Cheng, B. Jiang, Y. Huang, Design of the novel polyaniline/polysiloxane flexible nanocomposite film and its application in gas sensor, Composites Part B: Engineering 196 (2020).
[240] R. Liu, K. Wang, Z. Liu, Y. Xu, Q. Wang, M. Luo, X. Shi, S. Ye, In Situ Growth of Silver Film on Polyimide with Tuned Morphologies for Flexible Electronics, Langmuir (2021).
[241] J. Brenneman, D.Z. Tansel, G.K. Fedder, R. Panat, Interfacial delamination and delamination mechanism maps for 3D printed flexible electrical interconnects, Extreme Mechanics Letters 43 (2021).
[242] W.-S. Lei, A. Kumar, Delamination and Reliability Issues in Packaged Devices, Adhesion in Microelectronics2014, pp. 267-312.
[243] S.-M. Yi, I.-S. Choi, B.-J. Kim, Y.-C. Joo, Reliability Issues and Solutions in Flexible Electronics Under Mechanical Fatigue, Electronic Materials Letters 14(4) (2018) 387-404.
[244] L.y. Zhou, J.z. Fu, Q. Gao, P. Zhao, Y. He, All-Printed Flexible and Stretchable Electronics with Pressing or Freezing Activatable Liquid-Metal–Silicone Inks, Advanced Functional Materials 30(3) (2019).
[245] C.-K. Chen, Y.-C. Lin, S. Miyane, S. Ando, M. Ueda, W.-C. Chen, Thermally and Mechanically Stable Polyimides as Flexible Substrates for Organic Field-Effect Transistors, ACS Applied Polymer Materials 2(8) (2020) 3422-3432.

[246] Y. Matsumura, Y. Enomoto, T. Tsuruoka, K. Akamatsu, H. Nawafune, Fabrication of Copper Damascene Patterns on Polyimide Using Direct Metallization on Trench Templates Generated by Imprint Lithography, Langmuir 26(14) (2010) 12448-12454.
[247] R. Rahimi, M. Ochoa, B. Ziaie, Direct Laser Writing of Porous-Carbon/Silver Nanocomposite for Flexible Electronics, ACS Applied Materials & Interfaces 8(26) (2016) 16907-16913.
[248] J. Li, E.H. Hill, L. Lin, Y. Zheng, Optical Nanoprinting of Colloidal Particles and Functional Structures, ACS Nano 13(4) (2019) 3783-3795.
[249] E.P. Koumoulos, E. Gkartzou, C.A. Charitidis, Additive (nano)manufacturing perspectives: the use of nanofillers and tailored materials, Manufacturing Review 4 (2017).
[250] S. Xu, W. Wu, Ink-Based Additive Nanomanufacturing of Functional Materials for Human-Integrated Smart Wearables, Advanced Intelligent Systems 2(10) (2020).
[251] M. Ghayoomi Mohammadi, D. Mahmoud, M. Elbestawi, On the application of machine learning for defect detection in L-PBF additive manufacturing, Optics & Laser Technology 143 (2021).
[252] T.J. Fleck, A.K. Murray, I.E. Gunduz, S.F. Son, G.T.C. Chiu, J.F. Rhoads, Additive manufacturing of multifunctional reactive materials, Additive Manufacturing 17 (2017) 176-182.
[253] K. Yan, J. Li, L. Pan, Y. Shi, Inkjet printing for flexible and wearable electronics, APL Materials 8(12) (2020).
[254] E. Jabari, E. Toyserkani, Aerosol-Jet printing of highly flexible and conductive graphene/silver patterns, Materials Letters 174 (2016) 40-43.
[255] A.J.L. Garcia, G. Sico, M. Montanino, V. Defoor, M. Pusty, X. Mescot, F. Loffredo, F. Villani, G. Nenna, G. Ardila, Low-Temperature Growth of ZnO Nanowires from Gravure-Printed ZnO Nanoparticle Seed Layers for Flexible Piezoelectric Devices, Nanomaterials 11(6) (2021).
[256] H. Sirringhaus, T. Shimoda, Inkjet Printing of Functional Materials, MRS Bulletin 28(11) (2011) 802-806.